

**Photonic Terahertz signal analyzers: fully
ballistic Terahertz source for a photonic
VNA and error analysis of Terahertz
time domain spectroscopy of liquids**

vom Fachbereich Elektrotechnik und Informationstechnik der
Technischen Universität Darmstadt

zur Erlangung des Grades
Doktor Ingenieur
(Dr.-Ing.)

Dissertation
von Mario Méndez Aller

Referent: Prof. Dr. Sascha Preu
Korreferent: Prof. Dr. Duu Sheng Ong

Darmstadt 2021

Méndez Aller, Mario:

Photonic Terahertz signal analyzers: fully ballistic Terahertz source for a photonic VNA and error analysis of Terahertz time domain spectroscopy of liquids,

Darmstadt, Technische Universität Darmstadt

Jahr der Veröffentlichung der Dissertation auf TUPrints: 2022

URN: urn:nbn:de:tuda-tuprints-202534

Tag der mündlichen Prüfung: 20.07.2021

Veröffentlichung unter CC-BY-SA 4.0 International

<https://creativecommons.org/licenses/>

A mi padre.

Contents

Abbreviations	v
Abstract	vii
Kurzfassung	ix
Acknowledgments	xi
1. Introduction and Overview	1
1.1. Motivation and State-of-the-Art	1
1.2. Thesis outline	4
2. Photomixing devices for a CW PVNA	7
2.1. The concept of continuous-wave photomixing	7
2.1.1. Ideal photomixer operation	7
2.1.2. Photomixer operation limits	8
2.2. Antenna-coupled photomixing devices	11
2.2.1. Antennas	11
2.2.2. Photoconductive devices	11
2.2.3. Optimization of p-i-n diodes for THz operation	16
2.2.4. Realization of THz p-i-n diodes concepts	20
2.3. Waveguide-coupled full-ballistic p-i-n diode	22
2.3.1. Diode heterostructure overview	23
2.3.2. Passive optical waveguide (POW)	23
2.3.3. Analytical determination of the coupling length between the POW and the FB-p-i-n diode	26
2.3.4. FB-p-i-n diode designs	29
3. Fabrication and characterization of a fully-ballistic-p-i-n diode	33
3.1. Fabrication of the FB-p-i-n diode	33
3.1.1. Processing overview	33
3.1.2. Ohmic contacts	36
3.1.3. Plasma-assisted dry etching	39
3.1.4. Other processes	42
3.2. Characterization of the FB-p-i-n diode	43
3.2.1. Experimental setup	43
3.2.2. Some practical considerations	43
3.2.3. Terahertz Characterization	45

3.2.4.	Photocurrent comparison to top-illuminated diodes	48
3.3.	Conclusions and further work	49
4.	THz time-domain spectroscopy of liquids	53
4.1.	Transmission THz-TDS of liquids	53
4.1.1.	Basics of terahertz time-domain spectroscopy	53
4.1.2.	Extraction of material parameters of liquids	54
4.1.3.	Iterative algorithm for optical constants extraction	57
4.2.	Error Sources of THz-TDS of Liquids	57
4.2.1.	Introduction and Overview	57
4.2.2.	Systematic errors due to approximations	58
4.2.3.	Systematic and random errors due to cuvette dimensions	61
4.2.4.	Error due to misplacement of the cuvette	66
4.2.5.	Error introduced by the resolution of the TDS system	69
4.2.6.	Amplitude variations in the THz signals	71
4.2.7.	Optimal cuvette length	72
4.2.8.	Phase unwrapping artifacts and correction	73
5.	Distinctness of engine oil contamination with fuel and oxidation grade using THz-TDS	79
5.1.	Introduction	79
5.2.	Samples and measurement techniques	80
5.2.1.	Samples under test	80
5.2.2.	Data set: division in measurement rounds	80
5.2.3.	Measurement setup	81
5.3.	Cuvette thickness error estimation	83
5.3.1.	Estimation of the error for individual cuvettes	83
5.3.2.	Estimation of the sample thickness error between different assemblies	85
5.4.	Uncertainty of the optical constants with a single-cuvette configuration	86
5.4.1.	Single cuvette standard deviation of the refractive index	88
5.4.2.	Single-cuvette standard deviation of the absorption coefficient	90
5.5.	Distinctness of the samples in a single-cuvette configuration	92
5.6.	Uncertainty of the optical constants using multiple cuvettes	95
5.6.1.	Intra-round error metrics	96
5.6.2.	Standard deviation of the measurements using multiple cuvettes	98
5.7.	Other sources of error and summary	101
6.	Broadband characterization of biodiesel blends	105
6.1.	Introduction and motivation	105
6.2.	THz-TDS setup and sample description	106
6.3.	Absorption models for diesel and biodiesel	107
6.3.1.	Non-polar liquid model for diesel	107
6.3.2.	Modified model for biodiesel	109

6.3.3. Data fit to models	109
6.4. Broadband blend characterization	111
6.4.1. Linear combination model of blends	111
6.4.2. Real-time characterization	113
6.4.3. Biodiesel content determination by maximum dispersion . . .	114
6.5. Conclusions and Further Work	115
7. Conclusions and summary	117
A. Dry etching process description and calibration	119
A.1. III-V semiconductor etching process	119
A.2. SiN etching process	120
A.3. Other recipes and summary	120
A.3.1. Photoresist removal	120
A.3.2. Cleaning process	121
A.3.3. Summary	121
B. Optical constants of the S.I.-Fe:InP substrate	125
C. Error normalization	127
Bibliography	137
Erklärungen laut Promotionsordnung	139
Selected publications	139

Abbreviations

AC alternate current.

AE antenna emitter.

ARC anti-reflective coating.

CW continuous-wave.

DC direct current.

DNR dynamic range.

EDFA erbium doped fiber amplifier.

FAME fatty acid methyl ester.

FB fully-ballistic.

GHz gigahertz.

ML monolayer.

MOCVD metalorganic chemical vapour deposition.

PECVD plasma enhanced chemical vapor deposition.

POW passive optical waveguide.

PVNA photonic VNA.

s. i. semi-insulating.

SMF single-mode fiber.

SNR signal-to-noise ratio.

TDS time-domain spectroscopy.

THz Terahertz.

UTC uni-travelling-carrier.

VNA vector network analyzer.

Abstract

The technological gap in the terahertz (THz) range has reflected in the lack of cost-effective tools to characterize and develop the necessary technology, such as vector network analyzers (VNAs) and spectrum analyzers. This thesis presents on its first part a fully-ballistic (FB)-p-i-n diode THz source for a photonic vector network analyzer (PNVA). The source is designed towards a commercial implementation with efficient optical coupling, improved thermal conductivity and ease of commercial fabrication as compared to n-i-pn-i-p superlattice photomixers. Special emphasis is put in the refinement of some necessary processing steps that required some of the largest efforts within this thesis. The FB-p-i-n diode exhibits experimentally an improved efficiency in terms of transport time roll-off at high frequencies (beyond 1 THz) compared to a n-i-pn-i-p superlattice diode, although it still features a lower absolute emitted power than the n-i-pn-i-p. Pathways to overcome these limitations in future implementations will be outlined.

The second part of the thesis presents analyses with THz-time domain spectroscopy (THz-TDS) of liquids. After a theoretical description of the THz-TDS technique and of the main systematic and random sources of error, motor oil with different grades of gasoline contamination and oxidation is used to analyze how the different sources of error arise during the experiment. A higher robustness of the phase measurements is demonstrated (i.e. samples distinguished using refractive index), not being affected by system noise and exhibiting an error close to the resolution limit. However, the more differentiated absorption coefficient between the samples makes it still a better parameter to discern contamination and oxidation levels.

Chapter 6 presents a novel technique to identify biodiesel in petroleum-diesel blends using broadband information of the absorption coefficient. This new approach demonstrates the adequacy of using a linear combination of two models, one for each of the two components, to identify the exact content, exhibiting a deviation from the nominal values of the biodiesel content of less than 3%. This opens the door to real-time analysis of the blend in the absence of narrow spectral features, just relying on the broadband, featureless absorption of each component. Relying on broadband information also eliminates the uncertainty about the origin of the absorption coefficient at individual frequencies, which could be affected by many other contaminants and systematic errors.

Kurzfassung

Die technologische Lücke im Terahertz (THz)-Band zeigt sich in einem Mangel an kosteneffizienten Geräten zur Charakterisierung von Bauteilen und Komponenten, wie z.B. Vektornetzwerkanalysatoren (VNAs) und Spektrumanalysatoren. Diese Arbeit präsentiert in ihrem ersten Teil eine voll ballistische (fully-ballistic, FB)-p-i-n-Diode als Quelle für einen photonischen VNA (PVNA). Die Quelle ist auf eine kommerzielle Implementierung mit effizienter optischer Kopplung, verbesserter Wärmeleitfähigkeit und einfacher kommerzieller Herstellung im Vergleich zu anderen Technologien wie n-i-pn-i-p-Übergitter-Fotomischern ausgelegt. Besonderes Augenmerk wird auf die Verfeinerung einiger notwendiger Prozessschritte gelegt, die einige der größten Anstrengungen innerhalb dieser Arbeit darstellten. Die hier vorgestellte FB-p-i-n-Diode zeigt experimentell eine verbesserte Effizienz hinsichtlich des Transportzeitabfalls bei hohen Frequenzen (über 1 THz) im Vergleich zu einer ni-pn-ip-Übergitterdiode, obwohl sie immer noch eine niedrigere absolute emittierte Leistung aufweist. Verbesserungsmöglichkeiten für zukünftige Implementierungen werden aufgezeigt.

Der zweite Teil der Arbeit befasst sich mit Analysen mittels THz-Zeitbereichsspektroskopie (THz-TDS) von Flüssigkeiten. Nach einer theoretischen Beschreibung der THz-TDS-Technik und den wichtigsten systematischen und stochastischen Fehlerquellen wird Motoröl mit unterschiedlichen Verschmutzungs- und Oxidationsgraden von Benzin verwendet, um zu analysieren, wie sich die verschiedenen Fehlerquellen auf das spektroskopische Ergebnis auswirken. Es wird eine höhere Robustheit der Phasenmessungen gezeigt (d. H. Proben, die anhand deren Brechungsindex unterschieden wurden), die nicht durch Systemrauschen beeinflusst werden und einen Fehler nahe der Auflösungsgrenze zeigen. Der differenziertere Absorptionskoeffizient zwischen den Proben macht es jedoch immer noch zu einem geeigneteren parameter, um den Oxidationsgrad bzw. den Kontaminationsgrad zu bestimmen.

Im letzten Kapitel wird eine neuartige Technik zur Identifizierung von Biodiesel in Erdöl-Diesel-Gemischen anhand von breitbandigen Messungen des Absorptionkoeffizienten vorgestellt. Dieser neue Ansatz zeigt die Präzision der Bestimmung des Biodiesel-Gehalts anhand einer Linearkombination von zwei Modellen, eines für jede der beiden Komponenten wobei eine Abweichung von den Nennwerten des Biodieselgehalts von weniger als 3% gezeigt wird. Dies ermöglicht die Echtzeitanalyse der Mischung, ohne dass enge spektrale Merkmale erforderlich sind. Durch die Verwendung von Breitbandinformationen werden auch Fehler bei der Bestimmung des Biodieselgehalts vermieden, wenn andere Verunreinigungen und systematische Fehler die Absorption bei spezifischen Frequenzen beeinflussen.

Acknowledgments

The first acknowledgement is for Prof. Dr. Sascha Preu for his guidance and help during the thesis as well as for trusting and motivating me throughout all these years. It has been an honor and a privilege to be a part of the beginning of his professorship. Thank you!

I would also like to thank the following persons that contributed to this thesis:

- To all the colleagues who were joining the group all these years. I cannot imagine a better work environment without them. A special acknowledgment to Stefan, who has probably been the person I had spent the most time within the last six and a half years (which I do not regret).
- To all the technicians from the IMP, specially Peter Kießlich and Andreas Semrad, for their dedicated and extraordinary work.
- To Prof. Dr.-Ing. Andreas Stöhr, from Universität Duisburg-Essen, for providing us the necessary technology for fabricating the FB-p-i-n diodes. To José Luis Fernández Estévez, a great professional who helped with the fabrication in Duisburg and with whom it was a pleasure to work, not only the great knowledge and support he gave me, but also for the enjoyable experience that it was to work next to him. ¡Muchas Gracias!
- To Prof. Dr. Ong Duu Sheng, from the Multimedia University in Selangor, Malaysia, for providing us with the biodiesel samples and his continuous support and interest on our work together.
- To Prof. Dennis Watson, from the Southern Illinois University, for providing with the motor-oil samples that are the heart of the second half of this thesis.
- To my parents for all the support they have always given me, and my siblings Isabel, Marta and Luis, for being an example to follow.

1. Introduction and Overview

1.1. Motivation and State-of-the-Art

The Terahertz (THz) range, defined as the frequency range between 100 GHz and 10 THz, has been a technological gap between millimeter waves, at some tens of GHz, and optics, above some tens of THz. In the last decades, however, a number of new applications have fostered strong technological progress.

Many optically opaque substances, such as plastics, paper or clothes are transparent to THz radiation, while polar substances present multiple narrow absorption lines in the THz range, making THz spectroscopy a very powerful tool for composition analysis by its molecular fingerprint. In combination with imaging, where THz features a higher resolution than millimeter and sub-millimeter wavelengths, these characteristics enable the identification of hazards and makes THz radiation a very attractive technology for security applications. With the increasing demand of bandwidth, THz technology is also a promising candidate in future communication applications.

While the gap has started to close from both sides, table-top systems still feature lower performances in comparison to optic or electronic systems. The technological gap also reflects the lack of costly-effective tools for device characterization and development, such as vector network analyzers (VNAs) or spectrum analyzers, which makes the development of THz technology and components more complicated and expensive.

State-of-the-art VNAs are limited to maximum frequencies of around 65 GHz. Beyond this frequency, VNAs require frequency extenders [1], composed of frequency doublers and triples which usually consist of Schottky diode-based multipliers. The hollow metal waveguide configuration of the frequency extenders limits the bandwidth of an extension set to less than a 50% of the center frequency, requiring of a complete exchange of the equipment and recalibration for larger frequency sweeps. At the same time, the cost increases exponentially with frequency and an extension above 500 GHz is already several times more expensive than commercial photonic THz systems, which are already competitive in terms of dynamic range at these frequencies.

State-of-the-art photonic systems at 1550 nm offer peak dynamic range (DNR) of 105 dB [2], not far from the specifications of commercial extenders from Virginia Diodes [1]. A comparison between the DNR of the commercially available extenders and a commercial THz setup from Toptica Photonics AG is shown in fig. 1.1. Around 400 GHz, the maximum difference on DNR is 40 dB. At 1 THz, the VNA

1. Introduction and Overview

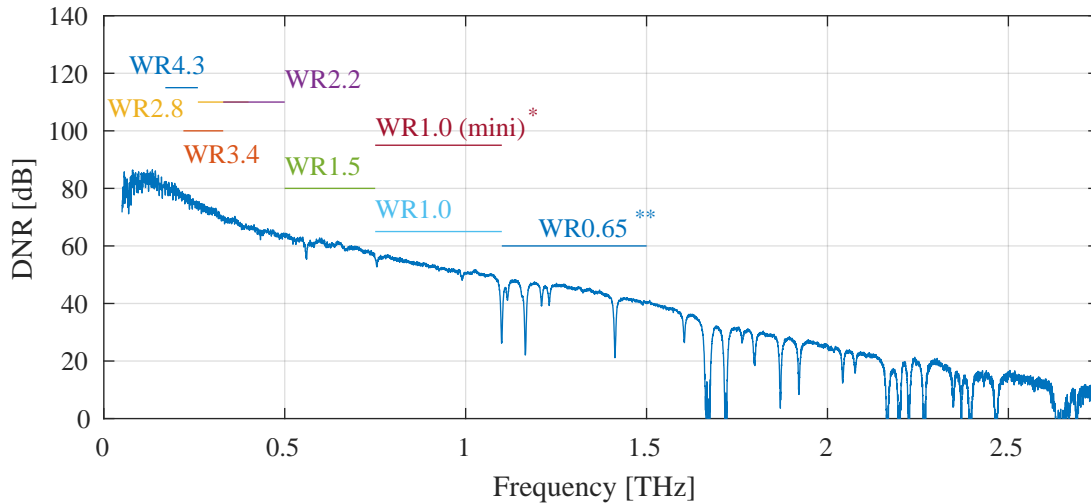


Figure 1.1.: State-of-the-art of frequency extenders from Virginia Diodes [1] and comparison to the DNR result using commercially available table-top CW setup from Toptica AG and an in-house developed detector. The DNR is set to a $ENBW = 10$ Hz. *This dynamic range is only possible under certain conditions established by the manufacturer. **Performance of the WR0.65 with a TxRx-Rx configuration, a TxRx-TxRx configuration will experience an additional ~ 15 dB losses and requires of additional hardware.

performance depends strongly on the phase noise level of the VNA sources, but the photonic systems becomes competitive in terms of DNR above 1 THz. Photomixers show a strong roll-off of f^{-4} that quickly degrades the system performance, but the frequency extender counterpart faces issues with fabrication of metallic structures above 1 THz that introduce additional losses (e.g. surface roughness, Skin effect, coupling losses) and makes VNA frequency extenders exponentially more expensive and severely degrades its DNR, yet with only 40-60 dB at $ENBW=10$ Hz [1]. Therefore, photonic systems yet show comparable or even superior performance above 1 THz. Further, there are no commercial extenders available beyond 1.5 THz yet.

Photonic VNAs (PVNAs) can be constructed using continuous-wave (CW) or pulsed THz technology, although the characteristics and the field of application for each of them is different. Potential schemes of the PVNA systems are shown in fig. 1.2, where free space configurations are depicted. On-chip developments are a potential powerful implementation, specially for CW-PVNA. Pulsed setups will suffer from the dispersion of the waveguides and components that are necessary for an on-chip configuration.

Continuous-wave PVNA

A basic scheme for a CW-PVNA, as proposed by Preu in [3], is shown in fig. 1.2a. It consists of the combination of transmission and reflection configurations using

two different sources (p-i-n diode-like photomixers), producing a CW-THz signal modulated at two different frequencies, which are further detected by two photoconductive receivers at each side of the sample. The different modulation at each transmitter can be applied using a traditional bias modulation to the p-i-n diodes, but other alternatives using electro-optical and accusto-optical modulation are being considered for faster data acquisition.

The enabling technologies for PVNAs at telecom wavelengths (~ 1550 nm) are:

- **Lasers with large tunability.** The optical subsystem relies on telecom wavelength (~ 1550 nm) components, that are commercially available and affordable in large quantities and specifications, benefitting from the telecom market. Thermally stabilized DFB lasers are widely used, providing tunabilities of around 1.2 THz per diode pair. The combination of three diodes allow systems to cover up to 2.75 THz [4]. They provide linewidths in the range of 1 MHz, though this can be reduced down to the Hz level by the use of frequency comb generators [5]. Other solutions, such as VCSELs, can be tuned beyond 10 THz, thus covering the whole range with a single optical setup [6].
- **Photomixing sources.** CW THz setups are usually driven by p-i-n diode based sources. Examples of ultra-wideband (covering several decades) p-i-n sources are e.g. UTC diodes, providing up to $2 \mu\text{W}$ [7] at 1 THz, n-i-pn-i-p superlattice photomixers, with around $0.8 \mu\text{W}$ at 1 THz [8,9] and waveguide integrated (WIN)-photodiodes [10]. At the lower end of the THz range triple transit time diodes [11] reach more than 1 mW at 110 GHz.
- **Photoconductive receivers.** CW THz systems usually rely on photoconductors for homodyne detection. New materials feature noise-floors in the fW/Hz range at 200 GHz [12]. Combined with state-of-the-art photonic sources, they offer a peak dynamic range above 100 dB and still >50 dB at 1 THz [2,13].
- **Passive components for on-chip solutions.** Dielectric waveguides and related passive components (e.g. couplers, filters, etc.) can be used covering larger bandwidths, as compared to hollow waveguides. Dielectric rod waveguides (DRW) have already been demonstrated coupled to a n-i-pn-i-p superlattice photomixer [14]. As long as multimodal operation is not an issue, the bandwidth extends from the frequency in which the field is sufficiently confined in the dielectric structure, without upper cut-off frequency. As the confinement of the field changes with frequency, they are intrinsically dispersive. This is however not an issue in CW-PVNA systems, where only a single frequency propagates at a time.
- **Calibration and measurement routines.** Appropriate calibration and the measurement routines are also a key factor of a PVNA. New techniques must be implemented to obtain S-parameters using a two-port configuration. Additionally, identifying and characterizing random and systematic errors that

1. Introduction and Overview

affect the parameter extraction is an important step towards the system implementation, which should attempt to mitigate or isolate these errors.

Amongst these subsystems, a main bottleneck for extending the system performance are the photomixing sources and photoconductive receivers, both showing continuous improvement within the past decade. This thesis aims for improving the performance of the photomixer source, particularly at frequencies above 0.5 THz.

Free space pulsed PVNA

Free space pulsed PVNA is a potentially powerful tool to characterize planar devices such as polarizers, metamaterials or photonic crystals or simply bulk materials for determination of their THz properties. This system will allow to analyze the structure of the devices through the double source and detector configuration. A candidate system is depicted in fig. 1.2b. The two port configuration consists of two sources modulated through the bias at different frequencies and disposed in a combined transmission and reflection setup with detectors also at both sides of the sample under test.

In this thesis, a transmission TDS setup is used which can be considered as a VNA only recording the S21 parameter. A full two port pulsed PVNA is currently being developed in the group. A remaining difficulty is the separation of the optical thickness nd into the physical thickness d and the refractive index n from the S21 measurement only. The situation becomes even more challenging when the samples under test are too thin or dispersive. The comprehension of the systematic error sources that affect the system is an important element towards the implementation of a free space pulsed PVNA. Understanding how the sample positioning, the Fabry-Pérot oscillations or the system resolution affects the THz-TDS measurements helps to understand the challenges that this system presents.

One of the proposed calibration methods in a free-space pulsed PVNA consists on using a well-known dielectric slab as a reference. Analyzing the systematic and random errors that appear between the reference and the sample measurement is of great importance to provide reliable characterizations of the samples.

1.2. Thesis outline

This thesis is composed of two parts, addressing different challenges for photonic systems:

The **first part** focuses on the development of continuous-wave sources for increasing the optical to THz conversion efficiency, enabling two port measurements using table-top systems with tens of mW of optical power levels. In chapters 2 and 3, the concept and experimental demonstration of passive optical waveguide (POW) coupled fully ballistic (FB) p-i-n diodes (FB-p-i-n) is presented as a suitable CW-THz source with improved high frequency performance.

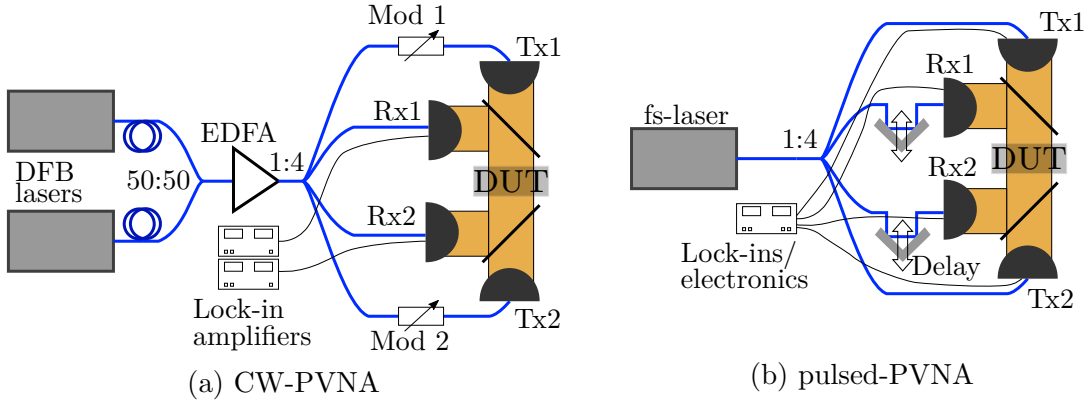


Figure 1.2.: Proposed schemes for PVNAs. For simplicity, free space approaches are depicted.

Chapter 2 introduces the basics of photomixing CW photomixers and antenna-coupled devices, specifically giving an overview about the operation of p-i-n diode sources and photoconductive detectors. The last part of the chapter presents the waveguide-coupled fully-ballistic p-i-n diode and the main aspects about the design of the POW.

Chapter 3 presents the fabrication and the THz characterization of the fully-ballistic (FB)-p-i-n diode.

The **second part** of the thesis (chapters 4 to 6) reports on THz-time-domain spectroscopy (TDS) of liquids, putting emphasize on the data evaluation and the identification of error sources that limit the optical parameters extraction of the sample, which will be present in free-space pulsed PVNAs.

Chapter 4 presents the basics of THz-TDS of liquids. Based on the peculiarities of liquid spectroscopy, techniques for parameter extraction are described. The second part of the chapter models and describes the most relevant error sources and quantifies systematic errors introduced by the post-processing techniques or introduced by common approximations and assumptions.

Chapter 5 uses the characterization of different levels of fuel contamination and oxidation with THz-TDS as a data pool for the influence and magnitude of different random and systematic errors such as, e. g. sample position and thickness uncertainty and resolution induced uncertainty.

Chapter 6 demonstrates the strength of the THz TDS system and the developed evaluation routines by identifying the biodiesel concentration in diesel blends, without any narrow spectral feature.

2. Photomixing devices for a CW PVNA

Continuous-wave (CW) PVNAs will rely on photomixing sources and detectors to operate. This chapter gives an overview of the fundamentals of photomixing, particularly about the p-i-n diode-based sources and photoconductive detectors. It provides also a description of a candidate source developed during this thesis, a waveguide-coupled full-ballistic (FB) p-i-n diode, including the description of an analytical method using a planar waveguide approximation to study the optical coupling between the built-in POW to the p-i-n diode, which will be compared to the previous numerical results.

2.1. The concept of continuous-wave photomixing

2.1.1. Ideal photomixer operation

Continuous-wave (CW) photomixing is the result of beating two lasers at frequencies $f_1 = f - f_{THz}/2$ and $f_2 = f + f_{THz}/2$ detuned by the desired THz frequency, f_{THz} .

The resulting electric field of the two beating lasers is:

$$\vec{E}_t = \vec{E}_1 \exp [j2\pi(f - f_{THz}/2)t] + \vec{E}_2 \exp [j2\pi(f + f_{THz}/2)t + \phi] \quad (2.1)$$

The optical intensity is

$$I_{opt}(t) \sim |\vec{E}_t|^2 = |\vec{E}_1|^2 + |\vec{E}_2|^2 + 2|\vec{E}_1 \cdot \vec{E}_2| \cos(2\pi f_{THz}t + \phi) \quad (2.2)$$

Expressing eq. (2.2) in terms of the optical power yields

$$P_{opt} = P_1 + P_2 + 2\sqrt{P_1 P_2} \cos \alpha \cos(2\pi f_{THz}t - \phi), \quad (2.3)$$

where $P_1 \sim E_1^2$ and $P_2 \sim E_2^2$ are the power of each laser and α is the relative angle between the electric field of the two lasers. eq. (2.3) shows that the amplitude of the modulation is maximized for $P_1 = P_2$ and when both lasers have the same polarization ($\alpha = 0$). Therefore, rewriting for the optimal conditions yields

$$P_{opt} = P_L(1 + \cos(2\pi f_{THz}t + \phi)), \quad (2.4)$$

where $P_L = P_1 + P_2 = 2P_1 = 2P_2$.

2. Photomixing devices for a CW PVNA

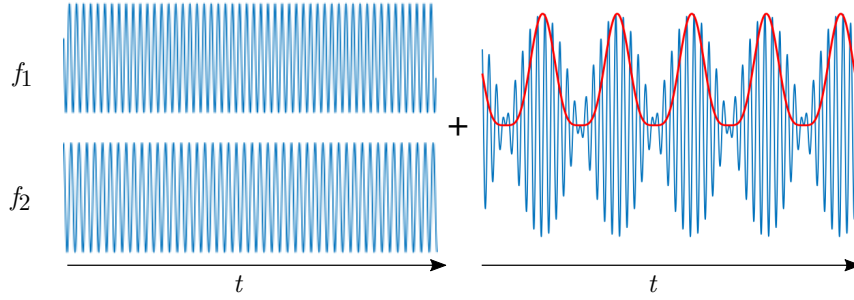


Figure 2.1.: Graphical interpretation of heterodyning. Here, two tones with frequencies $f_1 = f_0 + f'/2$ and $f_2 = f_0 - f'/2$, with $f_0 = 10f'$. The red trace correspond to the amplitude of the modulated intensity.

An ideal photoconductor, which absorbs all light and has no losses, will then generate a photocurrent:

$$I_{Ph,id} = \frac{eP_L}{hf} [1 + \cos(2\pi f_{THz}t + \phi)] \quad (2.5)$$

This work uses antenna coupled devices as sources. When the device is attached to an antenna with radiation resistance R_A , the ideal radiated THz power is

$$P_{THz,id} = \frac{1}{2} R_A (I_{Ph,id})^2 \quad (2.6)$$

2.1.2. Photomixer operation limits

The ideal photocurrent $I_{Ph,id}$ assumes that every available photon will generate an electron-hole pair. However, not all available photons are absorbed, limiting the efficiency of the device. The photocurrent on a photomixer differs from the ideal photocurrent through the external photonic efficiency, $\eta_{ph,I}$.

There are also physical limitations of the devices that affect the radiated power at high frequencies. These are the capacitance of the device, which introduces a RC time constant with the antenna resistance R_A , and the interference of carriers generated at different times while being transported. These two characteristics introduce roll-offs, usually referred as RC roll-off and transport-time roll-off, that degrade the radiated power as $\eta \sim f_{THz}^{-2}$.

External quantum efficiency

The external quantum efficiency, η_{ext} can be divided into two different phenomena:

- Propagation loss: the light reflected at the interface between the air and the semiconductor. In some cases, an anti-reflective coating (ARC) might help to reduce the impact. For a power reflection coefficient R the power and, thus, the photocurrent, is reduced by the factor

2.1. The concept of continuous-wave photomixing

$$T = (1 - R) \quad (2.7)$$

For side illuminated devices, the laser couples through a waveguide that may feature additional transmission losses with $T_{wg} < 1$.

- Imperfect absorption: not all the photons that are incident on the semiconductor device are absorbed. For a semiconductor length, d_i (for example, the intrinsic layer length of a p-i-n diode) and absorption coefficient α , with values around 8000 cm^{-1} for GaAs at 1.55 eV (800 nm) [15] and 10000 cm^{-1} for $\text{In}_{0.53}\text{Ga}_{0.47}\text{As}$ at 0.8 eV (1550 nm) [16]. The total absorbed power can then be expressed as

$$P_{abs} = P_L (1 - e^{-\alpha d_i}) \quad (2.8)$$

Therefore, the external quantum efficiency for the photocurrent is

$$\eta_{ext,I} = (1 - R) (1 - e^{-\alpha d_i}) \quad (2.9)$$

With the resulting photocurrent, I_0 :

$$I_0 = \eta_{ext,I} I_{Ph,id} \quad (2.10)$$

As $P_{THz} \propto I_{Ph,id}^2$, the external efficiency for the radiated power is $\eta_{ext} = \eta_{ext,I}^2$, reducing the ideal radiated power as:

$$P_{THz} = \eta_{ext} P_{THz,id} \quad (2.11)$$

RC roll-off

Antenna coupled photomixers can be modeled as RC circuits in which the capacitance is defined by the intrinsic device capacitance or contacts metallization on the active semiconductor and connected to an antenna with a radiation resistance R_A . This model corresponds to a first order low pass filter that attenuates the AC photocurrent by a factor $\eta_{RC}^i = 1/(1 + i2\pi f_{THz} C R_A)$. The power degradation due to this RC low pass filter, defined as RC roll-off, is:

$$\eta_{RC} = \frac{1}{1 + (2\pi f_{THz} C R_A)^2} = \frac{1}{1 + (f_{THz}/f_{RC}^{3dB})^2}, \quad (2.12)$$

where the 3 dB roll-off frequency f_{RC}^{3dB} is defined as:

$$f_{RC}^{3dB} = \frac{1}{2\pi C R_A}, \quad (2.13)$$

where C is the capacitance of the device.

Transport time roll-off

A second roll-off phenomenon that degrades the high-frequency operation of photomixers arises when the THz frequency becomes close to the inverse average time that a single carrier is contributing to the photocurrent, known as carrier transport time (τ_t), and the remaining carriers start screening newly generated electron-hole pairs. The contribution time of an individual carrier is determined either by the average time it needs to recombine, defined as recombination time (τ_{rec}), or by the average time that it takes to reach a contact, defined as transit time (τ_{tr}). The total transport time can be approximated as $1/\tau_t \approx 1/\tau_{rec} + 1/\tau_{tr}$.

Transport time roll-off affects different photomixers in a different manner. Photoconductive mixers are dominated by the recombination lifetime, τ_{rec} (therefore termed as "lifetime roll-off"), while transit time τ_{tr} is relevant to the operation of p-i-n diodes. Transit time, however, must also be considered on photoconductive devices, as the ratio between τ_{rec} and τ_{tr} , representing the ratio of carriers actually contributing to photogenerated current, often termed as photoconductive gain, g , with typical values of $g \sim 10^{-2} - 10^{-3}$, reduces the power emitted by these devices at all frequencies.

Optimization of the photomixer for transport roll-off will generally compromise RC roll-off and thermal and electrical constraints, which limits the maximum bias and optical power that can be fed to the photomixer. In the following sections, the optimization criteria for each type of antenna-coupled photomixer are formulated.

Laser limitations

For CW photomixers, the THz resolution and bandwidth are limited by the linewidth and detuning range of the lasers, respectively. Detuning a laser by 1 THz requires a 8 nm detuning at 1550 nm. Whilst many lasers offer tuning ranges far beyond 10 THz, not imposing any limitations to the THz bandwidth, there are other mechanisms that limit the performance at THz frequencies. In terms of linewidth, there are many commercially available and inexpensive DFB lasers with linewidths on the MHz and sub-MHz range, but stabilized system can achieve resolutions down the Hz level [5].

The wide and agile tuning range makes photomixers specially favorable for spectroscopy applications, in which photomixers not only provide a wide operational bandwidth, but also the capability to resolve narrow features. CW photomixers are also essential for PVNAs, with the same device operating from a few GHz to several THz without the source being a limiting element, as it is the case for conventional VNA frequency extenders.

2.2. Antenna-coupled photomixing devices

2.2.1. Antennas

In this work, mainly antenna coupled devices will be taken into consideration. Antennas are responsible for efficiently converting the THz power generated as photocurrent into emitted THz power. For applications such as spectroscopy or emitters meant to work as PVNA sources, it is necessary to use ultra-wideband antennas. These antennas are often self-complementary and planar on a semi-insulating semiconductor. Their radiation resistance is obtained from Babinet's Principle as

$$R_A = \sqrt{\mu_0 / (4\epsilon_0\epsilon_{eff})} = \frac{60\pi}{\sqrt{\epsilon_{eff}}}, \quad (2.14)$$

where ϵ_{eff} is the effective permittivity, which can be approximated by $\epsilon_{eff} = (1 + \epsilon_r)/2$ for an antenna deposited on a semiconductor (dielectric permittivity ϵ_r)-air (dielectric permittivity $\epsilon_{air} = 1$) interface. For a substrate with $\epsilon_r = 13$, the radiation resistance is then $R_A \approx 72 \Omega$.

The most common antennas used for CW operation, illustrated in fig. 2.2, are:

- **Logarithmic spiral antennas.** The bandwidth of this circularly polarized antenna is set by its dimensions. The upper limit of the band will be limited by the gap size between the two antenna arms, usually corresponding to the photomixer or diode size. The lower limit is set by the polarization change at lower frequencies. The functional limit is usually set at the point in which the axial ratio drops below 2. This usually happens when the total arm length becomes approximately one wavelength ($\lambda_0/\sqrt{\epsilon_{eff}}$) [17].
- **Bow-tie antennas.** For opening angles of 90° , the self-complementary shape of this type of antennas provides a very constant radiation resistance through the whole frequency range and linear polarization. The radiation pattern is, however strongly dependent on frequency.
- **Log-periodic antennas.** This antenna is a bow-tie with teeth-shaped arms attached acting as resonators. For that reason, the radiation resistance is not as constant as for bow-ties and spirals and the radiation pattern also depends strongly on the frequency. They, however, feature an overall high directivity and are widely used for THz emitters. They are linearly polarized, but with a polarization perpendicular to the bow-tie antennas, and with the arms provoking slight polarization changes at different frequencies.

2.2.2. Photoconductive devices

Photoconductive mixers are very common devices for both sources and receivers at CW, as well as the most common devices on pulsed homodyne systems. While the

2. Photomixing devices for a CW PVNA

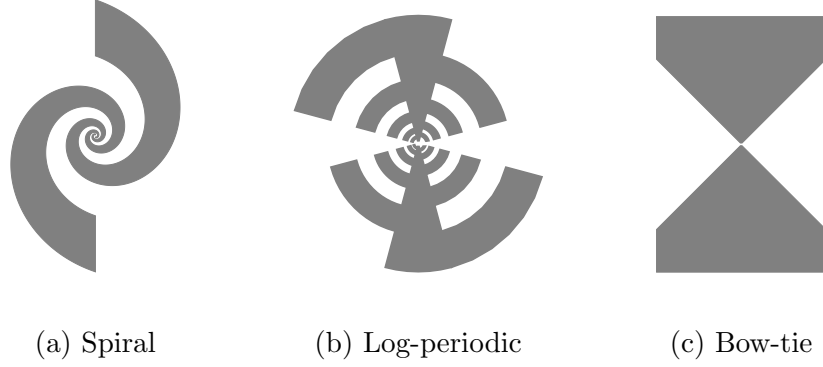


Figure 2.2.: Most common antennas used for CW photomixers

source presented in this paper is a p-i-n diode based photomixer, an overview of the photoconductors is given for two main reason: they are an immediate alternative as a source and comprise all the detectors use in this thesis.

In photoconductors, the beaten lasers illuminate a semiconductor material with metallic contact electrodes (which are, at the same time, the innermost tips of the antenna for antenna-coupled devices). The modulated power of the heterodyned laser generates electron-hole pairs that are then accelerated by an external bias in the range of several tens of volts: 15 V peak to peak (± 7.5 V_p) for very conservative long-term operation under CW regime with an electrode gap around 2 μm [13] and up to 200 V DC under pulsed operation with an electrode gap around 25 μm , corresponding to a field strength of approximately 35 kV/cm [18].

Lifetime roll-off of photoconductors

As indicated in section 2.1, when the THz frequency becomes comparable to $1/\tau_{rec}$, generated carriers start screening each other, producing a degradation of the THz photocurrent and thus, of the emitted THz power.

The amount of carriers generated at a time t_0 for a time interval of Δt by the lasers are $\Delta N(t_0) = I_0 \Delta t_0 / e (1 + \cos(2\pi f_{THz} t_0))$. The recombination lifetime τ_{rec} is then defined through the amount of carriers from t_0 which still survive at a later time $t > t_0$, which are $\Delta N(t) = \Delta N(t_0) \exp(-(t - t_0)/\tau_{rec})$ the total amount of carriers at a later time t_1 is the integral over all previous contributions at elapsed times $t = t_1 - t_0$ [9]

$$\begin{aligned}
 N(t) &= I_0/e \int_0^\infty [1 + \cos(2\pi f_{THz}(t - t_0))] e^{-t_0/\tau_{rec}} dt_0 \\
 &= I_0/e \cdot \tau_{rec} \left(\frac{\sin(2\pi f_{THz} t - \phi)}{\sqrt{1 + (2\pi f_{THz} \tau_{rec})^2}} + 1 \right), \tag{2.15}
 \end{aligned}$$

where $\phi = \arctan(2\pi f_{THz} \tau_{rec})$. Making the simplifying assumption that the current density j is homogeneous through the photoconductor cross section, the current is

calculated as $I = jA$ with $j = env_{dr}$, where $n = N/V$ is the carrier density, where N is the total number of carriers and V is the volume, which can also be expressed as $V = Ad_g$, where d_g is the gap between the two contacts, and v_{dr} is the drift velocity of the carriers. The current $I(t)$ is then

$$I(t) = \frac{eN(t)}{d_g} v_{dr} = \frac{eN(t)}{\tau_{tr}} = I_0 \frac{\tau_{rec}}{\tau_{tr}} \left(\frac{\sin(2\pi f_{THz} t - \phi)}{\sqrt{1 + (2\pi f_{THz} \tau_{rec})^2}} + 1 \right) \quad (2.16)$$

The AC term at eq. (2.16) rolls off as $1/\sqrt{1 + (2\pi f_{THz} \tau_{rec})^2}$. As $P_{THz} \propto I(t)^2$, a lifetime roll-off can be defined as

$$\eta_{LT} = \frac{1}{1 + (2\pi f_{THz} \tau_{rec})^2} \quad (2.17)$$

At the same time, the factor $g = \tau_{rec}/\tau_{tr} \ll 1$ affects both DC and AC component, reducing the total power. It is usually termed as photoconductive gain.

Including the effect of RC roll-off, the power radiated by an antenna-coupled photoconductive mixer is,

$$\begin{aligned} P_{THz} &= \frac{1}{2} R_A I_0^2 \cdot g^2 \cdot \eta_{LT} \cdot \eta_{RC} \\ &= \frac{1}{2} R_A I_0^2 \left(\frac{\tau_{rec}}{\tau_{tr}} \right)^2 \frac{1}{1 + (2\pi f_{THz} \tau_{rec})^2} \cdot \frac{1}{1 + (2\pi f_{THz} R_A C)^2} \end{aligned} \quad (2.18)$$

Here the capacitance is typically set by the interdigitated contacts in CW photomixers.

Material optimization for photoconductors

A good photoconductive material must fulfill certain features in order to have an efficient performance at high frequencies. In particular, for CW emitters we should consider [9, 13]:

- **Low carrier lifetimes.** Eq. (2.17) shows that the 3 dB lifetime roll-off frequency is $f_{LT}^{3dB} = 1/(2\pi\tau_{rec})$. A short carrier lifetime is therefore crucial for the maximum frequency operation of the photoconductor.
- **High absorption** at the laser wavelength, ideally above 5000 cm^{-1} . InGaAs-based devices fulfill this at 1550 nm [19].
- **High mobility** (μ) is required to obtain the maximum photocurrent at the given bias as $I \sim \mu E_{DC}$. There is however, a trade-off between the mobility and the amount of trap states introduced to reduce the carrier lifetime that has to be engineered. From the point of view of the transit time, as $I \sim \tau_{tr}^{-1}$, a high mobility increases the photoconductive gain.

2. Photomixing devices for a CW PVNA

- A **high dark resistance** reduces the DC electrical load on the semiconductor and, at the same time, makes the resistance under illumination higher, which is a critical requirement for detectors in order to reduce the noise floor.
- **Large breakdown field.** This particular feature is more difficult to engineer for 1550 nm photoconductors, as the break down field strength scales with the bandgap as $\sim (E_G)^{2.5}$ [20]. This is mainly relevant for sources where high voltages are applied.

1550 nm photoconductive sources and detectors

Despite the advantage of the amply available and cost effective 1550 nm lasers and components, photoconductors with inter-band transitions at this wavelength are more challenging to engineer compared to their 800 nm counterparts due to the lower band gap, which usually translates into a lower dark resistance and smaller break down field strength. Two basic strategies have been developed to overcome this limitation. The first one consists of solutions that make use of 800 nm materials (GaAs). They exploit the extrinsic photoconductivity that originates through the sub-band-gap absorption introduced by highly concentrated defects and impurities and include solutions for CW.

The first attempt on these extrinsic photoconductors at 1550 is LT-GaAs [21], showing overall very low absorption. A proposed solution for CW operation uses a waveguide photodetector formed by a p-i-n diode, with the LT-GaAs absorption region in the i-layer, that increases the overall absorption while maintaining constructive interference of THz waves generated along the transmission line, with distances over $\sim 100 \mu\text{m}$ [22].

Among the most successful extrinsic photomixers are homogeneously Er doped GaAs devices (Er:GaAs) [23] achieving < 0.5 ps scale carrier lifetime and dark resistances in the $\text{G}\Omega$ range, but without CW results so far.

The second approach are intrinsic photoconductive mixers based on materials with a band gap smaller than the photon energy at 1550 nm, such as InGaAs. LT-InGaAs is strongly n-type conductive and thus, is not a good candidate. Ion-damaged InGaAs has been demonstrated with lifetimes as low as 0.3 ps, but always with a high n-type background that does not allow for resistances above $5 \Omega\text{cm}$ [24].

More recent approaches are heterostructures of LT-InAlAs in LT-InGaAs forming quantum wells. It has been shown to be very successful with lifetimes in the range of ~ 0.5 ps, resistances of $\sim 300 \Omega\text{cm}$ and mobilities of $\sim 600 \text{cm}^2/\text{Vs}$ [25]. Better mobilities of $\sim 1100 \text{cm}^2/\text{Vs}$ are achieved at the expense of much longer lifetimes [26].

Homogenous Fe doping of InGaAs has achieved sub-ps lifetimes with electron mobility above $\sim 900 \text{cm}^2/\text{Vs}$ and resistivities of $\sim 1000 \Omega\text{cm}$ [27].

A material system developed within our group is presented in the following section. It consists of ErAs:InAlGaAs:InGaAs superlattice photoconductive material that has achieved bandwidths up to 6.5 THz under pulsed operation [18] and 52 dB dynamic range at 1 THz under CW operation [13]. In this thesis, these super-

lattice photoconductors are predominantly used as receivers for characterizing the developed p-i-n diodes, along other commercial photoconductors.

Superlattice ErAs:InAlAs:InGaAs photoconductors

The ErAs:InAlGaAs:InGaAs photoconductors [13,28] are a superlattice layer structure consisting of an intrinsic 15 nm InGaAs layer and 0.8 monolayers (ML) of semi-metallic delta-p-doped ErAs. In order to optimize its performance as photoconductive sources, an additional 2.5 nm InAlAs layer is grown between the InGaAs and the ErAs. This layer increases the dark resistance of the diode, but degrades the lifetime as carriers need now to tunnel through the InAlAs layers into the recombination states [9]. For detectors, driven by the THz field instead of the DC bias of sources, the best results are obtained without the InAlAs layer. This reduces the dark resistance and the break-down field of the detector, but strongly improves the mobility and reduces the carrier lifetime [9, 13].

As InGaAs and ErAs are grown at the same temperature of 480°C, they do it with a high crystalline quality. At the same time, the differences on the crystal structure of ErAs and InGaAs makes the ErAs non-wetting and, therefore, it does not require additional annealing to form clusters.

For the source, where the resistance is increased by using the InAlAs layers, a dark resistance of 4.5 MΩ and a mobility of 600 cm²/Vs are achieved. The break down field strength of this sources is 170 ± 40 kV/cm under dark conditions, which is the best among the intrinsic photoconductor mentioned above.

Material	τ_{rec} [ps]	ρ [Ωcm]	μ [cm ² /Vs]	E_{BD} [kV/cm]
Fe:InGaAs source [27]	0.3	2000	900	40 to > 60 ($P_L = 20$ mW)
ErAs:In(Al)GaAs source [9, 13]	1.3	670	1100	174 (dark) 45 ($P_L = 26$ mW) $w_G = 1.9$ μm [13]
ErAs:InGaAs detector [9, 13]	0.52	100 to 340	900	–
LT-InGaAs:LT-InGaAs (quantum wells) [25]	13	~ 300	600	-
LT-InGaAs:LT-InGaAs (quantum wells) [26]	0.5	~ 300	5000	-

Table 2.1.: Overview of 1550 nm photoconductive materials. τ_{rec} : carrier lifetime. ρ : resistivity. μ : mobility. E_{BD} : Break-down field strength, given, if available, for a gap between the contacts w_G and an optical power P_L .

2.2.3. Optimization of p-i-n diodes for THz operation

P-i-n diode-based photomixers provide some advantages with respect to photoconductive sources.

- In a p-i-n diode, ideally, every photogenerated carrier reaches the contact and contributes to the photocurrent (i.e. photoconductive gain has a value of $g = 1$).
- Unlike photoconductors, where voltages in the order of ~ 30 V are required, p-i-n diodes require reverse biases not higher than 3 V, leading to a much smaller electrical thermal load. Therefore, a much higher photocurrent can be handled by a device.

Two basic phenomena diminish the THz photocurrent and, consequently, the THz power at high frequencies in p-i-n diodes and photoconductors, namely the RC roll-off and transport roll-off. However, the nature of the latter is different to photoconductive mixers. In p-i-n diode sources, the transport time τ_t is practically identical to the transit time, with $\tau_{rec} \gg \tau_{tr}$, and recombination does not play any role. Carriers contribute to the generated current till they reach the respective contact. With some simplifying assumptions (very thin absorption region, or constant charge velocity, v_{sat} , e.g.) and defining $\tau_{tr} = d_i/v_{sat}$, the total current can be calculated as [29]

$$\begin{aligned} I(t) &= \frac{1}{\tau_{tr}} \int_0^{\tau_{tr}} I_0 [1 + \cos(2\pi f_{THz}(t - t'))] dt' \\ &= I_0 \left[1 + \cos \left(2\pi f_{THz}t - 2\pi f \frac{\tau_{tr}}{2} \right) \cdot \text{sinc} \left(2\pi f \frac{\tau_{tr}}{2} \right) \right] \end{aligned} \quad (2.19)$$

We can see how, unlike for photoconductive mixers, the DC component of the photocurrent remains unaltered, while the AC (THz) component rolls off by the sinc function. The emitted THz power will be then attenuated by the factor $\text{sinc}^2(2\pi f_{THz}/2)$. The sinc function zeros will usually disappear on realistic scenarios where electron-hole pairs generated at different times will be moving at different velocities. In fact, for most of the THz sources, only electrons contribute to the photocurrent and they experience an almost constant acceleration within the first ~ 100 fs after their generation (quasi-ballistic transport), as it will be described in the following sections.

The initial assumption that all carriers travel the whole distance, d_i , is usually not perfectly fulfilled in real devices. The absorption region features a certain width, typically of the order of 40-100 nm, while the intrinsic layer (transport layer) is $d_i = 200 - 400$ nm in length for most concepts. This leads to a smearing out of the nulls of the sinc function. Therefore, the transit time roll-off can be approximated by $\eta_{tr} = 1/(1 + f_{THz}/f_{tr}^{3dB})$, where f_{tr}^{3dB} can be calculated from $\text{sinc}^2(2\pi f_{tr}^{3dB}\tau_{tr}/2) = 0.5$ [29]. Solving the equation by approximating the sinc function to the first three

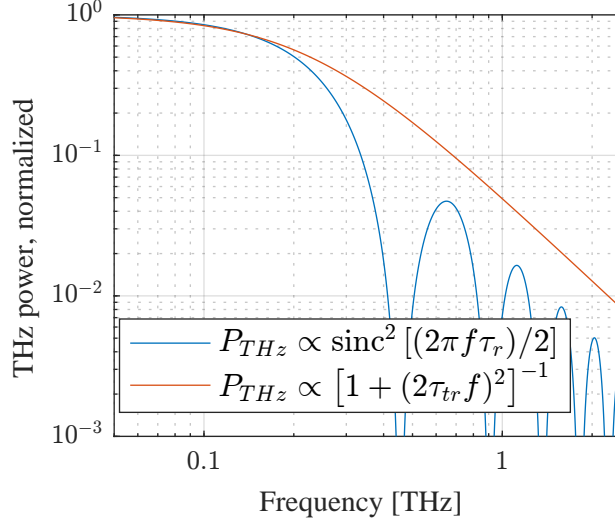


Figure 2.3.: THz power for a diode for a $f_{tr}^{3dB} = 147GHz$ and the approximation according to eq. (2.20).

terms of its Taylor expansion, the 3 dB roll-off frequency is approximated as $f_{tr}^{3dB} \approx 0.44/\tau_{tr}$. In more realistic diodes, where carriers do not move at a constant velocity, the transit time can be defined as $\tau_{tr} = d_i/\bar{v}$, where \bar{v} is the average velocity of the carriers. The result is usually further simplified as $f_{tr}^{3dB} \approx 1/2\tau_{tr}$, obtaining the following transit time roll-off expression:

$$\eta_{tr} = \frac{1}{1 + (2\tau_{tr}f_{THz})^2} \quad (2.20)$$

The envelope approximation from eq. (2.20) is illustrated in fig. 2.3.

Therefore, the 3 dB transit time roll-off frequency, for a diode with an average velocity \bar{v} , is:

$$f_{tr}^{3dB} \approx \frac{\bar{v}}{2d_i} \propto d_i^{-1} \quad (2.21)$$

The capacitor that determines the RC performance of the diode is the cross-sectional area of the mesa in which the vertical heterostructure is disposed ($C = \epsilon_0\epsilon_r l_x l_y / d_i$). The 3 dB RC roll-off frequency of a p-i-n diode is then

$$f_{RC}^{3dB} = \frac{d_i}{2\pi\epsilon_0\epsilon_r l_x l_y R_A} \propto d_i \quad (2.22)$$

Therefore, there is a trade-off on the design of p-i-n diodes, as making a short intrinsic layer in order to reduce the transit time increases, at the same time, the capacitance of the diode. The diode's mesa area is usually limited by the fabrication technology and by the maximum carrier density that the material can handle to a few micrometers and thus it is not always possible to compensate for the C increment reducing the dimensions of the diode.

2. Photomixing devices for a CW PVNA

The power radiated by an antenna-coupled p-i-n diode is then:

$$P_{THz} = \frac{1}{2} R_A I_0^2 \eta_{tr} \eta_{RC} = \frac{1}{2} R_A I_0^2 \frac{1}{1 + (2\pi f_{THz} R_A C)^2} \cdot \frac{1}{1 + (2\tau_{tr} f_{THz})^2} \quad (2.23)$$

A frequent optimization criteria for p-i-n diode sources is to make $f_{tr}^{3dB} = f_{RC}^{3dB}$. The optimal length of the intrinsic layer is, under this criteria:

$$d_i = \sqrt{v_{sat} \pi \epsilon_0 \epsilon_r A R_A} \quad (2.24)$$

Equation 2.23 shows different approaches that can be used to increase the delivered THz power:

- Reducing diode dimensions (A). As mentioned before, there are limitations because of either technological restrictions on fabrication or the maximum current density that the material of the transport layer admits.
- For $f_{THz} \gg f_{RC}^{3dB}$, $P_{THz} \propto R_A^{-1}$. Therefore, reducing the antenna radiation resistance might improve the overall performance by pushing RC roll-off towards higher frequencies. In terahertz applications such as spectroscopy or PVNA systems, it is necessary to use ultra-wideband antennas. These antennas are, typically, self-complementary and deposited on a semi-insulating semiconductor that has an almost constant radiation resistance of 72Ω , as stated in 2.2. Resonant antennas such as half-wavelength dipoles, with a radiation resistance around 27Ω , might improve the RC roll-off performance of the diode, but they work efficiently only over a narrow frequency range.
- Improving the average velocity of carriers. The transit-time roll-off 3 dB frequency improves with higher average velocities ($\tau_{tr} = d_i/\bar{v}$). In direct-bandgap semiconductors, carriers can be accelerated to velocities much higher than the saturation velocity for a short period of time (typically $\sim 100-200$ fs) which allows strongly improved transit-time performance. This phenomenon is termed as velocity overshoot or quasi-ballistic transport.

Quasi-ballistic transport

There are two main scattering phenomena of electrons in InGaAs which affect the average velocity of carriers, depicted in fig. 2.5:

- At low energies (ΔE_{LO}), **LO-phonon-scattering** reduces the acceleration of electrons, that continue with a constant acceleration and without a significant change of their direction and with little loss of kinetic energy.
- Once the electrons reach the energy of the side valleys ($\Delta E_{\Gamma L}$), **inter-valley scattering** occurs, the direction of motion changes randomly and the average velocity reduces to the saturation velocity.

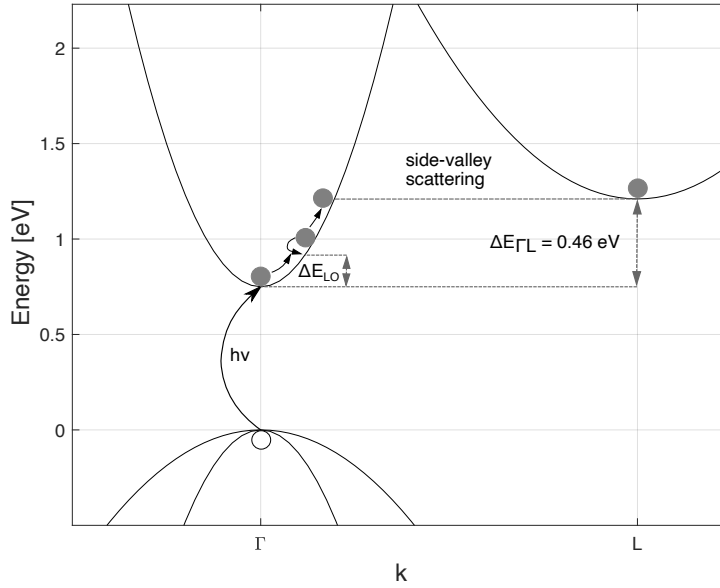


Figure 2.4.: Sketch of the side-valley scattering in InGaAs. LO-phonon scattering reduces acceleration at low energies of ΔE_{LO} . Side-valley scattering will drastically change the direction of motion of electrons that exceed the threshold $\Delta E_{\Gamma L}$, with a value of approximately 0.46 eV for InGaAs. The two bands coinciding at the valence band maximum (center of the Brillouin zone Γ) correspond to the light and heavy holes bands, with the shape of a steeper and a flatter parabola near Γ , respectively.

In order to maximize the distance covered by an electron, the optimum electric field must be applied in order to prevent that the electrons reach a kinetic energy of the side-valley energy $\Delta E_{\Gamma L}$ before transport is completed.

Fields between 10 and 20 kV/cm provide ballistic transport in InGaAs for diodes with intrinsic layers of 200 nm [29]. For lower fields, lower acceleration of electrons reduces the average speed and the distance covered by the electron within a certain time, such as the inverse THz frequency. For higher fields, electrons suffer from inter-valley scattering, reaching saturation velocity within a distance shorter than 200 nm.

While for a diode operating under a saturated regime, average velocities of $v_{sat} = 10^{-7}$ cm/s provides a transit time of $\tau_{tr} = d_i/v_{sat} = 2$ ps for $d_i = 200$ nm, the same distance is covered within 0.25 ps in a diode optimized for ballistic transport, increasing the roll-off frequency from $f_{tr}^{3dB} = 250$ GHz to $f_{tr,bal}^{3dB} = 2$ THz. For diodes that use the velocity overshoot, the penalty paid for increasing the intrinsic layer length by, say, 50% is so severe for transit time performance, that the gain by reduced RC time constant is much less [30].

2.2.4. Realization of THz p-i-n diodes concepts

UTC diodes

UTC diodes are p-i-n diode photomixers for THz generation, invented at Nippon Telegraph and telephone (NTT) [7], in which the main contribution to the photocurrent is due to electrons. This is achieved by attaching a p⁻-type InGaAs absorption layer to the p-contact, followed by a slightly n-type InP collection layer, as illustrated in fig. 2.5. This way, holes are basically generated within the p-contact and electrons are the only charges contributing to the photocurrent, making use, at least partially, of the velocity overshoot shown by electrons [7,31]. One to three additional InGaAsP layers are introduced at the interface between the absorption and collection layer for a stepwise transition of the band gap, avoiding current blocking.

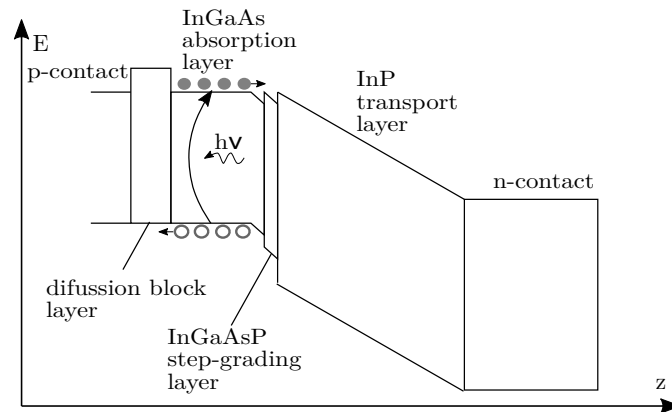


Figure 2.5.: Scheme of the band diagram of a UTC diode.

UTC diodes have three main advantages with respect to standard p-i-n diodes:

1. Much higher operation speed by removing the contribution of the holes to the photogenerated current. The average velocity of an electron is orders of magnitude higher than the one of the heavy holes that limits the high frequency operation of conventional diodes. UTC diodes still suffer from the slow diffusion velocity from the InGaAs absorbing layer to the InP collection layer. This can be overcome by reducing the thickness of the first one without affecting the RC performance of the diode, as the transport length remains constant within the collection layer. This comes at cost of reduced absorption.
2. The much higher carrier velocity also produces a much smaller space charge effect. It still occurs, but as holes do not contribute to the photocurrent, it will only happen at much higher current densities than in p-i-n photodiodes [7].
3. High speed operation can be achieved with very low or even with no bias at all, making use of the built-in field of the junction. This brings simplicity, economy and reliability to the device.

The original NTT design showed a power of $10.4 \mu\text{W}$ at 1 THz with a resonant antenna and up to $2.6 \mu\text{W}$ with a broadband antenna.

Superlattice diode photomixers

The p-i-n diode-based photomixers described in the previous sections suffer from the trade-off between transit time and RC-roll off described in section 2.2.3. For a 3 dB RC roll-off frequency at 1 THz (f_{RC}^{3dB}), assuming a mesa area of $40 \mu\text{m}^2$, an $\epsilon_r = 13$ and a radiation resistance of 72Ω , $d_i = 2\pi f_{RC}^{3dB} \epsilon_0 \epsilon_r A R_A \approx 2.1 \mu\text{m}$. However, for a 3 dB transit time roll-off frequency (f_{tr}^{3dB}) of the order of 1 THz, the optimal length is $d_i < 250 \text{ nm}$ for a typical average velocity in InGaAs of $5 \times 10^7 \text{ cm/s}$.

Döhler et al. proposed in [32] a solution for this compromise. It consists on stacking N p-i-n diodes, optimized for ballistic transport and a certain f_{tr}^{3dB} . The N diodes stack reduces the total capacitance by the number of periods, N . It decouples both roll-off phenomena, as it enables to engineer the capacitance without altering the transit time. Another way of reducing the capacitance would be through reducing the area (i.e. the mesa cross-section) of the diode's mesa. This however, is limited by the maximum current density that the diode can take before breaking.

The main drawback of stacking N diodes in series is that the current is reduced by a factor N and, therefore, it needs of an optical power N times the power used on a regular p-i-n diode in order to obtain a similar performance. This, however, is usually not a restriction as powerful and inexpensive telecom sources and erbium doped fiber amplifiers (EDFAs) are available at 1550 nm. The accumulation of carriers at the n-p junction that forms between two consecutive p-i-n diodes might screen the field, leading to a flat band situation. In order to avoid this phenomenon, it is necessary to design this diode so that electrons and holes are efficiently recombined at the current density at which the device is operating.

The recombination diode consists of semi-metallic ErAs nanoparticles (1 to 2 ML) between the n and p layers. The band diagram of two periods of a superlattice p-i-n diode photomixer is shown in figure 2.6.

Successful operation at 1550 nm has already been shown in ref. [8], using an InGa(Al)As heterostructure. The band gap of the intrinsic layer is graded by increasing the Al content towards the n-contact (higher Al content leads to higher band gap energies). The absorption takes place in only a small region close to the p -contact and almost exclusively electrons contribute to the photocurrent. This enables, at the same time, the possibility to make use of ballistic transport within the individual period, solving the side effect of RC and transit time roll-off trade off by adding the number of periods that drops the capacitance to the desired value as $C \propto N^{-1}$. An Al content below 8% is enough to increase the band gap so that 1550 nm photons are not absorbed.

The best power achieved by a superlattice n -i- pn -i- p photomixer is in the range of $0.8 \mu\text{W}$ at 1 THz [9]. This is achieved with a three-periods device ($N = 3$) with a cross-section of $82 \mu\text{m}^2$, up to six times larger than the UTC from Ito et al. [7]. The device is ballistically optimized for a transit time roll-off with $f_{tr}^{3dB} = 1 \text{ THz}$, but

2. Photomixing devices for a CW PVNA

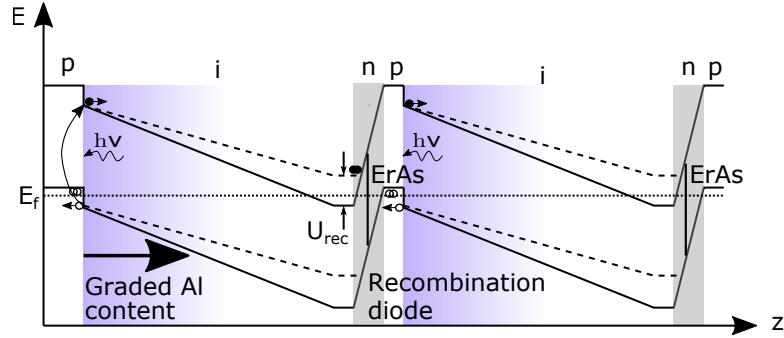


Figure 2.6.: Band diagram of two periods of a superlattice photomixer

Ref.	P_{THz}
n-i-pn-i-p superlattice [8, 32]	0.8 μ W @ 1 THz
UTC Ito et al. [7]	2.6 μ W @ 1 THz (broadband antenna) 10.4 μ W @ 1 THz (resonant antenna)

Table 2.2.: Overview over p-i-n diode-based photomixers

its relatively large dimensions sets the RC roll-off to $f_{RC}^{3dB} = 0.14$ THz. The device provides the 0.8 μ W under operation conditions close to the thermal limits of the device. Previous results with more conservative operations show 0.65 ± 0.15 μ W with 9.5 mA photocurrent obtained from 190 mW of laser power [8]. Thermal limitations are the dominant limitation of n-i-pn-i-p superlattice photomixers. In(Al)GaAs is a very poor thermal conductor with a thermal conductance at least 12 times lower than that of InP. The thick In(Al)GaAs layers (> 750 nm) as compared to ~ 100 nm for UTC diodes further complicates the situation.

2.3. Waveguide-coupled full-ballistic p-i-n diode

In order to mitigate thermal effects, a concept based on single diodes with InP contact layers and with fully ballistic transport across the intrinsic layer similar to the n-i-pn-i-p superlattice design are envisaged. Instead of using a stack of p-i-n diodes, the capacitance is reduced by using very low widths of the mesas that are coupled to a waveguide. The optical signal is coupled from a monolithic integrated optical waveguide in the heterostructure to the active areas of the device along the propagation direction. This approach has already been proven as an efficient coupling method for 1550 nm CW THz sources, achieving up to 5 μ W of THz power at 500 GHz under 25 mW of optical pump [2, 10]. It has also been used as a coupling method in triple-transit-region photodiodes (TTR-PD) working as millimeter wave (mmW) sources, providing up to 1 mW at 110 GHz [11].

2.3.1. Diode heterostructure overview

The device layout integrates the FB p-i-n diode and a passive optical waveguide (POW). The FB p-i-n diode will be optimized to achieve a transit time roll-off 3 dB frequency above 700 GHz while the POW maximizes the coupling of the optical signal to the absorption layers of the diode without compromising its high frequency performance.

The heterostructure consists of the following layers, which are depicted in figure fig. 2.7:

- A 600 nm p⁺-InP top contact layer. The 600 nm initial InP layer works as a p-contact and as well as a thermal buffer due to its better thermal capabilities with respect to InGaAs compounds.
- The 5nm p⁺-InAlGaAs serves to pin the Fermi-level at the valence band edge, removing any barrier for holes to the InP contact.
- The subsequent three n⁻-In(Al)GaAs layers form the intrinsic layer of the photodiode. In order to avoid any significant contribution of slow holes to the photocurrent, absorption is forced to take place in a thin layer with non-zero field near the p-contact of the diode. This is achieved by grading the Al content within the In(Al)GaAs intrinsic layer, increasing the band-gap of the photoconductor beyond the 1550 nm photon energy without introducing jumps on the band gap and therefore avoiding certain scattering mechanisms, similar to the n-i-pn-i-p superlattice photodiodes.
- The n⁺-InAlGaAs is the n-contact layer of the diode.
- The next layers, (n⁺-InP, n⁺-InGaAsP and a second n⁺-InP), form the passive optical waveguide (POW) of the diode, as well as further n-contact layer. The quaternary compound InGaAsP (Q1.26) is used as the high refractive index part of the of the POW (i.e. its core). The Q value corresponds to the band gap wavelength, in microns ($1.26 \mu\text{m} \sim 1 \text{ eV}$).
- All previous layers are grown lattice matched on top of Fe-compensated InP semi-insulating substrate (s.i.-InP:Fe).

2.3.2. Passive optical waveguide (POW)

This section revises the fundamentals of POWs for integration with photodiodes. While the actual design of the waveguide was carried out by collaboration partners at the University of Duisburg-Essen (ZHO, Prof. Stöhr, master thesis of Mr. Peng Lu [33]), a general understanding of the waveguide and coupling principles is key to compare experimental results of samples processed within this thesis to theoretical expectations.

2. Photomixing devices for a CW PVNA

Material	Doping (cm ⁻³)	Thickness (nm)
InP	p ⁺ , Zn: 2*10 ¹⁹	600
In _{0.53} Al _{0.08} Ga _{0.39} As	p ⁺ , Zn: 5*10 ¹⁸	5
grading In _{0.53} Ga _{0.47} As -> In _{0.53} Al _{0.08} Ga _{0.39} As	n ⁻ , Si: ~1*10 ¹⁶	150
In _{0.53} Al _{0.08} Ga _{0.39} As	n ⁻ , Si: ~1*10 ¹⁶	50
In _{0.53} Al _{0.08} Ga _{0.39} As	n ⁺ , Si: ~5*10 ¹⁸	50
InP	n ⁺ , Si: ~1*10 ¹⁸	100
InGaAsP Q1.26	n ⁺ , Si: ~1*10 ¹⁸	290
InP	n ⁺ , Si: ~1*10 ¹⁸	710
s.i.-InP:Fe		

Figure 2.7.: Layered structured of the sample.

The cross-section of the waveguide is depicted in fig. 2.8. A similar monolithically integrated POW has been successfully integrated with Triple-Transit-Region Photodiodes (WG-TTR-PD) [11]. The POW is formed by the quaternary InGaAsP (Q1.26) serving as core and the bottom and top InP layers that form the cladding. At the same time, they must serve as n-contact for the diode. The required donor concentration affects the refractive index and add losses to the POW. The dimensions of the waveguide and a compromise on the maximum tolerable doping level is necessary in order to optimize the optical coupling into the diode.

The width of the top InP layer is 3 μm . The total length of the waveguide is set by the dimensions of the antenna, as it must extend beyond the antenna structure. The length of the waveguide is, thus, determined by the design of the antenna. It varies between 0.45 mm for log-periodic antennas and 0.75 mm for bow-ties.

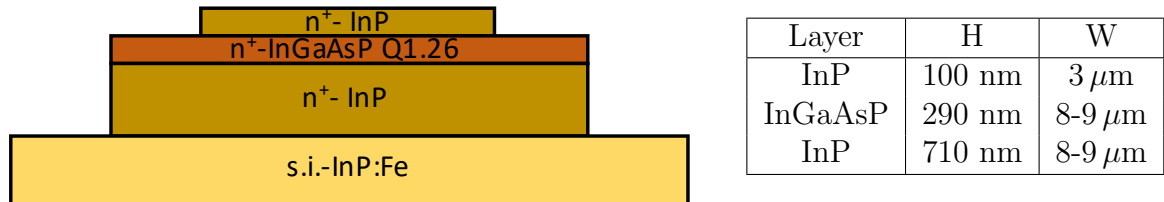


Figure 2.8.: Cross-section of the final designed of the POW from [33]. All layers are doped with Si ($1 \times 10^{18} \text{ cm}^{-3}$).

InGaAsP Q1.26 compound and lattice matching to InP

Attention must be put also to the composition of the quaternary layer. Lattice-matching to the surrounding InP is key in order to avoid mechanical, optical and electrical degradation. For $\text{In}_{1-x}\text{Ga}_x\text{As}_y\text{P}_{1-y}$, the lattice matching condition is obtained from Vegard's law by [34]

$$a(x, y) = xy a_{GaAs} - x(1 - y) a_{GaP} + (1 - x) y a_{InAs} + (1 - x)(1 - y) a_{InP} \text{ \AA} \quad (2.25)$$

For matching all layers to the lattice constant of InP, $a(x, y) = a_{InP}$, the condition for lattice matching is given by

$$x = \frac{0.4526y}{1 - 0.031y} \approx 0.45y \quad (2.26)$$

Under this condition, the band-gap in eV can be obtained for a InP matched InGaAsP compound depending on the As content [34]:

$$E_g = 1.35 - 0.72y + 0.12y^2 \quad (2.27)$$

In this case, the compound band gap was designed as Q1.26 (the energy of a photon at 1260 nm, ~ 0.98 eV), corresponding to a composition with $y = 0.57$ and $x = 0.26$ ($\text{In}_{0.24}\text{Ga}_{0.26}\text{As}_{0.57}\text{P}_{0.43}$).

Losses in the POW

The doping required for the n-contacts modifies the optical characteristics of the POW. With variations on the absorption and the refractive index of the n-InP and n-InGaAsP for different doping levels, the losses and the coupling efficiency are also affected.

There are three mechanisms that determines the absorption of the POW:

1. Interband absorption. When the energy of the incoming photon is larger than the band gap energy of the photoconductor, it will be absorbed. In this case, both InP and InGaAsP (Q1.26) has energy gaps larger than 0.8 eV, such that interband absorption is efficiently prevented.
2. Two photon absorption (TPA). When the band gap is larger than the photon energy, these can still be absorbed in pairs, with a first photon exciting a carrier into a virtual intermediate state before a second photon excite it to the conduction band. This mechanism is quantified by the TPA coefficient, that measures the required spacing in time between two arriving photons per unit area in order to a carrier to be moved to the conduction band.

TPA reduces the intensity of an incoming planar wave with intensity I_0 , through a semiconductor of thickness x and a TPA coefficient β_{TPA} by:

$$\eta_{TPA} = \frac{1}{1 + \beta_{TPA} x I_0} \quad (2.28)$$

For a laser power of 50 mW, assuming a conservative calculation of the intensity in which that it is confined in the InGaAsP core, with dimensions

2. Photomixing devices for a CW PVNA

$3\ \mu\text{m} \times 290\ \mu\text{m}$ ($I_0 = 57.4\ \text{GW}/\text{m}^2$) and is 0.5 mm long, and a TPA coefficient calculated using the theoretical expression that relate it to band-gap energy from [35], the TPA losses results in $\eta_{TPA} = 0.99$. The actual intensity is much lower as a fraction of the mode propagates on the InP cladding of the POW and therefore the 1% losses due to TPA are a conservative estimation.

3. Free carrier absorption (FCA) or intraband absorption. When a photon with an energy smaller than the band gap reaches a semiconductor, it can be absorbed by transferring its energy to move the carriers from the band edge to deeper states within the same band. The absorption coefficient is approximated from classical Drude model for most n-type semiconductors by [36]:

$$\alpha_{FCA} = \frac{Ne^3\lambda^2}{4\pi^2n(m_{eff})^2\mu\epsilon_0c^3}, \quad (2.29)$$

where N is the free-carrier (electron) concentration, λ is the wavelength in vacuum, n is the refractive index, m_{eff} is effective mass of electrons and μ is the electron mobility.

The absorption coefficient for InGaAsP, calculated for an electron mobility $\mu \approx 2500\ \text{cm}^2/\text{Vs}$ (value given in [37] for $y = 0.60$), and an effective electron mass $m^* = 0.06m_0$ [38] is $\alpha_{FCA} = 4.16\ \text{cm}^{-1}$. After 0.5 mm, the total power loss is therefore $-0.90\ \text{dB}$ (i.e. $-1.8\ \text{dB}/\text{mm}$).

The proportionality to electron concentration makes it particularly sensitive to doping and it is, thus, the main source of absorption to be considered when the photon energy is below the band-gap. Following the same classical electromagnetic approach, using the Drude model, it can also be related to the variation for the refractive index under high doping concentrations.

Although higher doping levels make better ohmic contacts with lower serial resistance, the losses on the POW above $1 \times 10^{18}\ \text{cm}^{-3}$ make it impractical and the sample was grown with $1 \times 10^{18}\ \text{cm}^{-3}$ throughout all layers. The compromise with the ohmic contact performance is, nevertheless, not as critical for n-contact as for p-contacts, as GeAu/Ni/Au contacts have been proven to work even for low annealing temperatures on InP [39]. Solutions and experimental data for the ohmic contacts are given in section 3.1.2.

2.3.3. Analytical determination of the coupling length between the POW and the FB-p-i-n diode

The design of the POW and the FB-p-i-n diode must also optimize the optical coupling efficiency to the absorbing region. From mode-coupling theory, it is possible to obtain the distance needed for a total coupling of the optical power (couple length).

The propagating mode in waveguide can be expressed with the phasor

$$\vec{E}(x, y, z) = ae^{-j\gamma z}\vec{E}(x, y) = A(z)\vec{E}(x, y), \quad (2.30)$$

where $\vec{E}(x, y)$ corresponds to the normalized field, $A(z)$ is the complex amplitude and $\gamma = \beta - j\alpha/2$ is the complex propagation constant of the mode in the waveguide.

The power in a waveguide is given by

$$P(z) \sim A(z)A^*(z) \quad (2.31)$$

For simplicity, from now on only the coupling between two identical waveguides is considered, namely the POW and the absorbing layer. This approximation to two identical waveguides is shown in the inset in fig. 2.9. The coupling between two identical waveguides and modes is given by [36]

$$\frac{dA_0(z)}{dz} = -i\gamma A_0(z) - jkA_1(z) \quad (2.32)$$

$$\frac{dA_1(z)}{dz} = -i\gamma A_1(z) - jkA_0(z), \quad (2.33)$$

where k is defined as the coupling coefficient and A_0 and A_1 are the complex amplitudes in the POW and absorber layer, respectively.

Considering as boundary conditions that $A_0(0) = 1$ and $A_1(0) = 0$, the solution for the power in each of the waveguides is

$$P_0(z) = \cos^2(kz)e^{-\alpha z} \quad (2.34)$$

$$P_1(z) = \sin^2(kz)e^{-\alpha z} \quad (2.35)$$

The coupling coefficient k of the first TE mode (i.e. with non-zero E_y component for the geometry defined in the inset of fig. 2.9) between two planar slab waveguides of width w and separated by a distance s is approximated for well confined modes as [40]

$$k = \frac{2p^2q^2e^{-qs}}{\beta(w + 2/q)(q^2 + p^2)}, \quad (2.36)$$

with

$$p^2 = \frac{\omega^2}{c_0^2}n_1^2 - \beta^2 \quad (2.37)$$

and

$$q^2 = \beta^2 - \frac{\omega^2}{c_0^2}n_2^2 \quad (2.38)$$

The value of the real propagation constant β can be obtained from the first real solution of the dispersion relation for an even TE mode [41]

2. Photomixing devices for a CW PVNA

$$\sin p \frac{w}{2} - \frac{q}{p} \cos p \frac{w}{2} = 0 \quad (2.39)$$

From eq. (2.34) and eq. (2.35), it can be seen that, in absence of losses (i.e. $\alpha = 0$), the whole power is transferred periodically between one waveguide to the other after a certain distance known as the coupling length:

$$L = \frac{\pi}{2k} \quad (2.40)$$

Simplifying the heterostructure in fig. 2.7, it is possible to obtain an approximate value for the coupling length between the POW and the FB-p-i-n diode. The two cores correspond to the InGaAs-InAlGaAs layers for the waveguide and the InGaAsP for the POW, with thicknesses of 255 and 290 nm, respectively and refractive indices that vary between 3.5 and 3.6 for In(Al)GaAs (in the different Al and doping compositions [42–44]) and 3.37 in the quaternary layer [42]. The cladding areas correspond to the InP layers, with refractive indices that vary between 3.16 for the p^+ – InP and 3.17 for the s.i. InP [45]. The simplified slab structure and the obtained coupling length for different waveguide separation values s are given in figure 2.9.

The power at a given instant in the parallel identical waveguides, in the absence of losses, is shown in fig. 2.10. It also shows how most of the power is confined within the waveguide core, making eq. (2.36) a valid approximation.

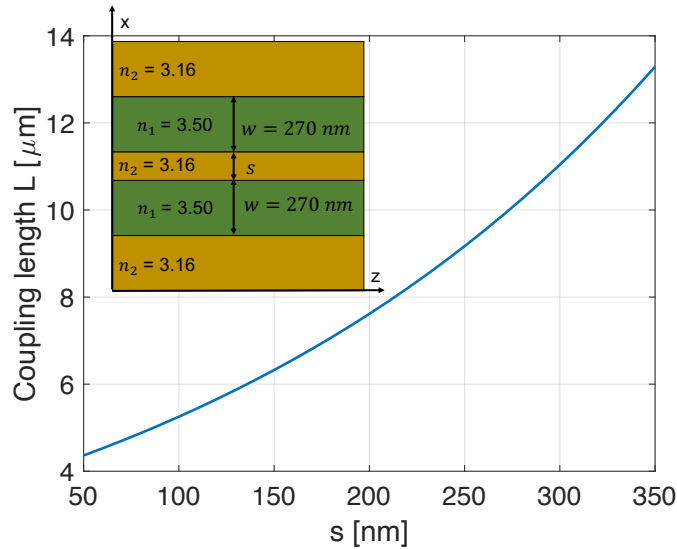


Figure 2.9.: Simplified slab structure used to obtain an estimate of the coupling length between the POW and the FB-p-i-n diode, where s is the thickness of the InP ridge of the POW.

Peng’s study on the waveguide also extends to some other dimensions of the heterostructure and the coupling length. While the guiding core was fixed at the

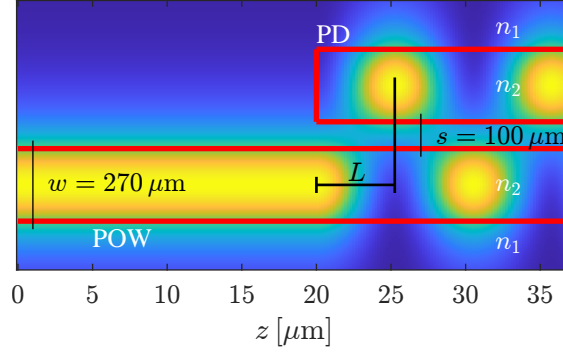


Figure 2.10.: Power coupling between the two planar slab waveguides, POW and the p-i-n diode (P), assuming that there are no losses or absorption and considering the same width $w = 270 \text{ nm}$ for both. The two waveguides, with core and cladding refractive indices of $n_1 = 3.50$ and $n_2 = 3.16$, respectively are separated by 100 nm . The resulting coupling length is $L = 5.25 \text{ }\mu\text{m}$.

same thickness that was successfully demonstrated for TTR- PDs [11], the top InP cladding layer, with a fixed width of $3 \text{ }\mu\text{m}$, is optimized in order to maximize the coupling to the FB p-i-n diode. For that purpose, a numerical analysis calculating the coupling efficiency while ignoring the losses and extinction factors on the POW is carried out, finding an optimal thickness of 100 nm . Peng also demonstrated that the coupling efficiency between the lensed SMF and the POW is almost constant with this top InP cladding layer, improving only by a 3% at the thinner dimensions, where the coupling to the FB-p-i-n diode drops by a 30% [33]. The numerical study also showed a coupling distance of $5 \text{ }\mu\text{m}$ (showing a total distance for re-coupling into the POW of approximately $10 \text{ }\mu\text{m}$). This is in agreement with the results obtained with the approximation using the symmetrical and planar structure in figure 2.9, where the result for the coupling length for a spacing of 100 nm is $5.25 \text{ }\mu\text{m}$.

The above calculation also considers the dimension and doping level of the p^+ -InAlGaAs layer, the only one that will not strongly compromise the high frequency performance of the diode, which are set to 5 nm layer and $5 \times 10^{18} \text{ cm}^{-3} \text{ Zn}$.

Ignoring the losses of the POW, but considering the absorption of the intrinsic layer and the losses associated to the high doped layers within a FB p-i-n diode with dimensions $4 \text{ }\mu\text{m}$ width and $8 \text{ }\mu\text{m}$ length along the waveguide axis (corresponding to approximately 1.5 coupling lengths), the maximum calculated coupling efficiency is 37%, where 32% contribute to the photocurrent, with the other 5% being absorbed at undesired areas of the photodiode [33]. The ideal photocurrent increases to 50% after $17 \text{ }\mu\text{m}$, corresponding to approximately 3 coupling lengths.

2.3.4. FB-p-i-n diode designs

Figure 2.11b shows a top view sketch of a FB-p-i-n diode and how the antenna reaches the contacts passing over a $\sim 1.5 \text{ }\mu\text{m}$ SiN passivation layer that avoids a

2. Photomixing devices for a CW PVNA

shunt by the antenna metalization. There are three different etch steps that define the diode shape: a mesa etch that forms the actual diode containing the active layers, a waveguide etch and a final etch down to the semi insulating Fe:InP substrate. All diode samples are coated by a $\lambda/4$ SiN anti-reflective coating (ARC) and some of them also have the waveguide coated by the isolation layer. As the refractive index contrast between the SiN ($n = 1.96$) and the InP-InGaAsP is very high and the mode is strongly confined, the SiN coating has only marginal influence on the POW operation.

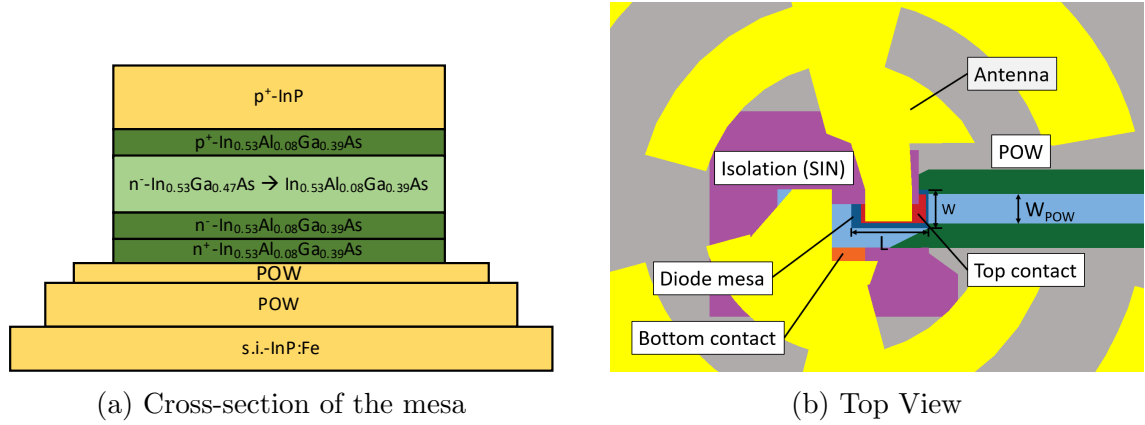


Figure 2.11.: Cross-section of the structured layers of the FB-p-i-n diode. The thicknesses of the layers are not to scale.

The mask includes three different kinds of waveguide-coupled devices for different fabrication tolerances, each of them with mesa lengths of $8 \mu\text{m}$ and $17 \mu\text{m}$. From eq. (2.13) and considering an effective refractive index of the In(Al)GaAs layer of 3.5, a transport layer of 200 nm and an antenna resistance of 72Ω , the RC 3 dB roll-off frequency of the devices are between 127 GHz for the smallest device and 34 GHz for the largest. The results for all devices are summarized in table 2.3.

Device	Width (W)	Length (L)	f_{RC}^{3dB}
Standard	$4 \mu\text{m}$	$8 \mu\text{m}$	127 GHz
Standard	$4 \mu\text{m}$	$17 \mu\text{m}$	60 GHz
Save	$5 \mu\text{m}$	$9 \mu\text{m}$	91 GHz
Save	$5 \mu\text{m}$	$18 \mu\text{m}$	45 GHz
Ultra save	$6.6 \mu\text{m}$	$9 \mu\text{m}$	68 GHz
Ultra save	$6.6 \mu\text{m}$	$18 \mu\text{m}$	34 GHz

Table 2.3.: List of devices with its geometries and the corresponding 3dB RC roll-off frequencies.

The 3 dB transit time roll-off frequency (f_{tr}^{3dB}) is obtained from eq. (2.21). Under fully-ballistic transport occurring in InGaAs at fields between 30 and 40 kV/cm² [30],

2.3. Waveguide-coupled full-ballistic p-i-n diode

it is possible for electrons to travel the whole 200 nm distance of the intrinsic layer in less than 0.5 ps, corresponding to a f_{tr}^{3dB} of more than 1 THz.

3. Fabrication and characterization of a fully-ballistic-p-i-n diode

Large efforts within this thesis consisted on the implementation of the FB-p-i-n diode described in section 2.3.4. In this chapter, the processes of fabricating and characterizing the device is described. Special attention is given to those aspects of the fabrications that entailed the most challenges, such as the creation of good ohmic contacts to the p-InP top layer or the etching of the diode heterostructure, which required of a completely new calibration of the processes in a plasma-assisted dry etching system (which are also given in appendix A). The last part of the chapter provides a comparison to commercial and state-of-the-art systems, as well as the key aspects for improvement of the diode performance and further work.

3.1. Fabrication of the FB-p-i-n diode

3.1.1. Processing overview

Refining the necessary processing techniques has taken a very important part the thesis. Each processing step has been performed using contact-photo-lithography and UV sensitive photoresists in the clean rooms at TU Darmstadt and at the University of Duisburg-Essen, Center for Semiconductor Technology and Optoelectronics ZHO (Prof. Andreas Stöhr).

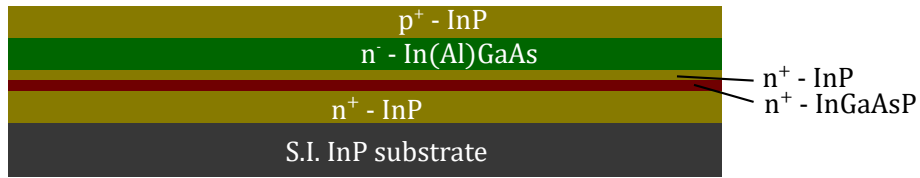
The sample was grown using metalorganic chemical vapour deposition (MOCVD) by ENT, the VIGO systems epitaxy division, in Poland [46].

Plasma etching of the III-V semiconductor etching systems with reliable and vertical etch profiles was carried out at the ZHO with inductively-coupled plasma reactive ion etching (ICP-RIE) system SI 500 from Sentech Instruments GmbH. The anisotropy of the process, which provides the verticality of the diode etch profile, is critical for an optimal performance of the diode at high frequencies.

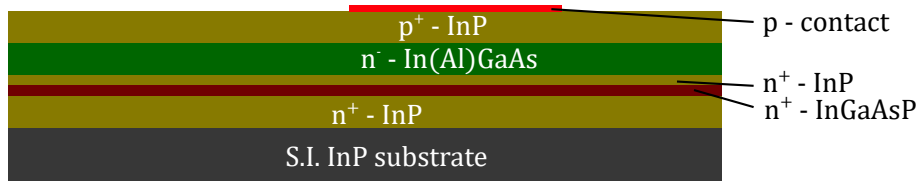
The SiN hard masks for the etching process have been deposited at TU-Darmstadt with an Oxford Plasmalab 100 with plasma enhanced chemical vapor deposition (PECVD) capabilities.

Figure 3.1 shows the step by step fabrication process of the diode. It consists of metal deposition, etching and SiN deposition processes (some of them to be used as mask for the III-V semiconductor etch steps and others as passivation and ARC).

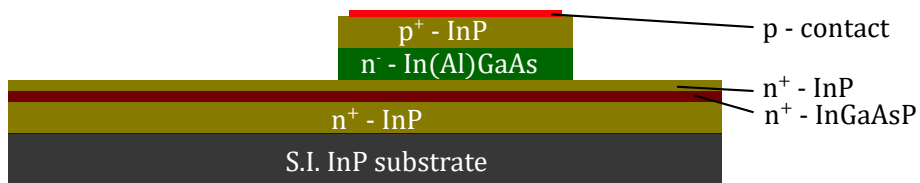
3. Fabrication and characterization of a fully-ballistic-p-i-n diode



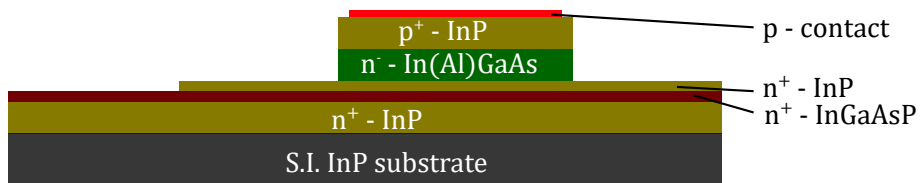
(a) Initial material



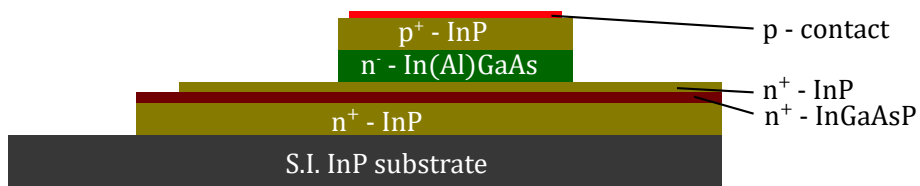
(b) Au/Zn/Au p-contact.



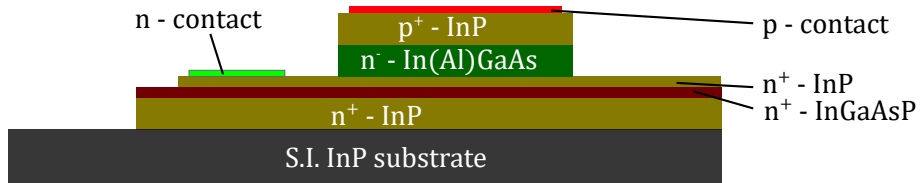
(c) Mesa etching.



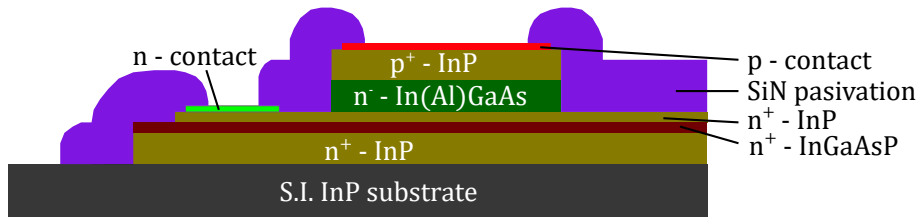
(d) Waveguide etching.



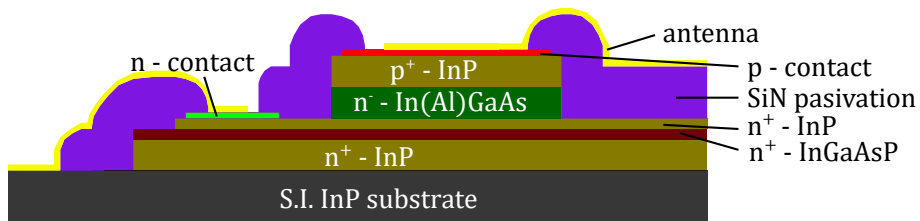
(e) Substrate etching.



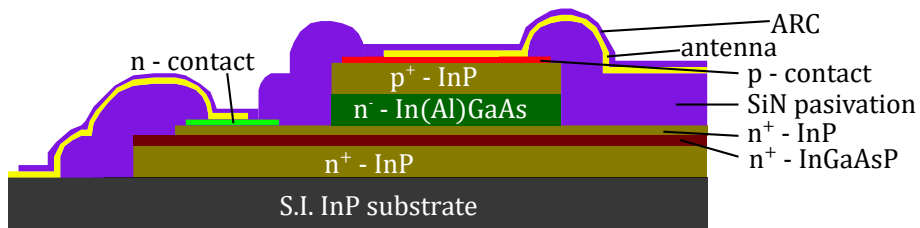
(f) InAu or GeAu/Ni/Au n-contact



(g) Isolation.



(h) Antenna.



(i) ARC.

Figure 3.1.: Fabrication steps of a FB p-i-n diode

3.1.2. Ohmic contacts

A critical element of p-i-n diodes are the metal-semiconductor contacts. They should exhibit the lowest possible resistance, with a voltage drop for any polarity that should be negligible compared to the voltage dropping in the semiconductor. For this reason, it is important to create ohmic contacts. The top- and bottom contacts are deposited in separate metalization steps (see figs. 3.1b and 3.1f), as each of them requires different alloys and metals depending on the type of doping (n or p). They are also different in the antenna metalization step shown in fig. 3.1h.

In order to quantify the quality of an ohmic contact the figure of merit for ohmic contacts is the resistance, defined as [47]:

$$R_C = \left(\frac{\partial J}{\partial V} \right)_{V=0}^{-1} \left[\frac{\Omega}{\text{cm}^2} \right] \quad (3.1)$$

Due to the presence of surface states, oxides and contaminations, an unannealed contact usually behaves like a Schottky contact. Thermionic emission predominates providing a current density of [48]

$$J = A^* T^2 e^{-q\phi_B/kT} (e^{qV/kT} - 1) \quad (3.2)$$

where A^* is the Richardson's constant given by $4\pi m_n k^2/h^3$, h is the Planck's constant, m_n is the effective mass of electrons, k the Boltzmann's constant, T the absolute temperature, ϕ_B the barrier height at the metal-semiconductor interface and q the elementary charge.

The contact resistance is thus

$$R_C \sim e^{\frac{q\phi_B}{kT}} \quad (3.3)$$

However, when the doping concentration becomes high enough (typically above 10^{19} cm^{-3}), the depletion layer narrows, as depicted in figure 3.2b and tunneling starts dominating the current transport, which is [47]

$$J \sim e^{-4\pi W} \sqrt{2m_n(q\phi_B - qV)/\hbar^2}, \quad (3.4)$$

where the size of depletion layer W can be approximated as $\sqrt{(2\epsilon/qN_D)(\phi_B - V)}$. The resistance of a contact with a highly doped semiconductor is, thus

$$R_C \sim e^{\frac{4\sqrt{m_n\epsilon} \phi_B}{\sqrt{N_D} h}}, \quad (3.5)$$

where N_D is the donor concentration (doping level).

Equations (3.3) and (3.5) show two strategies in order to create ohmic contacts, if not both of them simultaneously: choosing metals that introduce a small barrier height and introducing high doping concentrations that narrow the barrier and allow tunneling mechanisms through it. The most common solution to create ohmic contacts in compound semiconductors consists of creating a very thin and heavily doped layer. Even for a lightly doped semiconductor, such a high doped layer can be

achieved by diffusing a metal into the semiconductor. This is achieved by choosing of an appropriate metal and annealing at elevated temperatures under protective atmosphere or vacuum.

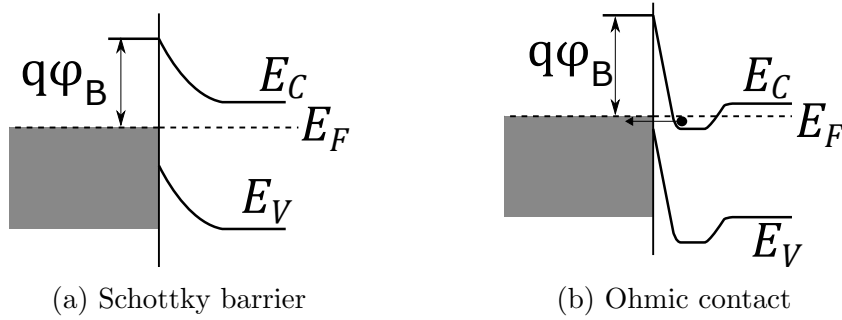


Figure 3.2.: Energy band diagram of a rectifying metal-semiconductor rectifying diode and an ohmic contact.

While low resistance is the main figure of merit for ohmic contacts, they should fulfill the following criteria:

- **Reproducibility:** the alloy and diffusion of the metals (and metalloids) into the semiconductor is dependent on the alloy composition, the temperature and atmosphere of the annealing process and the state and cleanliness of the sample surface when the metal is deposited. For this reason, reproducibility of ohmic contacts is often compromised. The formation of thin oxide layers affects the overall ohmic contact formation process. An homogeneous surface treatment can be carried out to ensure a clean and homogeneous contact. It is usually based on a short dip in an acid solution. A typical surface treatment consists of the dip in a 50% HCl solution in H₂O for InGaAs and GaAs compounds. For InP, etched by HCl, the solution is reduced to 2 M (~ 16% HCl concentration volume in H₂O for a 48% concentrated grade), level at which the oxides are attacked but not the InP [49].
- **Reliability:** the ohmic contact must be stable under the operation conditions of the diodes. They should be able to withstand the maximum operative temperature of the device.
- **Compatibility:** the formation of ohmic contacts should not modify other parts of the diode. An example of this is the diffusion of dopants induced by annealing into others layers different to the ones involved on the ohmic contact. It must also stay unaltered during other steps of the fabrication, for example, under the temperatures during plasma assisted dry etching.

Formation of p-contacts (fig. 3.1b)

For InP, p-type ohmic contacts are more challenging due to the large barrier height of most metals to p-InP [50]. Furthermore, p-type III-V compounds oxidize much

3. Fabrication and characterization of a fully-ballistic-p-i-n diode

easier than n-type, complicating the good formation of ohmic contacts [51].

The p-contact, which is the first processing step of the sample, is also one of the most critical and challenging ones. The only solution available for the metal was Zn, which is the same dopant used on the sample growing. As the annealing process will cause diffusion of the Zn from the contact metal stack into the semiconductor, while at the same time, the dopant Zn will diffuse inside the structure from the p-type layer into the intrinsic region, choice of the appropriate temperature is of highest importance. A few nm diffusion of the p-dopant into the intrinsic layer can be tolerated. Longer diffusion length would dope the intrinsic layer noticeably and alter the band curvature, yet increasing the transit time of carriers.

The linearity of the contacts was measured using two of the four contacts of a hall-cross. Two hall crosses, with squared contacts of $150\ \mu\text{m}$ sides, are implemented on the mask to access n and p-contact layers. In this work, only ohmicity and an upper limit of the resistance are determined.

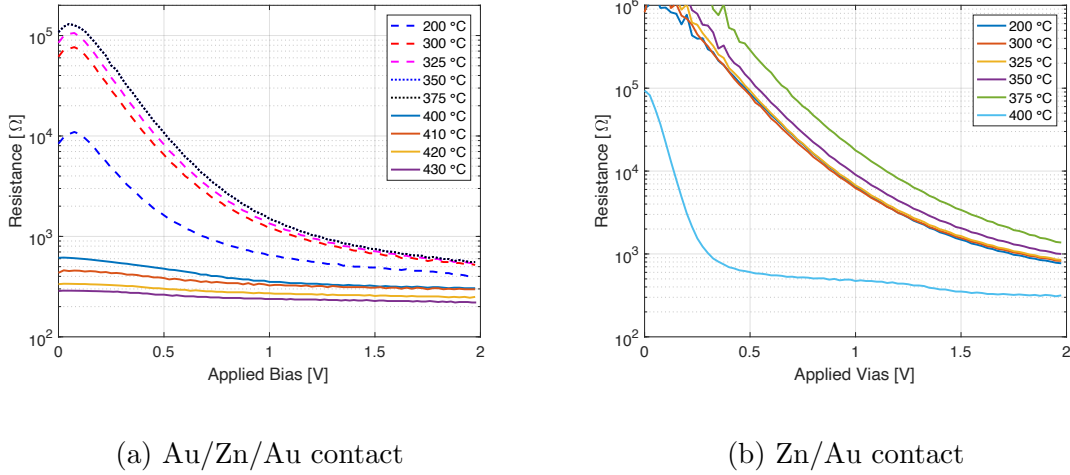
Two different solutions have been investigated. The first samples were processed with an evaporated Zn/Au contact with a thicknesses of 24 and 120 nm, respectively, and annealed in several steps at increasing temperatures under a 10^{-2} bar N_2 atmosphere for 30 s each step. The second sample followed similar steps but with a Au/Zn/Au contact with 10, 24 and 120 nm thickness, respectively. Figure 3.4 shows that, for both cases, the Zn started diffusing and creating an ohmic contact at temperatures higher than $400\ ^\circ\text{C}$, with Au/Zn/Au having a better ohmic behavior. Although better results could be obtained at higher temperatures, the fact that the Zn is also used as dopant dictates that samples have to be annealed only at the lowest temperatures in which an ohmic behavior was observed. In particular, Au/Zn/Au p-contacts annealed at $410\ ^\circ\text{C}$ have been used for the rest of the fabricated samples. The p-contacts are reannealed when the n-contacts are formed and, in some cases, the annealing temperature for the n-contacts are higher than for the p-type.

Other options of metal compositions that allow for annealing below $400\ ^\circ\text{C}$ for the p-contact were explored. In: Au contacts did not show ohmic behavior even at $375\ ^\circ\text{C}$, with a resistance about 5 times higher than the Au:Zn: Au contacts. Sn: Au was also explored up to $160\ ^\circ\text{C}$, without successful results.

Formation of n-contacts (fig. 3.1f)

Two different bottom contacts have been used: first, n-contacts of In: Au layers (20:100 nm) were evaporated. This contact is annealed even at a temperatures as low as $200\ ^\circ\text{C}$, with very good ohmic behavior through the hall-cross as it is shown in Fig.3.5. The main inconvenience for this contact is the poor behavior of In at high temperatures, becoming a potential problem under high power (i.e. high temperatures) operation.

A second solution using GeAu/Ni/Au was evaporated on the subsequent processing runs that provided functional devices. Annealing at $430\ ^\circ\text{C}$ (and, thus, re-annealing also the Zn/Au p-contact), the FB-p-i-n diodes have good exponential



(a) Au/Zn/Au contact

(b) Zn/Au contact

Figure 3.3.: V-R curves measured after different annealing steps of the studied contacts. The values correspond to the total resistance through the Hall contacts (two contacts and the semiconductor layer resistance)

IV characteristics reaching values under 100Ω at 2 V of forward applied bias, corresponding to good formed ohmic n- and p-contacts. It has been also observed that in absence of annealing the samples exhibited a total resistance already under 200Ω , which is consistent with the findings in [39]. Unannealed n-contacts are an option for future work.

3.1.3. Plasma-assisted dry etching

Side-illuminated p-i-n diode samples require three different etching steps: diode mesa, waveguide formation and n-contact layer etching down to the semi-insulating Fe:InP substrate. In addition to that, other plasma processes were necessary to shape SiN layers, which have been used as insulation layer, ARC and hard masks for the III-V semiconductor etching processes.

The III-V semiconductor etching has been performed with a Sentech SI 500 ICP-RIE system in the Duisburg-Essen University, using a $\text{Cl}_2:\text{N}_2$ recipe at 170°C . Typical photoresist hard bakes at this temperature, deforms and requires further complex removing processes. For this reason, plasma deposited SiN layers have been used as hard mask for the III-V etching steps. The SiN was deposited using an Oxford Plasmalab 100 with PECVD capabilities at TU Darmstadt.

Most of the III-V plasma assisted recipes are strongly selective to SiN, with selectivities beyond 5 (see appendix A), not requiring thick layers. Over a heterogeneous sample containing different binary, ternary and quaternary compounds (Al-graded In(Al)GaAs, InP and Q1.26 InGaAsP), however, it is critical to calibrate the speed at which the SiN is etched during a III-V semiconductor etching process. As the SiN is etched at more homogeneous rates than the heterostructured semiconductor material, the etch depth can be calculated more accurately from the estimation of

3. Fabrication and characterization of a fully-ballistic-p-i-n diode

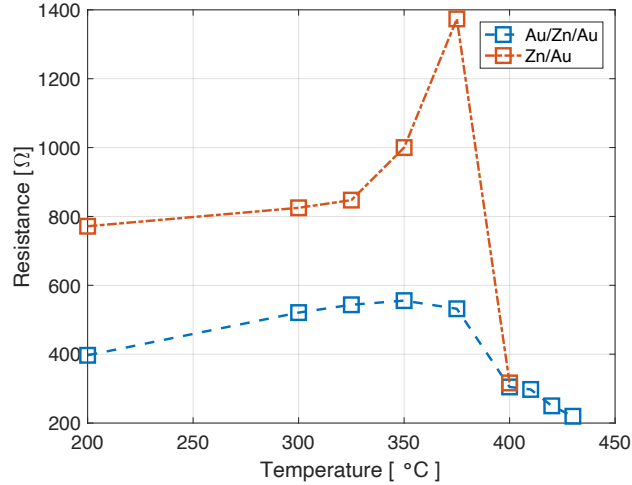


Figure 3.4.: Resistance measured through two contacts of the p-contact Hall cross at different temperatures for Zn/Au and Au/Zn/Au contacts. The depicted value is obtained from the derivative of IV characteristic curve at 2 V.

the remaining SiN mask thickness. The description of the used recipes and a more detailed description of the depth estimation process during processing is given in detail in appendix A.

1. On a clean surface, the SiN is deposited. The thicknesses range from 200 nm to 600 nm and are typically chosen to have a sufficiently thick layer left at the end of the process, that will be etched away after structuring.
2. The sample is coated with photoresist and the mask is formed using photolithography.
3. The photoresist pattern is transferred to the SiN with a plasma assisted process. III-V semiconductors behave as stop layers for the fluoride-based processes which are used. However the process duration should not exceed much beyond the time required to etch the deposited SiN layer, because a long exposition to plasma might polymerize already exposed side-walls of the diode or cause physical damage to the top surfaces. In order to avoid this, the etching time is targeted for the whole thickness of the SiN, followed by a visual inspection. This ensures that there is no visible SiN left on the exposed areas, proceeding with an extra 10 to 15 % additional etching, as very thin layers, of a few tens of nm, might be difficult to identify visually.
4. Photoresist is removed in an acetone dip for 5 minutes, followed by an isopropanol dip. The topmost surface of photoresist gets cross-linked during the dry plasma process, becoming insoluble in acetone and remaining on the

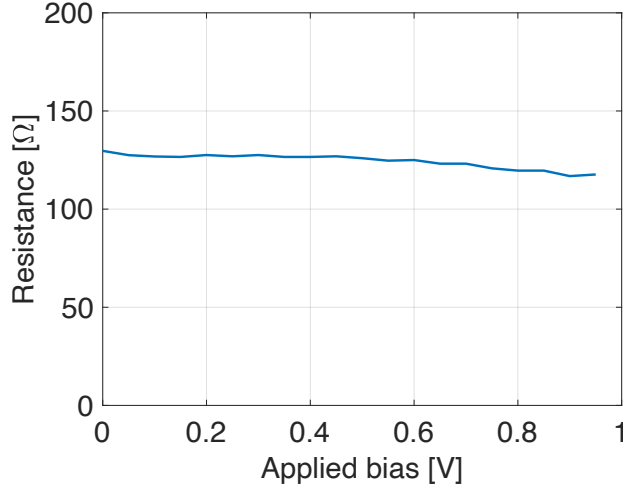


Figure 3.5.: Resistance measured through the n-contact Hall-cross with a In:Au metallization annealed at 200 °C.

surface. A short O₂ plasma etching process removes it completely (see appendix A).

5. After lithographic definition of the SiN hard mask, the actual etching is done with Cl₂ based dry-etching plasma process. The exact procedure differs for each of the layers:
 - For the mesa etching (fig. 3.1c), a single Cl₂:N₂ dry etching process is performed aiming to stop between 100 to 150 nm above the 100 nm InP waveguide layer, followed by a short wet etch where the InP layer acts as etch stop. H₃PO₄:H₂O₂:H₂O (1:1:4) and H₂SO₄:H₂O₂:H₂O (1:8:50) solutions were used. Both are very selective to crystal axis, generating different slopes and under-etchings on the structures. The small thickness of the remaining layer to be wet-etched causes only insignificant side wall inclination. Both etching solutions have rates of ~ 900 nm/min and, thus, requires only a few seconds to reach the InP stop layer.
 - The waveguide etching (fig. 3.1d) is done in a single step, aiming for the 100 nm of the InP waveguide. The non-constant etching rate during the first seconds of the plasma process complicates repeatability of etch depths. However, the effort on the cleaning and preconditioning of the chamber allowed to reduce the uncertainty to ± 10 nm. Precondition and cleaning protocols are also further explained in appendix A.
 - For the substrate etching (fig. 3.1e), where a thickness beyond 1000 nm must be reached, dry-etching is performed in two or more steps. After each step, the thickness is checked and the processing time is adapted according to the deviation from estimations. Once the estimated depth reaches the semi-insulating substrate, the resistivity of the sample is

3. Fabrication and characterization of a fully-ballistic-p-i-n diode

checked in order to ensure that it was actually reached. Wet etching is not practical at this step because the bottom layer of the n-contact is also InP, i.e., the same material as the substrate without any etch stop layer.

6. The SiN hard mask is removed with the same $\text{CF}_4:\text{O}_2$ recipe that is used during its formation.

3.1.4. Other processes

After the etching of the sample and the formation of the top and bottom contact (the former is the first step of the sample processing), the remaining steps are the antenna deposition, with the previous required isolation, and the ARC coating.

Passivation (fig. 3.1g)

The insulation or passivation step allows the antenna to connect to the n- and p-contact without shunting the diode. It consists of a SiN layer deposited with a PECVD process of ~ 1500 nm. The processing is similar to the mask formation in semiconductor etching. The main difference is that the photoresist is hard baked in order to round its shape, transferring this rounded edge to the underlying SiN with the $\text{CF}_4:\text{O}_2$ plasma etching process.

Antenna metalization (fig. 3.1h)

The antenna consists of a Ti:Au (~ 20 nm:200 nm) metalization deposited by evaporation. The height to be covered by the metallization is up to $3 \mu\text{m}$ due to the height of the diode plus the passivation layer. For this reason, it is necessary to evaporate the sample under an angle with a rotative holder, so that a proper connection is achieved in all angles.

Anti reflective coating (ARC) (fig. 3.1i)

The last step is SiN coating. It consists of a $1/4\lambda$ SiN layer deposited with PECVD, which corresponds to approximately 220 nm at 1550 nm, and it has three main purposes:

1. It acts as an anti-reflective coating of the top-illuminated samples.
2. Provides a mechanical protection.
3. Prevents the active layer from oxidation and other external agents.

3.2. Characterization of the FB-p-i-n diode

3.2.1. Experimental setup

The CW characterization of the FB-p-i-n diode was performed using a frequency-tunable table-top photomixing setup driven by a 1550 nm laser system where the THz frequency is tuned by the frequency difference of two DFB lasers. The scheme of the characterization setup is shown in fig. 3.6. Two receivers were used: a commercial HHI/Toptica photoconductor and an ErAs:InGaAs photoconductor, like the one described in [13]. The laser signal is coupled using a lensed fiber with a focal distance of $14\ \mu\text{m}$ and a spot size of $2.5\ \mu\text{m}$ into the POW exposed at a cleaved edge of the chip. Prior to incoupling, the optical power is amplified using an erbium doped fiber amplifier (EDFA).

The fiber is aligned to the POW using a high precision 3D positioning stage. The THz beam is radiated downwards by the antenna with the aid of a hyper-hemispheric HR Si-lens. A TPX lens collimates the THz beam, followed by a planar mirror that aligns it parallel to the optical table. A second TPX lens focuses the beam onto the Si-lens of the receiver.

The THz signal is modulated at 12 kHz by the bias of the FB-p-i-n diode. The bias amplitude and offset are optimized in order to obtain the maximum amplitude of the THz signal within certain safety margins. This is meant to prevent the break-down of the device, paying special attention to the forward bias. Both bias modulation and lock-in electronics are part of the proprietary hardware from Toptica Photonics AG.

The output current of the detector photoconductor is pre-amplified by a transimpedance amplifier (PDA-S) before being measured by the lock-in amplifier.

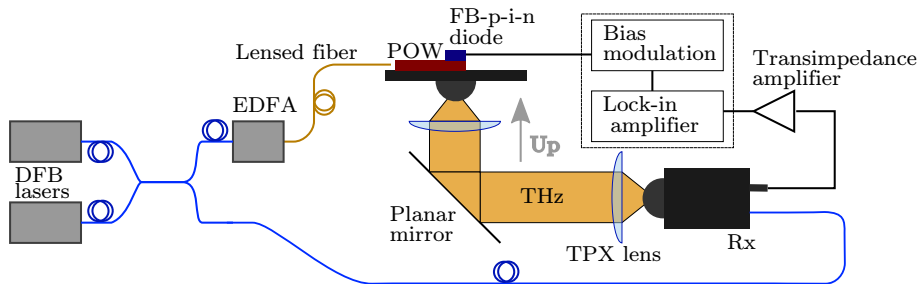


Figure 3.6.: CW setup for the characterization of the FB-p-i-n diodes.

3.2.2. Some practical considerations

Stable and reliable operation of the setup required some general considerations. The most relevant were:

3. Fabrication and characterization of a fully-ballistic-p-i-n diode

Protection circuit

After damaging some devices, probably occasioned by transients occurring during the alignment of the setup, a simple protection circuit was built with the schematic from fig. 3.7. A Zener diode with $V_z = -3.3\text{ V}$ limits the reverse bias to around -3.3 V and the forward bias to $\sim 0.7\text{ V}$. A small serial resistance limits the current that the FB-pi-n diode takes from transients, also when they are too fast for the Zener diode. Subsequent samples were able to work for long periods of time without suffering from breakdowns or degradation.

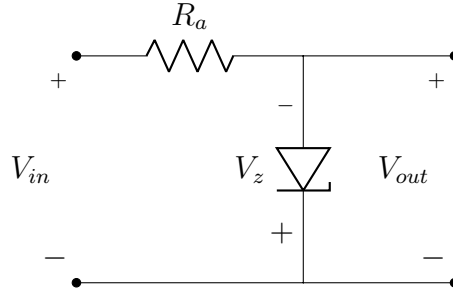


Figure 3.7.: Protection circuit.

Hyper-hemispherical Si lens

The sample is placed on top of a high-resistive (HR) silicon lens in order to improve the outcoupling efficiency, increasing the numerical aperture. The typical solution consists of using aplanatic hyper-hemispherical lenses. In aplanatic silicon lenses, an outcoupling beam emerges as a divergent beam with an angle of approximately 30° without spherical aberration [52]. The aplanatic condition, for a hyper-hemispherical lens with radius r and refractive index n is fulfilled when the distances between the tip and the planar side of the lens is

$$R_{hyp} = r \left(1 + \frac{1}{n} \right) \quad (3.6)$$

Equation (3.6) assumes that the substrate is part of the lens (i.e. it has the same refractive index and its thickness is included in R_{hyp}). This is, however, not the case in this thesis, where the substrate is semi-insulating (SI) Fe:InP with a thickness of $630\ \mu\text{m}$ and $n_{InP} = 3.54$ at THz frequencies. The interface of the sample substrate with the HR-Si lens, with $n_{Si} = 3.42$, introduces additional refraction. The optical characteristics of the substrate were measured using THz-TDS. The data (refractive index and absorption coefficient up to 3.5 THz) are shown in appendix B.

Figure 3.8 shows the deviation of the hyper-hemisphericity from the aplanatic condition for a substrate of thickness s . The refraction at the interface will produce spherical aberration, but it can be approximated to an aplanatic lens for small incidence angles from the approximation of Snell's law ($n_1\alpha_1 = n_2\alpha_2$).

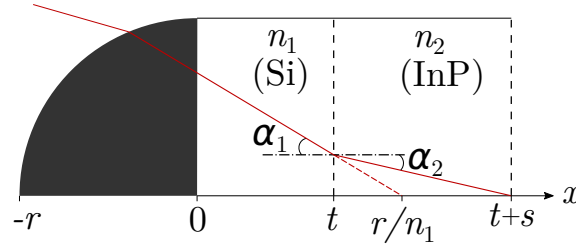


Figure 3.8.: Approximated aplanatic condition of a hyper-hemispherical lens of thickness $R_{hyp} = t + r$ with a substrate of thickness s .

The required thickness of the hyper-hemisphere (defined by $R_{hyp} = r + t$ in fig. 3.8) is thus

$$R_{hyp} = r \left(1 + \frac{1}{n_1} \right) - s \frac{n_1}{n_2} \approx 1.29r - 0.97s \quad (3.7)$$

The lenses available had a $r = 5$ mm radius and the sample was $s = 630 \mu\text{m}$ thick, corresponding to a required lens thickness of $R_{hyp} = 5.84$ mm. As a lens with this hyperhemisphericity was not available, it was configured using a hyper-hemispherical lens with $R_{hyp} = 5.7$ mm and a planar HR-Si spacer of 0.18 mm, making a total thickness of 5.88 mm.

Lensed fiber alignment and stability

A common issue during the experiment was the mechanical instability of the optical coupling between the lensed fiber and the POW. With a lensed fiber with a working distance of less $14 \mu\text{m}$ and a spot diameter of only $2.5 \mu\text{m}$, vibrations and mechanical limitations caused drifts of the photocurrent with time, despite using a floating table and highly precise mechanical positioning stages.

Reproducibility and sufficient stability was achieved by feeding the POW out of focus. After aligning the focal point to the POW at comparatively low optical power (typically 25 mW), the fiber was pulled back out of focus till the photocurrent dropped to 50% of the original value. Then the target photocurrent was set by increasing the pump current of the EDFA.

3.2.3. Terahertz Characterization

A device with a $18 \mu\text{m}$ long mesa and $d_i = 200$ nm integrated with a bow-tie antenna has been characterized using the Toptica Photonics AG CW system.

THz spectrum

A recorded THz spectrum of the device is shown in fig. 3.9. It was obtained with a photocurrent of 11 ± 1 mA and a bias modulation between -3 V and 0.6 V with a total optical power of 250 mW, but with the lensed single-mode fiber (SMF) placed

3. Fabrication and characterization of a fully-ballistic-p-i-n diode

out of focus by one Rayleigh length (a 50% photocurrent reduction). The receiver was a commercial photoconductor from Toptica Photonics AG/HHI operated with 22 mW optical power. For an integration time of 300 ms (ENBW \approx 1.7 Hz), the dynamic range is 37 dB at 1 THz. The whole band up to 1.75 THz was covered using two different configurations of the DFB lasers.

The results are compared with the spectrum obtained using a n-i-pn-i-p superlattice photomixer and an ErAs:InGaAs photoconductor [53]. The n-i-pn-i-p superlattice transmitter was top-illuminated with a laser power of 80 mW using an EDFA, obtaining a photocurrent of 3.7 mA at -1 V. The detector was illuminated with 26 mW. The transmitter is bias modulated between -2 and 1.2 V at around 12 kHz.

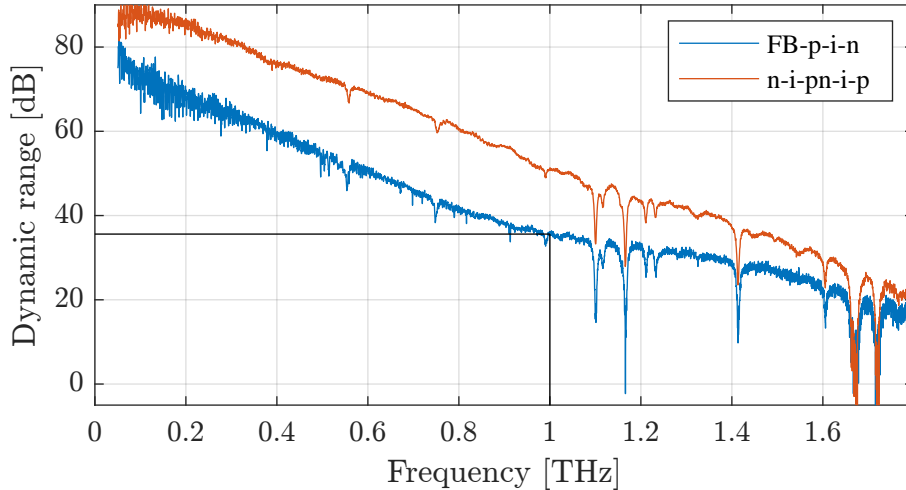


Figure 3.9.: Spectrum measured with the Toptica Photonics AG 1550 nm system. The dynamic range is calculated for an integration time of 300 ms. The spectrum is measured in two different ranges that require of two different configurations among the three DFB lasers available.

The intrinsic layers in both devices (the FB-p-i-n diode and the n-i-pn-i-p) are identical ($d_i = 200$ nm), except that the n-i-pn-i-p comprises a stack of 3 diodes and the FB-p-i-n diode is slightly n-doped (Si: $\sim 1 \times 10^{16}$ cm $^{-3}$), as shown in fig. 2.7. The transit time roll-off is thus very similar if the applied bias allows ballistic transport. The RC roll-off is significantly different in each device. The FB-p-i-n diode, with an area of 5×18 μ m, presents a 3 dB roll-off frequency (f_{RC}^{3dB}) of around 45 GHz. The n-i-pni-p, with an area of 10×9 μ m and 3 periods, features an RC roll-off with $f_{RC}^{3dB} = 135$ GHz.

Figure 3.9 shows that the FB-p-i-n diode, despite having an overall worse efficiency that strongly reduces the emitted power and a much unfavorable RC roll-off that degrades the spectrum by further 10 dB above 200 GHz, approaches to the n-i-pn-i-p at higher frequencies. This is more evident when the effect of the RC roll-off is eliminated and the spectra are normalized to their peak power, as shown in fig. 3.10. While both devices feature similar responses below 800 GHz, the FB-p-i-n diode outperforms the efficiency by more than 10 dB at higher frequencies.

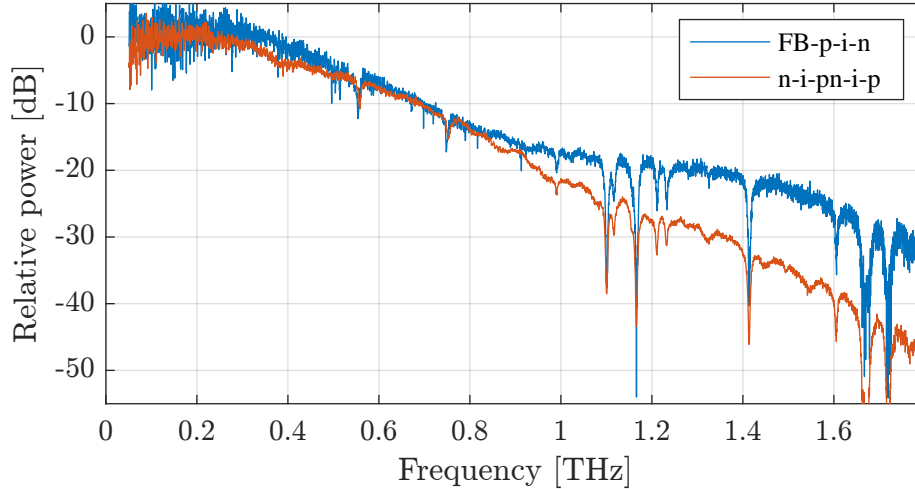


Figure 3.10.: Relative power after eliminating the effect of the RC roll-off in the FB-p-i-n diode and the n-i-pn-i-p superlattice photomixers. The power is normalized to the peak amplitude in order to compare the frequency response of the two devices.

This implies that, if the overall efficiency of the diode is improved in order to obtain similar peak THz powers than the n-i-pn-i-p, its response at high frequencies might be close to the state of the art dynamic range (DNR), of around 70 dB at 1 THz [2] with commercially available emitters.

There are many factors that might explain the better relative performance of the FB-p-i-n diode at higher frequencies, including the different experimental setups, that used devices with different antennas and different receivers, as well as different optics (the n-i-pn-i-p setup used parabolic mirrors in stead of the TPX lenses shown in fig. 3.6).

Less severe field screening might be a possibility. The optimal reverse bias to achieve ballistic transport increases approximately logarithmically with optical power, as accumulated photogenerated carriers induce a forward bias in the p-i-n and recombination diodes of the n-i-pn-i-p superlattice [29]. With only one period and a better thermal performance, the FB-p-i-n can handle ballistic transport at higher optical powers, which, at the same time, require higher reverse bias. Furthermore, the n-doped intrinsic layer of the FB-p-i-n is meant to compensate some of the field screening and, thus, reach more favorable, i.e. less bent, band profiles with high optical powers that keep transit times short.

The THz current provided by the receiver was measured at individual frequencies for different photocurrents of the FB-p-i-n diode. The results in fig. 3.11 show that the source features a saturation current around 10 mA. This saturation is more evident at lower biases, indicating a screening of the built-in field, which can be partially resolved with higher biases [29] restoring the optimal field for ballistic transport over a considerable part of the transport length.

3. Fabrication and characterization of a fully-ballistic-p-i-n diode

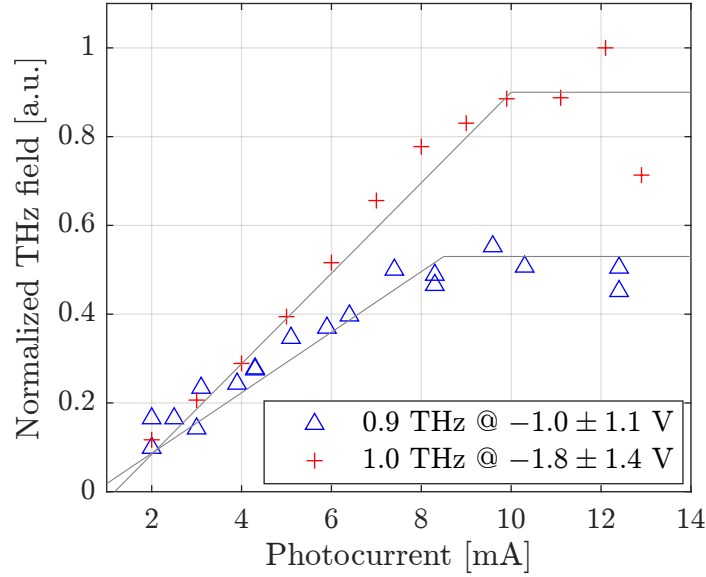


Figure 3.11.: THz field at different photocurrents. The gray lines are guides for the eye.

3.2.4. Photocurrent comparison to top-illuminated diodes

In order to quantify the optical to THz efficiency improvement due to the improved incoupling by the POW (side-illumination), top-illuminated samples were also processed on the same chip and characterized.

With side-illumination, the maximum measured photocurrent at 25 mW was 3.5 mA, corresponding to an external quantum efficiency of 11%, more than four times higher than by top-illumination, with only 0.8 mA at the same power level, corresponding to an efficiency of 3%.

There are two immediate factors that reduce the quantum efficiency: first, if a planar incidence on the POW is considered, 27% of the power is reflected (-1.37 dB loss). Furthermore, the guided power is absorbed by free carrier absorption in the POW (eq. (2.29)). For a POW length of $\sim 800 \mu\text{m}$, corresponding to the devices with bow-tie antennas, an additional -1.44 dB is lost, totaling to -2.81 dB or a factor of 0.52. Thus the external quantum efficiency of the FB-p-i-n diode reaches 21%, up to seven times higher than with top-illumination.

The IV characteristics of the top- and side-illuminated samples are shown in fig. 3.12. The side illuminated samples were measured by defocusing the lensed fiber to obtain a better stability, as discussed in section 3.2.2. Several measurements are taken using different optical powers. The reading of the power meter is corrected in each measurement by the photocurrent drop due to defocussing. The top-illuminated samples are measured directly at the focal point of an aspheric lens. Figure 3.12 shows that the photocurrent is for two different optical powers, namely 22 and 32 mW, above 4 times higher in the side-illuminated diodes, in agreement with the previous measurement using 25 mW if reflections and losses of the POW are not

considered.

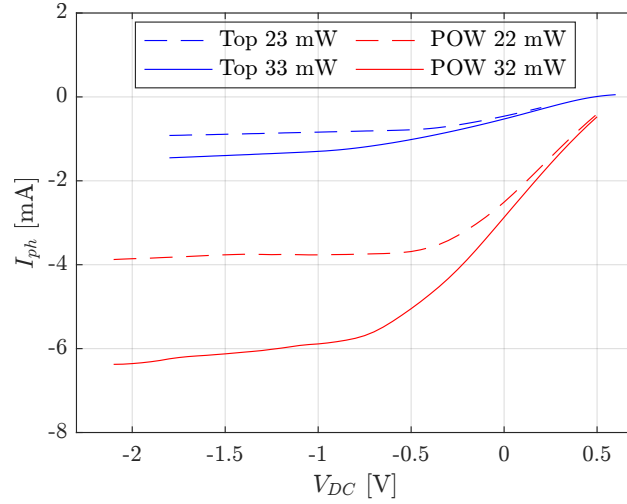


Figure 3.12.: IV characteristics of top- and side-illuminated samples.

3.3. Conclusions and further work

The POW-coupled photomixer is superior in terms of optical incoupling by a factor of 7 as compared to a top-illuminated sample. In future work, the emitted THz power needs to be improved by a redesign of the p-i-n structure in order to surpass the state of the art, which currently is about 15-20 dB better. Well designed and optimized n-i-pn-i-p superlattice photomixers have indeed shown an absolute higher power in figs. 3.9 and 3.10, There is a room for improvement concerning the FB-p-i-n diode, that features a comparatively better characteristics at high frequencies. This is a promising result which might overcome the limitations found to increase the power from n-i-pn-i-p devices at given laser powers, as it is now able to tolerate higher operating photocurrents with an improved thermal conductivity. Furthermore, single period diodes allow optical coupling through POWs, which is difficult in n-ipn-i-p superlattices. The requirement of Er in n-i-pn-i-p superlattice diodes further aggravates the commercial implementation of n-i-pn-i-p devices, which is not an issue with single period diodes only consisting of materials available at any foundry for telecom diodes.

There are some aspects that are yet to be solved which should strongly improve the performance of the diode:

- It is unclear if the Zn dopant for the p-contact layer affects the diode performance by diffusing into the intrinsic layer at the annealing temperatures needed for the p and n-contact formation. Diffusion is certain to be happening, as Zn is both part of the p-contact metallization alloy and the dopant and the former needs to diffuse to form a good ohmic contact. A diffusion of

3. Fabrication and characterization of a fully-ballistic-p-i-n diode

the Zn of some nm can be tolerated, but it will dope the intrinsic layer and introduce a curvature of the band structure, degrading the transit times and the overall performance of the diode. There were no means to know the exact state of the layers involved during or after the processing. Some effort was put to substitute the Zn from the contact alloy with a metal requiring lower annealing temperatures, but it resulted to be the most successful, without an available substitute. A better solution consists of changing the dopant of the p-contact layer to C, instead of Zn. Carbon does not show any noteworthy diffusion, however, was not available at the growth facility where the diodes were epitaxially grown. If Zn must be used as a dopant, still some improvement could be achieved reducing the annealing temperature of the n-contact, that has to be deposited after the p-contact due to the process flow. It has been already demonstrated that GeAu/Ni/Au forms ohmic contacts in n-InP even without annealing [39]. A clean and oxide-free surface must be then assured. Longer HCl dips for oxide removal in solutions with concentrations under 2 M could be useful in this case, while only short dips of around few tens of seconds were performed during the processing of the samples in this thesis.

- Several processing steps require further improvement:
 1. The waveguides (and the diodes) featured rough edges caused by a production or manipulation error of the mask, which was identified a posteriori. This might be resulting in excessive scattering losses.
 2. Isolation and antenna metalization (the latter with thickness below 250 nm due to processing limitations) were challenging steps due to the height of the diode structure, surpassing the 2 μm . Bad connections of the antenna were found to be the reason of many high-resistive devices on different samples. This height was increased by conservative overetching into the semi-insulating substrate of an extra 200 nm. The lack of an etch stop layer between the n-InP bottom contact and the Fe:InP substrate makes it difficult to hit the exact endpoint, but with a good calibrated etching process, the additional height could be minimized.
- The measurement setup showed some instability. It was partially solved by feeding the POW out of focus, but still some long-term drifts were noticed. Photocurrent drops of around a 20% were typical over a period of 30 minutes, the approximate duration of measurements with long integration times. This could explain the sudden drop of the roll-off above 1.4 THz in fig. 3.9. A lot of attention was put on the refinement of the mechanical and structural aspects of the setup, including the design of the aluminum structures to fit the lensed fiber holders at the correct heights. A promising improvement is expected from a mechanically stiff, small-sized mount where both fiber and devices are glued, similar to a package of a commercial DFB diode. This however, only allows for characterization of singular devices.

- The samples were grown with a CVD process. In the past, better performance was shown with MBE grown samples, (e.g. better control of the material properties which may improve the mobility, reduced unintentional doping, ...). Shifting the processes might help to improve the high frequency performance of the FB-p-i-n diode.

4. THz time-domain spectroscopy of liquids

4.1. Transmission THz-TDS of liquids

4.1.1. Basics of terahertz time-domain spectroscopy

Terahertz time-domain spectroscopy (THz-TDS) has become a powerful tool for material analysis and inspection in the THz range between 0.1 and 10 THz. It offers an attractive and cost-efficient solution in comparison to other technologies that try to fill the gap from the radio frequency (RF) and optical sides, while making use of technologies and components from both.

One of the most powerful characteristics of THz spectroscopy is that it enables the inspection through optically opaque substances [54]. Among many applications, THz-TDS has been used to determine optical constants of semiconductors [55, 56], as well as different kinds of plastics [57]. It has also been proven to be effective to characterize liquids, including hydrocarbons, for example to determine motor oil contamination with water [58] and glycol [59] or the composition and properties of biodiesel [60, 61].

The basic scheme of a THz-TDS setup is depicted in fig. 4.1. The laser pulse, divided into two different branches, is directed towards two photoconductive antennas that work as emitter and detector. When it reaches the source, the photogenerated carriers in the photoconductive material are accelerated by a DC bias towards an antenna, that radiates a THz pulse. The THz pulse travels through free space and is affected by the material characteristics of the sample before reaching the detec-

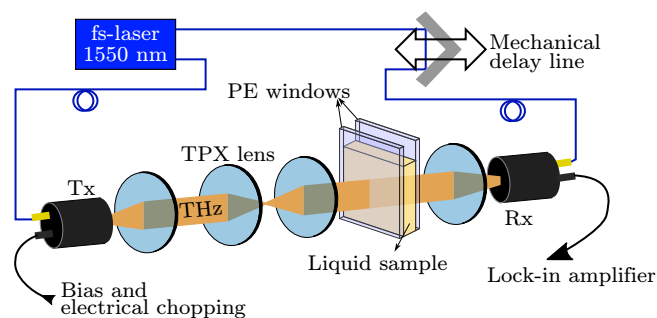


Figure 4.1.: Setup of the THz-TDS system for the measurement of liquid samples (© 2021 IEEE).

4. THz time-domain spectroscopy of liquids

tor. When the THz pulse and the other branch of the femtosecond pulse overlap temporally in the receiver, a signal that is proportional to the electric field of the THz pulse is generated (and thus making the system phase sensitive). As the optical pulse is much shorter than the THz pulse, a time delay between the pulses results in a raster scan of the THz field. The most usual way of scanning the THz pulse in different instants consists on introducing a mechanical delay line in one branch of the optical path, typically on the detector side, allowing the THz pulse to be recorded within a time span set by the movement of the delay stage. This probe scheme on the detector makes THz-TDS very robust against background noise. Once the pulse is recorded, usually averaging over several periods of the femtosecond laser repetition rate, a frequency domain signal can be obtained with a Fourier transformation. Comparing the amplitude and phase of the frequency domain signals, recorded with and without the sample, the spectral characteristics of the material are obtained.

4.1.2. Extraction of material parameters of liquids

Measuring and obtaining the optical constants, refractive index (n_s) and absorption coefficient (α), of liquids with THz-TDS implies considering the effects introduced by the cuvette, because the beam travels not only through the sample, but also through the windows that conform the cuvette, as depicted in figure 4.2. Although their effect can be calculated and subtracted, choosing windows that exhibit low losses preserves the signal to noise ratio (SNR) and the bandwidth of the system. Low losses also allow to use thicker windows, simplifying the post-processing. While the echoes of thick layers are easily eliminated with a window around the main pulse, with thinner layers the echoes overlap with it, hindering the post-processing and having to deal with the etalon effects. For a typical pulse-width of $t_p = 10$ ps, the minimum thickness required for a polyethylene (PE) layer ($n_w \approx 1.5$) to avoid overlapping is

$$d_w > \frac{c_0 t_p}{2n_w} \approx 1 \text{ mm}, \quad (4.1)$$

where c_0 is the speed of light in vacuum.

In order to obtain the optical constants, n_s and α , at least two signal recordings must be done: one reference measurement with the empty cuvette, providing the field measurement of the pulse $a_{ref}(t)$, and another with the cuvette filled with the liquid sample, $a_{sam}(t)$. After windowing the time traces over the main pulse, the Fourier transform of the resulting pulses provides the spectra $A_{ref}(\omega)$ and $A_{sam}(\omega)$, ideally free of Fabry-Perot oscillations.

The windowing of the main pulse is an important step to consider. Ultimately, all pulses are windowed as they are recorded over a limited time. Reducing the time window and giving it the appropriate shape has an important effect on the results of the spectrum and sample characteristics extraction. The Fourier-transform of the windowing mask must be as narrow as possible for the given width (duration) and its spectrum should have high side lobes height (SLH), so that they have the minimum

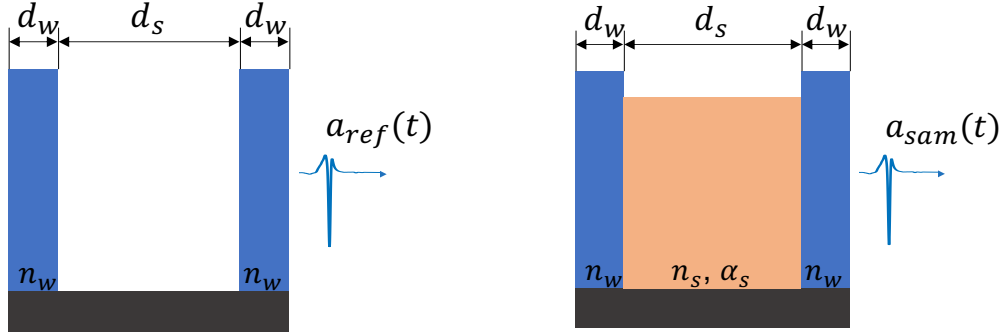


Figure 4.2.: Schematic of the cuvette configuration under reference and sample measurements of the pulses $a_{ref}(t)$ and $a_{sam}(t)$.

impact on the spectrum [62]. Among others, *hann* or *bartlett* windows are used for these purposes and are integrated in many signal-processing software toolboxes. Throughout this work, *hann* windows (also known as *hanning*) have been used, as they have excellent characteristics and can be controlled with only one parameter (the window length, d_w). All points outside the time window are immediately set to zero. Their number ultimately determines the sampling resolution of the spectra, which can be now artificially changed by simple zero-padding without altering the measured pulse. This resolution refers only to sampling, as the tail of zeroes do not add any additional information. This chapter also presents in section 4.2.8 the selection of the window length as a method to correct artifacts produced by the phase unwrapping without introducing additional systematic errors.

From the spectra of the pulses after applying the window, $E_{ref}(\omega)$ and $E_{sam}(\omega)$, the field transmission measurement is defined as

$$t(\omega) = \frac{E_{sam}(\omega)}{E_{ref}(\omega)} = \frac{t_{ws} e^{-j \frac{\omega}{c_0} N_s(\omega) d_s} t_{sw}}{t_{wa} e^{-j \frac{\omega}{c_0} n_0 d_s} t_{aw}}, \quad (4.2)$$

where the transmissions from air to window and window to air cancel out and are therefore omitted. $n_0 \approx 1$ is the refractive index of air and N_s is the complex refractive index, in which the sign of the imaginary part (κ_s) is chosen accordingly to the sign criteria of the propagating signal, so that $\kappa_s > 0$ represents losses. For the propagating signals defined in eq. (4.2) with $\exp(-j\omega nd/c_0)$, the complex refractive index is thus

$$N_s(\omega) = n_s(\omega) - j\kappa_s(\omega) \quad (4.3)$$

The complex factors t_{xy} are the Fresnel transmission coefficients for the field at the interfaces between air (*a*), window (*w*) and liquid sample (*s*), given by

$$t_{xy}(\omega) = \frac{2N_x(\omega)}{N_x(\omega) + N_y(\omega)} \quad (4.4)$$

Substituting and simplifying yields:

4. THz time-domain spectroscopy of liquids

$$t(\omega) = \frac{(N_w(\omega) + n_0)^2 N_s(\omega)}{(N_w(\omega) + N_s(\omega))^2 n_0} e^{-j \frac{\omega}{c_0} (n_s(\omega) - n_0) d_s} e^{-\frac{\omega}{c_0} \kappa_s(\omega) d_s} \quad (4.5)$$

Defining the complex Fresnel factor $r(\omega)$ as:

$$r(\omega) = \frac{(N_w(\omega) + n_0)^2 N_s(\omega)}{(N_w(\omega) + N_s(\omega))^2 n_0} = |r(\omega)| e^{j \angle r(\omega)}, \quad (4.6)$$

where $\angle r(\omega)$ is the phase of the Fresnel factor. The complex field transmission from eq. (4.5) can be rewritten in polar form as:

$$t(\omega) = |t(\omega)| e^{j\phi(\omega)} = |r(\omega)| e^{-\frac{\omega}{c_0} \kappa_s(\omega) d_s} e^{-j \left[\frac{\omega}{c_0} d_s (n_s(\omega) - n_0) - \angle r(\omega) \right]}, \quad (4.7)$$

where $\kappa_s(\omega)$ has been substituted by the absorption coefficient $\alpha(\omega)$, related by:

$$\frac{\alpha(\omega)}{2} = \frac{\omega}{c_0} \kappa_s(\omega) \quad (4.8)$$

The expressions for $n_s(\omega)$ and $\alpha(\omega)$ as a function of $\phi(\omega)$ and $|t(\omega)|$ are extracted from eqs. (4.6) and (4.7), obtaining:

$$n_s(\omega) = n_0 - \frac{c_0}{\omega d_s} (\phi(\omega) - \angle r(\omega)) \quad (4.9a)$$

$$\alpha(\omega) = -\frac{2}{d_s} \ln \left[\frac{|t(\omega)|}{|r(\omega)|} \right] \quad (4.9b)$$

The two unknowns, n_s and α , appear in both equations and the system must be solved numerically. However, assuming that the imaginary part of the refractive index, κ_s , is sufficiently small for the liquid sample, a constant and real window refractive index (n_w) and unity air refractive index ($n_0 = 1$), the Fresnel factor, $r(\omega)$, becomes real and transforms eq. (4.9) into:

$$n_s(\omega) = 1 - \frac{c_0}{\omega d_s} \phi(\omega) \quad (4.10a)$$

$$\alpha(\omega) = -\frac{2}{d_s} \ln \left[|t(\omega)| \frac{(n_s(\omega) + n_w)^2}{n_s(\omega)(n_w + 1)^2} \right] \quad (4.10b)$$

With this approximation, both parameters are obtained without requiring of any numerical approach. The following section presents a recursive method to solve eq. (4.9) without simplifying assumptions.

4.1.3. Iterative algorithm for optical constants extraction

Unlike solid slab samples, where the sample thickness and the complex refractive index are tightly related and need of more complex numerical methods to obtain precise values of the optical constants [56], the sample thickness can be uncoupled from the optical constants for liquids, as they can be determined from the characteristics of the reference measurement, where the empty cuvette length is the sample thickness.

The two equations from eq. (4.9) are still tightly related, with the phase change introducing phase and amplitude changes. In most cases, these are negligible and eq. (4.9) can be approximated by eq. (4.10). For precise measurements of very lossy or thin samples, accurate results can be obtained with a recursive algorithm:

1. Compute the initial values of $n_s(\omega)$ and $\alpha(\omega)$ with eq. (4.10).
2. Calculate the complex refractive index:

$$N_s(\omega) = n_s(\omega) - j\kappa_s(\omega) = n_s(\omega) - j\alpha(\omega)\frac{c_0}{2\omega}$$

3. With the new value of N_s , obtain the complex Fresnel factor $r(\omega)$ from eq. (4.6)
4. Obtain the two new values of n_s and α from eq. (4.10).
5. Check if the new n_s and α have converged, comparing them with the previous iteration. If the stop criteria (i.e. the selected precision) is not fulfilled, use them as a new input from point 2.

A quantitative demonstration of this algorithm is shown in fig. 4.3, where the residuals at each iteration, calculated as the difference between n_s and α with the previous step, are displayed. It shows a quick convergence, reaching the double float resolution after only 3 and 4 iterations. It also demonstrates the validity of the approximation from eq. (4.10). The error committed by the approximation corresponds to the residual of the first iteration, below 0.001% for both constants. The data used in this analysis corresponds for the most lossy sample and the thinner cuvette from chapter 5.

A comparison of the iterative resolution with the simplified analytic approach in eq. (4.10) shows, for all samples investigated in this work that the iterative solution is unnecessary. The value of κ_s is around three orders of magnitude smaller than n_s . Therefore, the approximation from eq. (4.10) is used throughout this work.

4.2. Error Sources of THz-TDS of Liquids

4.2.1. Introduction and Overview

In order to reduce the error committed on the refractive index, a detailed inspection and knowledge of the error sources is a must. A good understanding of all systematic

4. THz time-domain spectroscopy of liquids

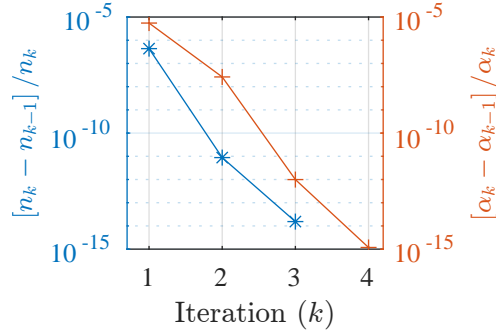


Figure 4.3.: Step residuals of the algorithm to solve n_s and α in eq. (4.9). The errors corresponds to the root mean square (RMS) of the normalized error (e.g. $[n_k(\omega) - n_{k-1}(\omega)]/n_k(\omega)$) at the frequency points between 0.5 and 1.5 THz.

and random error sources allows to identify those aspects that must be controlled and those that can be further simplified in order to obtain a precise and efficient system.

A summary and index of all errors described in this chapter can be found in table 4.1.

4.2.2. Systematic errors due to approximations

There are three general considerations which are usually taken in order to simplify the analysis of the optical constants. One of them is approximating the refractive indices by its real parts at the Fresnel factor (that is, $r(\omega) \approx (n_w + n_s)^2/(n_s(1 + n_w)^2)$) in eq. (4.9), leading to eq. (4.10). The second approximation consists of the assumption of a constant window refractive index or a negligible error of the characterization of the windows' optical constants. The third one is the assumption of a unity air refractive index ($n_0 = 1$). While the first and the last one will have an effect on both optical constants, a change or uncertainty on the refractive index of the cuvette windows will only produce a deviation of the absorption coefficient.

Complex refractive indices in the Fresnel terms

The Fresnel terms approximation is the one assumed in order to obtain equation (4.10) from (4.9), along with $n_0 = 1$. It consists of assuming that the complex term of the refractive index is negligible on the terms corresponding to the Fresnel coefficients ($r(\omega)$), i.e. $\kappa_s = 0$. The error, Δn^C , defined as the difference between the n_s values obtained using the approximation from eq. (4.10) and the actual value from eq. (4.9) ($\Delta n^C = n_{s,approx} - n_{s,actual}$), both with $n_0 = 1$, can be calculated as:

$$\Delta n^C(\omega) = -\frac{c_0}{\omega} \angle r(\omega), \quad (4.11)$$

where $\angle r$ is the phase of the complex Fresnel factor given by equation (4.6).

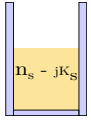
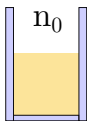
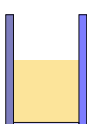
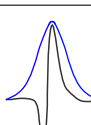
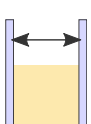
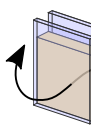
Error source		Type	Approx. value	Eqs.
Processing and approximation				
Complex refractive index		S	$\Delta n^C \sim 10^{-6}$ $\Delta \alpha^C \sim 10^{-5} \text{ cm}^{-1}$	(4.11) (4.12)
Unity refractive index of air		S	$\Delta n^a \sim 10^{-4}$ $\Delta \alpha^a \sim 7.5 \times 10^{-5} \text{ cm}^{-1}$	(4.16) (4.17)
Window refractive index		S	$\Delta n^C \sim \text{n. a.}$ $\Delta \alpha^a \sim 0.24 \Delta n_w / d_s$	(4.14)
Time-signal windowing		S	$\Delta n \sim 10^{-6}$	Sect. 4.2.8
Sample thickness (section 4.2.3)				
Cuvette thickness		S/R	($\sigma_d = 14 \mu\text{m}$, $d_s = 15 \text{ mm}$): $\sigma_{n,d} = 4 \times 10^{-4}$ $\sigma_{\alpha,d} = 5 \times 10^{-4} \text{ cm}^{-1}$	(4.19) (4.20)
Cuvette rotation		S/R	($\xi = 1^\circ$): $\Delta n^\xi = 7 \times 10^{-5}$ $\Delta \alpha^\xi = 3 \times 10^{-4} \text{ cm}^{-1}$	(4.37) (4.38)
TDS system resolution		R	($\delta_t = 0.033 \text{ ps}$, $d_s = 15 \text{ mm}$): $\sigma_{n,\delta} = 6 \times 10^{-6}$ $\sigma_{\alpha,\delta} = 10^{-4} \text{ cm}^{-1}$	(4.50) (4.51)
Amplitude error (section 4.2.6)				
Noise		R	($d_s = 15 \text{ mm}$): $\sigma_\alpha = 3 \times 10^{-4} \text{ cm}^{-1}$ @ 1 THz $\sigma_\alpha = 5 \times 10^{-3} \text{ cm}^{-1}$ @ 2 THz	(4.55) (4.58)

Table 4.1.: Summary of error sources. The type of error correspond to systematic (S) or random (R). For the former, the error is given in deviation terms (Δn and $\Delta \alpha$). Random errors are expressed in terms of the standard deviations (σ_n and σ_α). All errors are calculated for the measured values of sample NA000 in chapter 5 at 1 THz ($n_s = 1.468$ and $\alpha = 0.66 \text{ cm}^{-1}$).

4. THz time-domain spectroscopy of liquids

The deviation of the absorption coefficient, given by the difference between the approximated and the actual values, $\Delta\alpha = \alpha_{approx} - \alpha_{actual}$, is:

$$\Delta\alpha^C(\omega) = \frac{-2}{d_s} \ln \left[|r(\omega)| \frac{(n_w + n_s(\omega))^2}{(n_w + 1)^2 n_s(\omega)} \right], \quad (4.12)$$

where $|r(\omega)|$ is the amplitude of the complex Fresnel factor given by equation (4.6).

For a value of $\kappa_s = 3.58 \times 10^{-3}$, obtained from the most lossy sample in chapter 5 ($\alpha = 3 \text{ cm}^{-1}$ at 2 THz and considering a real value for n_w and $n_0 = 1$, the errors are $\Delta n^C \approx 7 \times 10^{-8}$ and $\Delta\alpha^C \approx 1.5 \times 10^{-5} \text{ cm}^{-1}$).

A qualitative analysis of this approximation was also demonstrated in fig. 4.3, where the first points provide an approximate empirical RMS value over the frequency points between 0.5 and 1.5 THz, from the data corresponding to the most lossy sample from chapter 5, of $|\Delta n^C|/n_s \approx 10^{-6}$ and $|\Delta\alpha^C|/\alpha \approx 10^{-5}$.

Variations of the window refractive index

An error in n_w will not have any impact on the measurement of the refractive index, n_s , as it does not depend on n_w and any possible effect is compensated by the quotient between the reference and the sample spectra. It is different in the case of the absorption coefficient, α , where the Fresnel term accounts for the different transmission coefficients at the dielectric interfaces and a variation of Δn_w introduces an error in α .

Given a deviation of the window refractive index Δn_w and $n'_w = n_w + \Delta n_w$, the deviation of the absorption coefficient α' from the actual one, α , is

$$\Delta\alpha^w(\omega) = \alpha(\omega)' - \alpha(\omega) = -\frac{2}{d_s} \ln [|t(\omega)|K'(\omega)] + \frac{2}{d_s} \ln [|t(\omega)|K(\omega)], \quad (4.13)$$

where, $K^{(\prime)}(\omega) = (n_s(\omega) + n_w^{(\prime)})^2 / (n_s(\omega)(1 + n_w^{(\prime)})^2)$, leading to:

$$\Delta\alpha^w(\omega) = \frac{2}{d_s} \ln \left(\frac{K(\omega)}{K'(\omega)} \right) = \frac{2}{d_s} \ln \left(\frac{(n_s(\omega) + n_w)^2 (1 + n_w + \Delta n_w)^2}{(n_s(\omega) + n_w + \Delta n_w)^2 (1 + n_w)^2} \right) \quad (4.14)$$

For typical values of $n_w = 1.525$, $n_s = 1.465$ and $d_s = 5 \text{ mm}$ and for a Δn_w as big as 0.1, the systematic error committed in the absorption coefficient is $\Delta\alpha = 0.05 \text{ cm}^{-1}$. Below this value of Δn_w , eq. (4.14) is approximately linear and can be approximated, for the typical values mentioned above, by

$$\Delta\alpha^w \approx 0.24 \frac{\Delta n_w}{d_s} \quad (4.15)$$

It is, therefore, a systematic error with a relatively small impact. Throughout this work, the value was found experimentally to $n_w = 1.525$ for all frequencies.

Unitary refractive index of air

The error committed assuming $n_0 = 1$ in eq. (4.9) (already taking real values for $N_s(\omega)$ and n_w) can be obtained using a similar approach as in the previous section, given that $n_{s,n_0=1} = n_{s,n_0} + \Delta n^a$ and $\alpha_{s,n_0=1} = \alpha_{s,n_0} + \Delta \alpha^a$, as:

$$\Delta n^a = -(n_0 - 1), \quad (4.16)$$

and

$$\Delta \alpha^a = \frac{2}{d_s} \ln \left[\frac{n_0(n_w + 1)^2}{(n_w + n_0)^2} \right] \quad (4.17)$$

Nitrogen purge is used throughout this work in order to eliminate water vapour absorption lines from the spectra. As the exact content in nitrogen and the residual atmospheric components within a non-fully sealed chamber, and therefore the refractive index of the atmosphere, were unknown, the value for all calculations was set to $n_0 = 1$. The errors caused by this assumption, given an air refractive index of 1.00027 (typical value for 1 atm at room temperature) and a cuvette length of 15 mm, are $|\Delta n^a| = 2.7 \times 10^{-4}$ and $|\Delta \alpha^a| = 7.5 \times 10^{-5} \text{ cm}^{-1}$. As the cuvette thickness is calculated in most cases using reflexions of the main pulse, the assumption of $n_0 = 1$ will also have a small effect on the obtention of the sample thickness.

4.2.3. Systematic and random errors due to cuvette dimensions

The cuvette dimensions are directly related with the optical constants and, in many spectroscopy problems, is another unknown of the measurement problem. The sample thickness corresponds to the inner size of the cuvette when the beam is propagating straight and collimated.

Cuvette dimension error can be separated into two different error sources: random and systematic errors. The qualification of an error within these two groups differs depending on the sample preparation and measurements proceedings. Usually, errors occurring evenly in all measurements or changing in a time scale larger than the individual measurements are considered systematic. Among the different possible causes of a cuvette dimensions error, the most relevant are:

- Cuvette structure: Cuvettes are fabricated using several pieces, such as windows, spacers and gaskets. An uncertainty after mounting the sample occurs, introducing a random error. This error might also be systematic when, for example, windows get deformed after several mounts or usages.
- Cuvette misplacement: If the sample is placed under a certain angle, it will cause the beam to travel through a longer distance. If all samples are measured without demounting the cuvette from the setup, it will be a systematic error. In the most typical scenario, each time a new sample is measured the cuvette is removed from the setup in order to exchange the liquid or the cuvette itself, becoming a random error.

4. THz time-domain spectroscopy of liquids

- Cuvette thickness measuring tolerance: either it is mechanically measured, for example with a caliper, or through the time-domain signal, looking at the echoes, the thickness measurement introduces a random error. The resolution error with a discrete scale can be modelled with a rectangular probability density function. For a measuring device resolution δ_l , the variance in the thickness is $\delta_l^2/12$ [63].

All previous errors can be modeled as thickness errors. Therefore, it is sufficient deriving the error of the optical constants (Δn and $\Delta\alpha$) for a certain thickness deviation Δd . Error derivations for cuvette misplacement or resolution will be obtained for specific expressions substituting Δd .

Random errors are expressed in terms of uncertainty, which will be here denoted with the standard deviations, σ_n and σ_α , for each of the optical constants, in contrast to systematic errors or deviations given by Δn and $\Delta\alpha$.

In this section, the expressions for the propagation of an error of the sample thickness (Δd) to the optical constants are given, followed by a justification about using the same expressions for the propagation of the uncertainty, given a standard deviation σ_d that translates into a standard deviation of the optical constants σ_n and σ_α . In other words, the propagation of the thickness deviation Δd into optical constants deviations (Δn and $\Delta\alpha$) is used to obtain the uncertainty propagation of a random change of the thickness, σ_d , into σ_n and σ_α .

The error expressions for positioning (rotation) and resolution errors, which substitute either Δd of σ_d , the latter for random processes, by the corresponding expressions, are provided in the following sections 4.2.4 and 4.2.5, respectively.

Sample thickness error propagation

The direct relation between the optical constants, n_s and α , and the sample thickness as $n_s(\omega) - 1 \propto 1/d_s$ and $\alpha \propto 1/d_s$, as shown in equation (4.10), makes it one of the most important sources of error. Given a deviation of the thickness Δd , a calculated refractive index n_s for a cuvette thickness d_s and n'_s for $d_s + \Delta d$, the error can be calculated from

$$\Delta n^d(\omega) = n'_s(\omega) - n_s(\omega), \quad (4.18)$$

obtaining:

$$\Delta n^d(\omega) = -(n_s(\omega) - 1) \frac{\Delta d}{d_s + \Delta d} \quad (4.19)$$

The error on the estimation of the refractive index propagates and affects also the absorption coefficient. The error from $\Delta\alpha(\omega) = \alpha(\omega, d_s + \Delta d) - \alpha(\omega, d_s)$ as:

$$\Delta\alpha^d(\omega) = -\alpha(\omega) \frac{\Delta d}{d_s + \Delta d} + \frac{2}{d_s + \Delta d} \ln \left(\frac{(n_s(\omega) + \Delta n(\omega))(n_s(\omega) + n_w)^2}{n_s(\omega)(n_s(\omega) + \Delta n(\omega) + n_w)^2} \right) \quad (4.20)$$

In those cases where $\Delta d \ll d_s$, which is generally true in this work, eqs. (4.19) and (4.20) can be approximated by:

$$\Delta n(\omega) = -(n_s(\omega) - 1) \frac{\Delta d}{d_s} \quad (4.21)$$

and

$$\Delta \alpha^d(\omega) = -\alpha(\omega) \frac{\Delta d}{d_s} + \frac{2}{d_s} \ln \left(\frac{(n_s(\omega) + \Delta n(\omega))(n_s(\omega) + n_w)^2}{n_s(\omega)(n_s(\omega) + \Delta n(\omega) + n_w)^2} \right) \quad (4.22)$$

Equation (4.22) can be further simplified when the second term is negligible. For typical values of the samples used in this work: $n_w = 1.525$, $n_s = 1.467$ and $\alpha = 0.52 \text{ cm}^{-1}$ at 1 THz (approximate values for the motor oil) and taking an approximated value of $14 \mu\text{m}$ for the standard deviation of the cuvette thickness as Δd in a cuvette with $d_s = 5 \text{ mm}$, eqs. (4.19) and (4.20) provide $\Delta n = 1.3 \times 10^{-3}$ and $\Delta \alpha = 1.5 \times 10^{-3} \text{ cm}^{-1}$. While the term $\alpha \Delta d / (d + \Delta d)$ increases linearly with α , the second term of eq. (4.20) ($-2/d_s \ln(R(\omega))$) contributes to the error with an almost constant value of approximately $7 \times 10^{-5} \text{ cm}^{-1}$. It is thus negligible for sufficiently thick samples or at sufficiently high frequencies. Under this assumption, $\Delta \alpha$ becomes:

$$\Delta \alpha^d(\omega) = -\alpha(\omega) \frac{\Delta d}{d_s} \quad (4.23)$$

Propagation of the standard deviation

Equations (4.19) and (4.20) provide the deviation that occur on the optical constants due to a deviation of the sample thickness. They do not provide, however, the standard deviation of n_s and α for a given standard deviation of the optical constants.

The uncertainty propagation, usually given by the variance (and, therefore, by the standard deviation) is a well known problem that, generally, does not have simple or exact solutions. While eqs. (4.19) and (4.20) give the equivalency, point by point, of any deviation of the sample thickness to the deviation of the optical constants, they do not directly provide the standard deviations of the optical constants (n_s and α), σ_n and σ_α , when substituting Δd by the standard deviation of the sample thickness, σ_d . An easy explanation is that the probability density function changes with transformations and the interval $[\mu_d - \sigma_d, \mu_d + \sigma_d]$ will not project into $[\mu_n - \sigma_n, \mu_n + \sigma_n]$ and $[\mu_\alpha - \sigma_\alpha, \mu_\alpha + \sigma_\alpha]$, where μ_d , μ_n and μ_α are the mean values of the sample thickness, d_s , n_s and α , respectively.

For any random variable X with normal probability density distribution with a mean μ_x and a standard deviation σ_x , the equivalency of the intervals described above is true for any linear transformation of the variable as $Y = aX + b$, which also has a normal distribution with a mean and a standard deviation that transform into

4. THz time-domain spectroscopy of liquids

$$\mu_y = a \cdot \mu_x + b \quad (4.24)$$

$$\sigma_y = |a| \cdot \sigma_x \quad (4.25)$$

In the function $y = ax + b$, any deviation on x propagates as $\Delta y = a\Delta x$. Substituting Δx by σ_x and taking the positive sign, the standard deviation propagation can be obtained from the propagated value of the error as:

$$\sigma_y = |\Delta y(\Delta x = \sigma_x)| \quad (4.26)$$

This is not true for other non-linear transformations or with more than one random variable. In most cases, if the standard deviation is sufficiently small, the error committed will be small and eqs. (4.19) and (4.20) will give a good approximation to the propagation of the cuvette thickness uncertainty to the optical constants. This is also true for any variable with symmetric probability density function X in which the confidence stays constant in the interval $[\mu_x - \sigma_x, \mu_x + \sigma_x]$ because any error will project into the equivalent interval, which will be still defined by the standard deviation. These criteria are fulfilled by normal probability distributions, but also, for instance, for uniform distributions. The confidence in the interval within one standard deviation in an uniform distribution between a and b , with a standard deviation $\sigma = (b - a)/\sqrt{12}$, is

$$\int_{\frac{b+a}{2}-\sigma}^{\frac{b+a}{2}+\sigma} \frac{1}{b-a} dx = \frac{2\sigma}{b-a} = \frac{2}{\sqrt{12}}, \quad (4.27)$$

and is thus eligible for this approximation.

In conclusion, for any transformation $Y = f(X)$ of a random variable X with symmetric probability density function in which the confidence within the interval $[\mu_x - \sigma_x, \mu_x + \sigma_x]$ is constant, the propagation of the standard deviation can be approximated from the error propagation for a value of σ_x sufficiently small by eq. (4.26).

This approximation is illustrated in fig. 4.4 showing the type of transformation that relates the refractive index n_s and the sample thickness d_s (eq. (4.10)).

Taking this assumptions, the propagation cuvette length uncertainty to n_s and α results in:

$$\sigma_{n,d}(\omega) \approx (n_s(\omega) - 1) \frac{\sigma_d}{d_s + \sigma_d} \quad (4.28)$$

and

$$\sigma_{\alpha,d}(\omega) \approx \alpha(\omega) \frac{\sigma_d}{d + \sigma_d} - \frac{2}{d_s + \sigma_d} \ln \left(\frac{(n_s(\omega) + n_w)^2 (n_s(\omega) - \sigma_{n,d}(\omega)) (1 + n_w)^2}{n_s(\omega) (1 + n_w)^2 (n_s(\omega) - \sigma_{n,d}(\omega) + n_w)^2} \right) \quad (4.29)$$

Another typical approach to the propagation of uncertainty is based on approximating any function with n variables $f(x_1, x_2, \dots, x_n)$ by a linear combination of the variables using a first-order Taylor expansion:

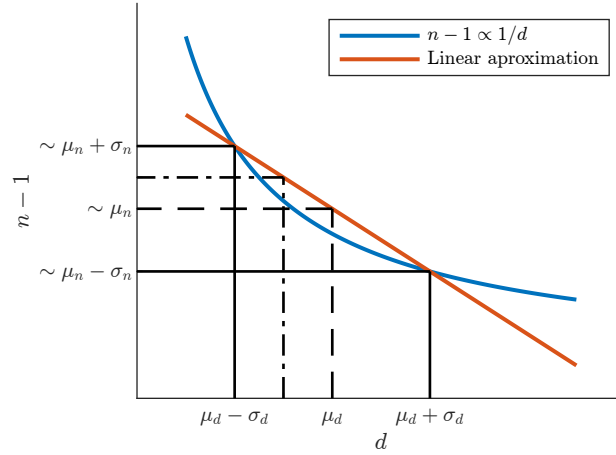


Figure 4.4.: Graphical representation of the linear transformation of a normal random variable and how it approximates any non-linear transformation if σ is sufficiently small.

$$f(x_1, \dots, x_n) \approx f_0 + \sum_{k=1}^n \frac{\partial f(x_1, \dots, x_n)}{\partial x_k} \quad (4.30)$$

If x_1, x_2, \dots, x_n are assumed to be independent random variables with variance $\sigma_1^2, \dots, \sigma_n^2$, the variance of f can be approximated from

$$\sigma_f^2 \approx \sum_{k=1}^n \left(\frac{\partial f}{\partial x_k} \right)^2 \sigma_k^2 \quad (4.31)$$

With this approximation, the uncertainty propagation, with the only random variable being d_s , results in:

$$\sigma_{n,d}(\omega) \approx \left| \frac{\partial n_s(\omega)}{\partial d_s} \right| \sigma_d = (n_s(\omega) - 1) \frac{\sigma_d}{d_s}, \quad (4.32)$$

and

$$\begin{aligned} \sigma_{\alpha,d}(\omega) &\approx \left| \frac{\partial \alpha(\omega)}{\partial d_s} \right| \sigma_d = \\ &= \alpha(\omega) \frac{\sigma_d}{d_s} - \frac{2}{d_s n_s(\omega)} \left(\frac{n_s(\omega) - n_w}{n_s(\omega) + n_w} \right) \sigma_n(\omega) = \\ &= \alpha(\omega) \frac{\sigma_d}{d_s} - 2 \left(\frac{n_s(\omega) - 1}{n_s(\omega)} \right) \left(\frac{n_s(\omega) - n_w}{n_s(\omega) + n_w} \right) \frac{\sigma_d}{d_s^2} \end{aligned} \quad (4.33)$$

It can be observed that eqs. (4.28) and (4.32) are almost identical. They actually are if $\sigma_d \ll d_s$, which is generally true. The same happens with the first term of σ_α in eqs. (4.29) and (4.33). Only the algebraic expressions of second term in both equations are significantly different.

4. THz time-domain spectroscopy of liquids

A third method can be found in the literature. Following the same approach than the authors in [64], where the uncertainty of the refractive index (σ_n) and the thickness (σ_d) are treated as independent, leads to a similar expressions of the uncertainty of the optical constants of a solid slab given in [64, 65]. While the expression (and the procedure) to obtain σ_n are identical to eq. (4.32), as it depends only on d_s , this is not the case for σ_α , where the two variables d_s and n_s are treated as independent, obtaining:

$$\begin{aligned}\sigma_{\alpha,d}^2(\omega) &\approx \left(\frac{\partial\alpha(\omega)}{\partial d_s}\right)^2 \sigma_d^2 + \left(\frac{\partial\alpha(\omega)}{\partial n_s(\omega)}\right)^2 \sigma_{n,d}^2(\omega) = \\ &= \left(\frac{\alpha(\omega)}{d_s}\right)^2 \sigma_d^2 + \left(\frac{2}{d_s n_s(\omega)}\right)^2 \left(\frac{n_s(\omega) - n_w}{n_s(\omega) + n_w}\right)^2 \sigma_{n,d}^2(\omega)\end{aligned}\quad (4.34)$$

This expression in eq. (4.34), although it is a sufficiently good approximation in most practical cases, underestimate the error as it does not consider the covariance between $n_s(\omega)$ and d_s , while the covariance in eqs. (4.29) and (4.33) is implicit.

To test the previous methods for uncertainty propagation, a Monte Carlo simulation was performed. Simulating a system with a thickness standard deviation of the cuvette σ_d , the refractive index and the absorption coefficient, with their respective standard deviations over 20000 realizations, are calculated. Figure 4.5a shows a Monte Carlo simulation of the random process next to the expressions in eqs. (4.28) and (4.32), where the only difference can be justified by a visual effect of the scale and the realizations of the random variables. Similarly, Figure 4.5b shows a Montecarlo simulation of the standard deviation of the absorption compared to the theoretical expressions from eqs. (4.29) and (4.32) to (4.34) (methods 1, 2 and 3, respectively). While eqs. (4.29) and (4.33) (methods 1 and 2) are indistinguishable and perfectly fit to the simulated data, eq. (4.34) (method 3) slightly underestimate it, something which is made more evident in the zoom shown in the inset from fig. 4.5b for the lowest frequencies. This is, as predicted, due to the absence of the correlation in that third method.

From this point forward, the propagation of uncertainty given by eqs. (4.28) and (4.29) (method 1) is used.

4.2.4. Error due to misplacement of the cuvette

Cuvette misplacement will have many effects on the measurements, affecting the beam propagation on a way that is difficult to track, as it will depend not only on the characteristics and positioning of the sample, but also on the Gaussian beam characteristics through the path.

Considering a planar propagation of the beam through the cuvette and a sufficiently large cross-section, so that the cuvette boundary effects are negligible, it is possible to estimate the error committed measuring the optical constants when the sample is positioned under an angle. As depicted in fig. 4.6 , inside a cuvette with

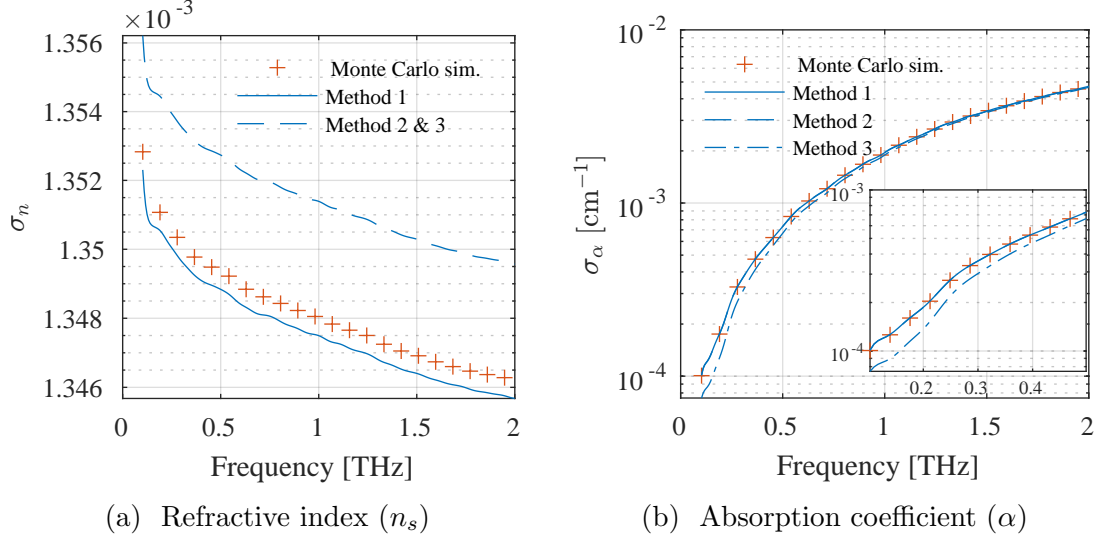


Figure 4.5.: Standard deviation of the optical constants calculated from the uncertainty propagation using three methods: method 1, provided by eqs. (4.28) and (4.29); method 2, provided by eqs. (4.32) and (4.33), and method 3, provided by eqs. (4.32) and (4.34). Methods 2 and 3 provide the same expression for the refractive index st. deviation. The used data correspond to the NA000 sample from round R0, as defined in section 5.6. The Monte Carlo simulation is performed with 20000 realizations of the optical constants using a normally distributed thickness with $\sigma_d = 15 \mu\text{m}$.

a thickness d_s , angled (or leaned) at an angle ξ , the beam will propagate over a distance, d'_s , given by:

$$d'_s = d_s / \cos \xi \quad (4.35)$$

Obtaining a thickness error of:

$$\Delta d^\xi = d'_s - d_s = d_s \left(\frac{1}{\cos \xi} - 1 \right) \quad (4.36)$$

Substituting (4.36) into (4.19) and (4.20), we obtain the propagated error as:

$$\Delta n^\xi(\omega) = -(n_s(\omega) - 1) \left(\frac{1}{\cos \xi} - 1 \right) \quad (4.37)$$

$$\begin{aligned} \Delta \alpha^\xi(\omega) = & -\alpha(\omega) \left(\frac{1}{\cos \xi} - 1 \right) \\ & + \frac{2}{d_s} \ln \left(\frac{(n_s(\omega) + \Delta n^\xi(\omega))(n_s(\omega) + n_w)^2}{n_s(\omega)(n_s(\omega) + \Delta n^\xi(\omega) + n_w)^2} \right) \end{aligned} \quad (4.38)$$

4. THz time-domain spectroscopy of liquids

The uncertainty in the refractive index due to the cuvette misplacement is independent of the cuvette length. The absorption coefficient features a term which is independent and another one that increases with $1/d_s$. The latter, however, will usually be negligibly small.

There is an additional consideration that must be made, as an angled cuvette with respect to the beam will also slightly displace the beam, causing improper propagation to the receiver. This will particularly affect to the amplitude, as usually the phase shift due to a small transversal misalignment of the receiver is negligible. In the case of liquid spectroscopy, the beam propagates through three different dielectric layers (the two windows and the sample or the air for the reference sample), each of the introducing displacement.

For a single dielectric slab (fig. 4.6a) with refractive index n_2 inside a medium n_1 the offset is given by:

$$d_{off} = \frac{d_s}{\cos \xi_2} \sin(\xi_1 - \xi_2), \quad (4.39)$$

where ξ_1 and ξ_2 are given by the Snellius' law

$$n_1 \sin \xi_1 = n_2 \sin \xi_2 \quad (4.40)$$

For small incident angles, the Snellius' law can be approximated by $n_1 \xi_1 = n_2 \xi_2$, $d_s / \cos \xi_2 \approx d$ and $\sin(\xi_1 - \xi_2) \approx \xi_1 - \xi_2$, simplifying eq. (4.39) into

$$d_{off} = d_s \xi_1 \left(1 - \frac{n_1}{n_2} \right) \quad (4.41)$$

Regarding a cuvette, consisting of three separated layers, the total offset originates at each individual layer as depicted in fig. 4.6b, where d_1 and d_3 corresponds to the offset introduced at the window layers, fulfilling $d_1 = d_3 = d_{off,w}$ if they are identical, and d_2 is the offset introduced by the liquid sample or the empty space between the windows for reference measurements.

Using simple trigonometry, and assuming the same approximations as in eq. (4.41), the offset of the whole cuvette can be calculated as the sum of three individual contributions

$$d_{off} = d_1 + d_2 + d_3 \quad (4.42)$$

The offset of the filled cuvette is thus:

$$d_{off}^{sam} = \xi_i \left[2 \cdot d_w \left(1 - \frac{1}{n_w} \right) + d_s \left(1 - \frac{1}{n_s} \right) \right], \quad (4.43)$$

while the offset for the empty cuvette, calculated from eq. (4.43) with $n_s = 1$ is

$$d_{off}^{ref} = 2 \cdot \xi_i d_w \left(1 - \frac{1}{n_w} \right) \quad (4.44)$$

d_s	d_w	n_s	n_w	ξ_i	$d_1(d_3)$	d_2	d_{off}^{sam}	d_{off}^{ref}
15 mm	3 mm	1.468	1.525	1°	0.02 mm	0.08 mm	0.12 mm	0.04 mm
15 mm	3 mm	1.468	1.525	5°	0.09 mm	0.42 mm	0.60 mm	0.18 mm
45 mm	3 mm	1.468	1.525	1°	0.02 mm	0.25 mm	0.29 mm	0.04 mm
45 mm	3 mm	1.468	1.525	5°	0.09 mm	1.25 mm	1.43 mm	0.18 mm

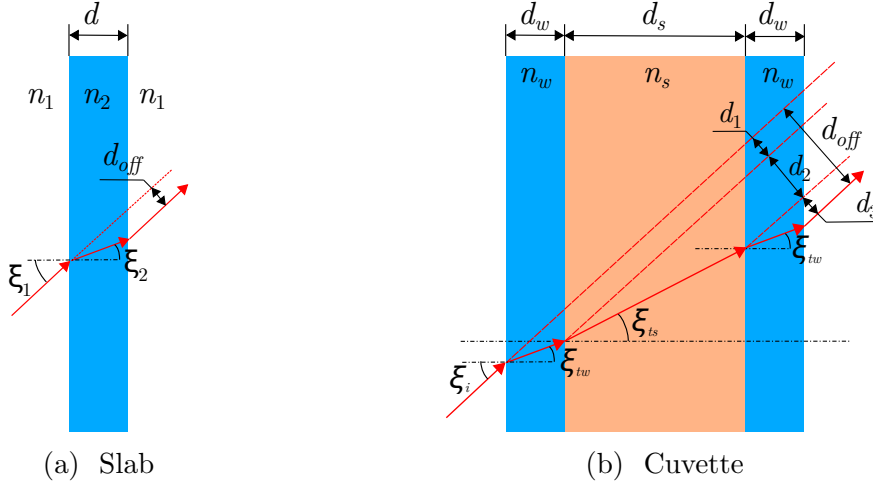
 Table 4.2.: Typical values for the beam offset given tilts of 1° and 5°


Figure 4.6.: Angled beam offset after crossing one or more dielectric slabs or layers

Table 4.2 shows the offset for typical beam offsets given angles of 1° and 5° degrees. When placing the samples manually, the error is typically below 5° (usually around 2°). For samples located at a highly collimated beam paths, with beam waists around 20 mm, the maximum offset do not exceed 7% of the beam waist for the largest cuvettes and misplacement angles. The effect of the offset will depend on the subsequent path and the propagation characteristics of the beam. As the receiver is mounted close to the focal point of a lens or mirror, the introduced error is usually (much) smaller than the relative error caused by the displacement. Further, only the difference of the displacements between the reference and the sample measurement matter.

4.2.5. Error introduced by the resolution of the TDS system

The temporal sampling resolution of the TDS system limits the resolution of the cuvette thickness measurement. The standard deviation of the observations from a measuring element with resolution δ_l , in which the probability distribution between two measurable values is uniform, is $\delta_l/\sqrt{12}$. Assuming again a unity refractive index of air and negligible imaginary refractive indices for $n_s(\omega)$ and n_w and substituting $\sigma_d = \delta_l/\sqrt{12}$ in eqs. (4.28) and (4.29), with $\delta_l \ll d_s$, the standard deviation of the optical constants given is:

4. THz time-domain spectroscopy of liquids

$$\sigma_{n,\delta}(\omega) = (n_s(\omega) - 1) \frac{\delta_l}{\sqrt{12}d_s} \quad (4.45)$$

and

$$\begin{aligned} \sigma_{\alpha,\delta}(\omega) = & \alpha(\omega) \frac{\delta_l}{\sqrt{12}d_s} \\ & - \frac{2}{d_s} \ln \left(\frac{(n_s(\omega) - \sigma_n(\omega))(n_s(\omega) + n_w)^2}{n_s(\omega)(n_s(\omega) - \sigma_n(\omega) + n_w)^2} \right) \end{aligned} \quad (4.46)$$

The uniform distribution applies for most dimension measurement devices, like rulers or calipers. Throughout this thesis the cuvette thickness has been measured using the first echo of the main pulse within the empty cuvette. This method can be modeled using two independent uniform variables: U_m and U_e , for the main pulse and the echo, respectively, representing the time at which each peak is recorded with variances $\sigma_{U_e}^2 = \sigma_{U_m}^2 = \delta_t^2/12$, where δ_t is the time resolution of the recorded time signal. The delay of the echo pulse is calculated as the difference between the two random variables, resulting in a new random variable with a variance:

$$\sigma_{U_e - U_m}^2 = \sigma_{U_e}^2 + \sigma_{U_m}^2 = \delta_t^2/6 \quad (4.47)$$

Thus, the corresponding spacial resolution can be calculated from:

$$\delta_l = \frac{c_0}{2} \delta_t, \quad (4.48)$$

where c_0 is the speed of light in vacuum and the 1/2 factor takes into account the fact that the echo is recorded after bouncing twice in the cuvette. The standard deviation of the measured cuvette thickness is then given by:

$$\sigma_d = \frac{c_0}{2\sqrt{6}} \delta_t \quad (4.49)$$

The standard deviation of the optical constants due to the resolution of the echo measurement in a system with a time resolution δ_t is, thus:

$$\sigma_{n,\delta}(\omega) = (n_s(\omega) - 1) \frac{c_0}{2\sqrt{6}} \frac{\delta_t}{d_s} \quad (4.50)$$

and

$$\begin{aligned} \sigma_{\alpha,\delta}(\omega) = & \alpha(\omega) \frac{c_0}{2\sqrt{6}} \frac{\delta_t}{d_s} \\ & - \frac{2}{d_s} \ln \left(\frac{(n_s(\omega) - \sigma_n(\omega))(n_s(\omega) + n_w)^2}{n_s(\omega)(n_s(\omega) - \sigma_n(\omega) + n_w)^2} \right) \end{aligned} \quad (4.51)$$

4.2.6. Amplitude variations in the THz signals

There are many different types of error that affect the amplitude of the recorded terahertz signals. Electrical and optical noises are primary sources of random error. However, other can behave as both random and systematic, such as the laser intensity fluctuation and the jitter of the mechanical delay line. Among the systematic errors, the mechanical drift (i.e. the changes on the setup alignment), must also be considered, specially when the different samples are introduced manually in the system.

Following a similar approach as in eqs. (4.19) and (4.20), this time from the deviation of the complex transmission quotient ($t(\omega) = |t(\omega)| \exp(-j\phi_t(\omega))$) in phase and amplitude ($\Delta\phi$ and Δt), where $\phi'_t(\omega) = \phi_t(\omega) + \Delta\phi(\omega)$ and $|t(\omega)'| = |t(\omega)| + \Delta t(\omega)$, obtaining:

$$\Delta n(\omega) = -\frac{C_0}{\omega d_s} \Delta\phi(\omega) \quad (4.52)$$

and

$$\Delta\alpha(\omega) = -\frac{2}{d_s} \ln \left(\frac{|t(\omega)| + \Delta t(\omega)}{|t(\omega)|} \frac{(n_s(\omega) + \Delta n(\omega) + n_w)^2 n_s(\omega)}{(n_s(\omega) + n_w)^2 (n_s(\omega) + \Delta n(\omega))} \right) \quad (4.53)$$

In order to express the error propagation to α , eq. (4.53) can be approximated by:

$$\Delta\alpha = \frac{2}{d_s} \frac{\Delta t(\omega)}{|t(\omega)|} - \frac{2}{d_s} \ln \left(\frac{(n_s(\omega) + \Delta n(\omega) + n_w)^2 n_s(\omega)}{(n_s(\omega) + n_w)^2 (n_s(\omega) + \Delta n(\omega))} \right) \quad (4.54)$$

Considering that the contribution of second term from equation eq. (4.54) is small, as was quantitatively shown already to obtain eq. (4.23), the standard deviation is further approximated by:

$$\sigma_\alpha(\omega) = \frac{2}{d_s} \frac{\sigma_t(\omega)}{|t(\omega)|}, \quad (4.55)$$

where the standard deviation of the field transmission amplitude, σ_t , is related to the standard deviation of the sample and reference signals in the frequency domain ($\sigma_{E,sam}, \sigma_{E,ref}$) as:

$$\sigma_t(\omega) = |t(\omega)| \cdot \sqrt{\frac{\sigma_{E,sam}(\omega)^2}{|E_{sam}(\omega)|^2} + \frac{\sigma_{E,ref}(\omega)^2}{|E_{ref}(\omega)|^2}} \quad (4.56)$$

Substituting eq. (4.56) in eq. (4.55):

$$\sigma_{\alpha,amp}(\omega) = \frac{2}{d_s} \sqrt{\frac{\sigma_{E,sam}(\omega)^2}{|E_{sam}(\omega)|^2} + \frac{\sigma_{E,ref}(\omega)^2}{|E_{ref}(\omega)|^2}} \quad (4.57)$$

4. THz time-domain spectroscopy of liquids

For the uncertainty propagation into the refractive index, $n_s(\omega)$, which depends on the real and imaginary part of the sample and reference signals, the standard deviation of the temporal signals must be considered. This is also a more practical approach, as usually the dynamic range is improved by averaging multiple signals in the time domain.

This approach is used in [65], where the variances of the optical constants of a solid slab sample are calculated, given the time domain standard deviations $\sigma_{E,sam}(t)$ and $\sigma_{E,ref}(t)$. Following a similar approach, they can also be calculated for the spectroscopy of liquids as:

$$\sigma_{n,amp}(\omega) = \frac{C_0}{\omega d_s} \sqrt{\frac{Q_{sam}(\omega)}{|E_{sam}(\omega)|^4} + \frac{Q_{ref}(\omega)}{|E_{ref}(\omega)|^4}} \quad (4.58a)$$

$$\sigma_{\alpha,amp}(\omega) = \frac{2}{d_s} \sqrt{\frac{R_{sam}(\omega)}{|E_{sam}(\omega)|^4} + \frac{R_{ref}(\omega)}{|E_{ref}(\omega)|^4} + \left(\frac{n_s(\omega) - n_w}{n_s(\omega) + n_w}\right)^2 \frac{\sigma_n^2(\omega)}{n_s^2(\omega)}}, \quad (4.58b)$$

where

$$\begin{aligned} Q_{sam}(\omega) &= \sum_k (\Im [E_{sam}(\omega) \exp(j\omega k\tau)])^2 \sigma_{E,sam}^2(\omega), \\ Q_{ref}(\omega) &= \sum_k (\Im [E_{ref}(\omega) \exp(j\omega k\tau)])^2 \sigma_{E,ref}^2(\omega), \\ R_{sam}(\omega) &= \sum_k (\Re [E_{sam}(\omega) \exp(j\omega k\tau)])^2 \sigma_{E,sam}^2(\omega), \\ R_{ref}(\omega) &= \sum_k (\Re [E_{ref}(\omega) \exp(j\omega k\tau)])^2 \sigma_{E,ref}^2(\omega) \end{aligned} \quad (4.59)$$

with k denoting the temporal index and τ the sampling period ($k\tau$ denotes thus the time). The complete derivation of eqs. (4.58a) and (4.58b) (the versions for a solid slab sample) can be found in the appendix of the work from Withayachumnankul *et al.* in [65].

4.2.7. Optimal cuvette length

The error of the absorption coefficient is related in two ways to the sample thickness, d_s . The first one is the uncertainty of the cuvette length, given by eq. (4.29) and which was used to model resolution and positioning errors (eqs. (4.38) and (4.51)). Here, Equation (4.29) is approximated by $\sigma_{\alpha,d} = \alpha\sigma_d/d_s$. The second one is the error introduced by noise, which also depends on the cuvette length. If the signal-to-noise ratio (SNR) between the reference and the sample spectra is only affected by the absorption of the sample, eq. (4.57) can be rewritten as:

$$\sigma_{\alpha,amp}(\omega) = \frac{1}{d_s} \sqrt{\frac{\exp[\alpha(\omega)d_s] + 1}{SNR_{ref}(\omega)}}, \quad (4.60)$$

where SNR_{ref} is the signal to noise ratio of the reference spectra (i.e. $SNR_{ref}(\omega) = |E_{ref}^2(\omega)| / \sigma_{E,ref}^2(\omega)$).

Assuming that these two sources of error are the main contributors to the random error of the absorption coefficient and independent, the standard deviation of the cuvette is then

$$\sigma_{\alpha}(\omega) = \sqrt{\sigma_{\alpha,d}^2(\omega) + \sigma_{\alpha,amp}^2(\omega)} \quad (4.61)$$

The optimum thickness can be then calculated from eq. (4.61) as:

$$d_{opt} = \arg \min_{d_s} \left[\sqrt{\left(\alpha(\omega) \frac{\sigma_d}{d_s} \right)^2 + \left(\frac{1}{d_s} \right)^2 \frac{\exp[\alpha(\omega)d_s] + 1}{SNR_{ref}(\omega)}} \right] \quad (4.62)$$

Figure 4.7 shows the optimal thickness calculated for several absorption coefficient and cuvette thickness uncertainty (σ_d) at different values of the SNR concerning the precision of the absorption coefficient. The optimal length is first constant when the error is dominated by noise at low SNR. The SNR at which the effect of the thickness uncertainty is visible reduces as the absorption increases (40 dB for a sample with $\alpha = 20 \text{ cm}^{-1}$ and 70 dB with 0.5 cm^{-1}). Above these values, the cuvette length uncertainty starts to be relevant and changes the optimal cuvette length for different standard deviations of the sample thickness.

There is not a unique optimal value due to the strong dependency with the absorption coefficient. In chapter 5, the frequency dependence of the optimal cuvette length, using data from measured samples, is shown.

4.2.8. Phase unwrapping artifacts and correction

In transmission spectroscopy, the determination of the refractive index from the phase of the field transmission, $\phi(\omega)$, of $t(\omega)$ (eq. (4.2)), requires the unwrapping of the discontinuous value of the phase, which is usually expressed with values between $-\pi$ and π , jumping back to $-\pi$ by -2π jumps every time the $\pm\pi$ value is exceeded.

The unwrapped value of the phase which is used in order to calculate the refractive index is:

$$\phi(\omega) = \angle t(\omega) - 2\pi N(\omega), \quad (4.63)$$

where N is an integer number that accounts for the number of discontinuities in the wrapped phase ($\angle t(\omega)$).

A problem arises when a 2π shifts occur within the first few frequency points of the recorded spectrum, as they are usually noisy below 100 GHz. These shifts must be identified and corrected in order to avoid the incorrect unwrapping of the phase, which ultimately leads to an unreliable value of the refractive index along the whole frequency range. This unreliable refractive indices can usually be identified as largely decaying curves towards the lower edge of the spectrum, while they will converge to a constant value at the higher end. This phenomenon can be observed

4. THz time-domain spectroscopy of liquids

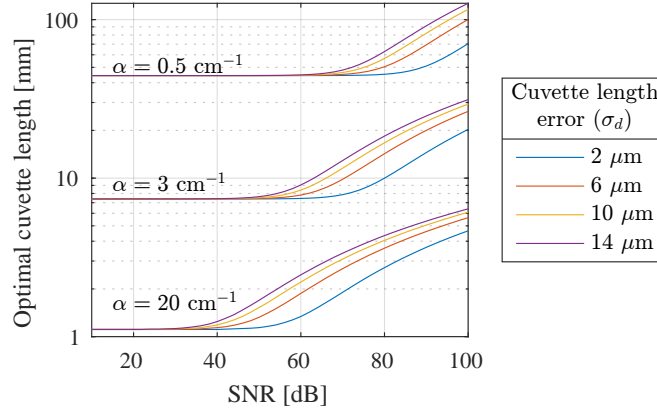


Figure 4.7.: Optimal length calculated at different SNR values of the reference measurement for different absorption coefficient and cuvette length standard deviations. The values have been chosen from samples that will be seen in the next chapters: $\alpha = 3 \text{ cm}^{-1}$ is the maximum absorption coefficient from the samples in chapter 5 and $\alpha = 20 \text{ cm}^{-1}$ from chapter 6. $\sigma_d = 2 \mu\text{m}$ is the approximated standard deviation caused by the resolution and $\sigma_d = 14 \mu\text{m}$ is the error produced by the assembly process of the cuvette, both demonstrated in chapter 5.

in fig. 4.8, where the phase and the refractive index from two different *hann* window lengths is plotted. The one with a length of 30 ps provides a correct phase reading, while the 25 ps window exhibits a -2π jump and, therefore, a glitch on the refractive index.

In order to avoid this, other authors have proposed a linear extrapolation from the first reliable phase value, so that the curve crosses the origin [66]. This is a good solution in those scenarios where a linear phase (i.e. constant refractive index) can be assumed [67].

After observing that certain window lengths produce phase shifts beyond $\pm\pi$ that make this artifact to occur, the possibility to use the window length as a correcting element for this artifact and compare the results with the usual extrapolation methods is analyzed.

Figure 4.8 shows that, using extrapolation, it is possible to correct the artifact arising from the 2π shifts, providing a much more accurate result. The window lengths of 25 and 30 ps were chosen, as they provided results with and without the phase artifact, as shown in fig. 4.9. The data corresponds to the GA040 sample (mixture of 4 % fuel in engine oil) that will be described in chapter 5 and a 45 mm cuvette. The anomalous results are difficult to predict and are different for different samples and data, but the *hann* window lengths that produce them are always grouped, as shown in fig. 4.9. This might indicate that the phase jump happens when certain features are included or excluded by the windowing of the time domain signal, but without a clear pattern or reproducibility between different samples.

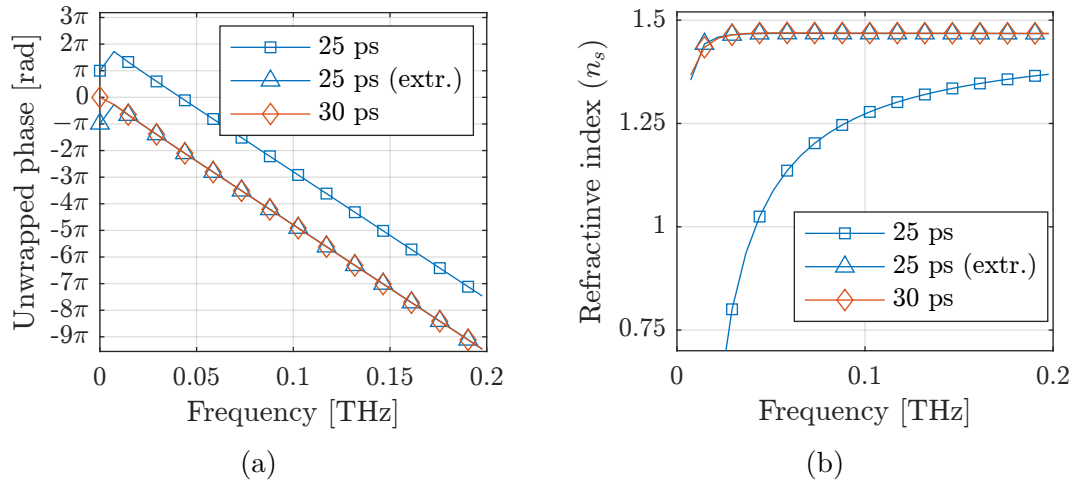


Figure 4.8.: Effects of the phase unwrapping glitch on the phase and the calculated refractive index.

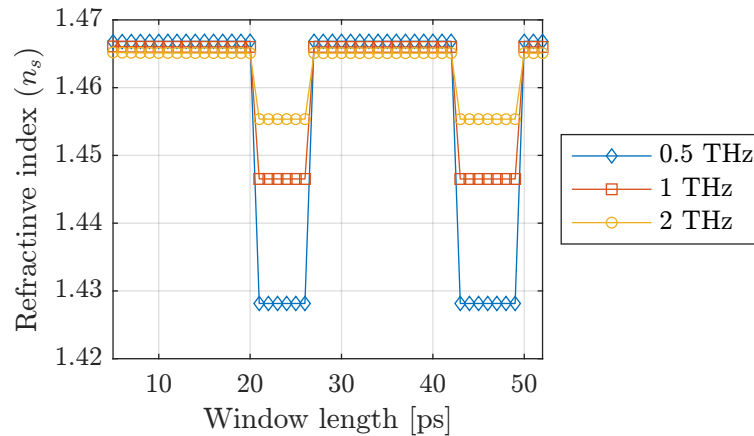


Figure 4.9.: Refractive indices of sample GA040 for different window lengths at 0.5, 1 and 2 THz. The lengths that provide drastically lower values are those at which a 2π shift occurs within the first points of the field transmission spectrum ($t(\omega)$).

Phase extrapolation vs. window length selection

Figure 4.10 shows the refractive index obtained after extrapolating the phase resulting from processing the time signal with different *hann* window lengths. It varies more than the one provided by simply choosing appropriate window lengths that do not produce phase jumps. This means that, if possible, visually inspecting the results and changing the length of the *hann* window accordingly could be more propitious than setting a fixed *hann* window length for all samples and applying extrapolation.

In the present work, the phase jump has been corrected by manually inspecting the refractive index. After selecting an initial window length, considering the duration of the main pulse and the time at which the first echoes will appear, so that the former is not filtered and the latter is kept outside the window, the resulting refractive indices are checked for their reliability, changing the window size for those samples that show anomalies. Figure 4.10 shows that, for windows shorter than 10 ps, the refractive index changes drastically in an unphysical manner. This is the result of a too short window that has a significant impact on the main pulse shape, as it becomes a softening filter for the spectra, losing information and resolution. In the upper limit, no distortion is observed, although the longer the window, the more likely it is to include other artifacts or reflections from the recorded time signal.

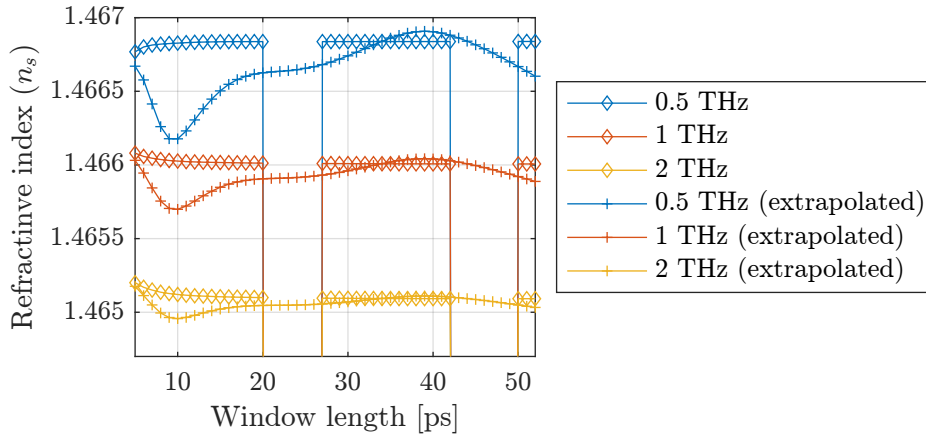


Figure 4.10.: Refractive indices of a mixture of 4 % fuel in engine oil (sample GA040) for different window lengths at 0.5, 1 and 2 THz and the corrected values using the extrapolation method.

The standard deviation of the refractive index obtained with different *hann* window lengths is shown in Figure 4.11. Only excluding the windows in which the glitch occurs, the error is negligible ($\sim 1 \times 10^{-6}$) and white, meaning that the influence of the *hann* window length is negligible. Using extrapolation, however, introduces a colored error that, though small, varies between 1×10^{-4} and 2×10^{-5} . The best

way to correct the phase artifacts is, therefore, changing the window length to a value that does not produce it.

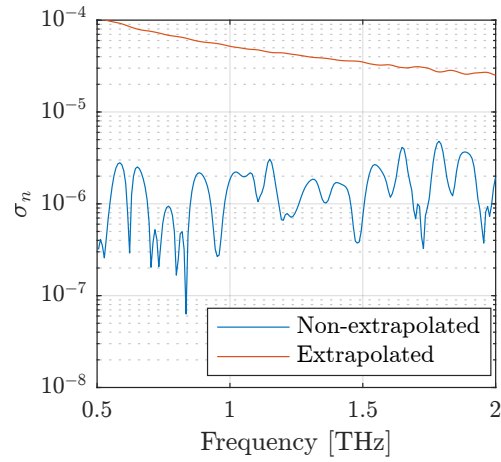


Figure 4.11.: Standard deviation of the refractive index (n_s) obtained with *hann* window lengths between 18 and 52 ps, in intervals of 1 ps. For the non-extrapolated data, the values in which the phase glitch provides a wrong value were excluded.

5. Distinctness of engine oil contamination with fuel and oxidation grade using THz-TDS

5.1. Introduction

Leaking unburned fuel that mixes with the oil is a potential risk for engines, reducing the lubricant and heat conducting properties of the oils. A 5% fuel contamination has been found to be a potentially dangerous limit [68]. With many systems only relying on the engine mileage as an oil change indicator, the most studied sensors are based on viscosity changes [69–71], with only some using infrared technologies [72].

Another risk for the engine is oil degradation due to aging, which usually reflects in oxidation. Introducing sensors that can identify these oxidation levels helps to reduce costs by avoiding the risk of costly machinery damage, but also reducing unnecessary maintenance of intact oil.

Terahertz (THz) time-domain spectroscopy (THz-TDS) is a potential technology that might allow for a good discrimination among contaminants in engine oils, fostered by publications that already showed the good discrimination among different gasoline contents [73,74]. It has already been applied to lubricant oils [75,76], oil base stock and additives [77], or water contamination in diesel engine oil [59]. In particular, 1550 nm THz-TDS systems offer a cost effective approach, with well-known and developed components at telecom wavelength with compact semiconductor front-ends which might enable real time, in-situ characterization.

This chapter uses the data from references [74,78] and extends the error analysis, to better identify the main error sources. The objective is thus to present the data for discriminating the different fuel content and oxidation levels, obtaining the error bars and extending the error analysis under different circumstances. It structures as follows: in a first section, the samples and the setup are described, followed by an experimental analysis of the cuvette thickness uncertainty. Next, the error of the optical constants using a single cuvette is estimated and the samples distinctness and the optimal cuvette length are analyzed. In the next two sections, the error arising from the use of multiple cuvettes (simulating a less controlled environment) and the estimation of the remaining systematic and random error sources are studied and compared.

5.2. Samples and measurement techniques

5.2.1. Samples under test

Two different experiments were carried out using two sets of samples and a reference sample:

- The reference sample is a commercially available gasoline engine oil (SAE 5W20, API SN service category), obtained from a local distributor in Carbonale, Illinois, USA.
- The first experiment was conducted to characterize the different levels of oxidation of the reference oil. The oxidation is accomplished using an available reactor from Parr Instruments Company which circulates ambient air through the oil under a controlled temperature, adjusted at $180\text{ }^{\circ}\text{C} \pm 1\text{ }^{\circ}\text{C}$ and with a regulated air flow of 1.0 l/min [78]. Three samples of 50 ml were processed during 48 h, 96 h and 144 h. After each oxidation and the subsequent cooling, the samples were bottled in an amber glass and sealed before being sent to Darmstadt for characterization using the THz-TDS setup.
- The second set of samples consists of 50 ml mixtures of engine oil and 87 octane gasoline. Three different samples were prepared with a gasoline content of 2 ml, 4 ml and 6 ml, corresponding to 4%, 8% and 12%. They were sent to Darmstadt within sealed amber glass bottles.

A summary of the samples and the given aliases can be found in table 5.1

Sample	Description
NA000	Reference motor oil (SAE 5W20)
OX048	Oxidized oil for 48 h at 180 °C
OX096	Oxidized oil for 86 h at 180 °C
OX144	Oxidized oil for 144 h at 180 °C
GA040	Gasoline contaminated oil (4% gasoline content)
GA080	Gasoline contaminated oil (8% gasoline content)
GA120	Gasoline contaminated oil (12% gasoline content)

Table 5.1.

Summary of samples with the alias given throughout the present work.

5.2.2. Data set: division in measurement rounds

The data set consists of six measurement rounds (R0 to R5) of all the seven samples (except R5). Each round is the consecutive measurement of the seven samples (four in the case of R5), assembling and disassembling the cuvette in order to clean it. Each sample requires two measurements, a first reference signal is recorded with a

newly assembled cuvette and a second measurement after filling the cuvette with the sample. Only in R4 and R5, the filled cuvette was measured multiple times after the reference measurement before disassembling it for cleaning in preparation for the next sample. The sample was removed from the setup and placed again at the same position between measurements so that the misplacement error could be analyzed.

- **R0**: reference data set, with the optical constants n_s and α calculated for each sample (NA000, OX048, OX096, OX144, GA040, GA080 and GA120) using calibrated cuvettes with the 5 mm spacer, where the sample thickness is precisely obtained from the echoes of each of the seven reference signals (seven different cuvette mounts, but each of them with the echo due to the internal reflection on the empty cuvette available, so that the exact thickness is known with an error below 3 μm (see section 5.3).
- **R0'**: Using the same data as in R0, but calculating the optical constants of all seven samples using the average thickness value of the 5 mm cuvette (5.19 mm). This round is intended to give an estimation of the error of the optical constants caused by sample thickness changes, eliminating other systematic and random errors, as it shares the raw data with the reference values from R0, changing only the thickness values which are used to compute n_s and α during post-processing.
- **R1** and **R2**: Rounds using the nominal 10 mm cuvettes. In both rounds, all seven samples were measured using different cuvette assemblies with the same spacers, but the optical constants are calculated for a fixed sample thickness of 10.16 mm, obtained in section 5.3 as the average thickness of cuvettes using the (nominal) 10 mm spacer.
- **R3** and **R4**: Rounds that use nominal 15 mm cuvettes (15.34 mm), similar to R1 and R2. The R4 round is composed of three measurements with the same 15 mm spacer for each sample and the data is recorded averaging over only 1200 waveforms, as compared to the 3000 waveforms in all other rounds (R0 to R3).
- **R5**: similar to R4 but using a 45 mm spacer and measuring only the NA and OX samples. This round was recorded some months after the previous ones with freshly prepared samples.

5.2.3. Measurement setup

The THz-TDS spectrometer consists of a commercial system from MenloSystems GmbH that uses a 1550 nm pulsed laser with a pulse length shorter than 90 fs and a pair of fiber coupled photoconductive antennas (PC) as source and detector.

5. Distinctness of engine oil with THz-TDS

Round	Nominal spacer	Repetitions (N_R)	Echo recording
R0	5 mm	1	yes
R1	10 mm	1	no
R2	10 mm	1	no
R3	15 mm	1	no
R4	15 mm	2/3/4*	no
R5	45 mm	3	no

Table 5.2.: Overview of the recorded measurement rounds. The number of repetitions consists of the number of times the sample was measured with the same cuvette mount after the reference measurement. The echo recording indicates whether the echo corresponding to the pulse bound between the two windows has been recorded in the reference pulse, so that a more exact thickness of the cuvette can be provided eliminating the error arising from the different thickness of the individual cuvette mounts used for each sample. *In R4, the GA samples were recorded 4 times each and GA040 was measured in three independent cuvettes with 2, 3 and 4 repetitions. All other samples (NA and OX) were repeated 3 times each.

The entire THz path is encapsulated and purged with dry nitrogen in order to eliminate water vapor traces from the measurement. In principle, the system allows for real time data acquisition of around 6 samples/s (depending on the time span recorded), but averaging in the time domain increases the bandwidth by reducing the noise floor, dominated by shot noise of the detector. Time signals were averaged over either 200 s (1200 waveforms) or 500 s (3000 waveforms). The dynamic range reduces quickly above 2-3 THz. With 500 s averages, the dynamic range of the empty cuvette spectrum was 90 dB at the peak frequency of 0.27 THz and 86 dB with 200 s. Filling the cuvette with the most lossy sample of the seven treated in this chapter (GA120), the noise floor is reached at around 3 THz. With less lossy samples and thinner spacers, the bandwidth extends to around 4 THz. In order to keep at least 30 dB of signal to noise ratio (SNR), the analysis is performed in the range between 0.2 and 2 THz.

The setup is configured in transmission configuration, with the cuvette placed in the collimated part of the beam, as close as possible to the detector. The cuvette consisted of 3 mm thick polyethylene (PE) windows separated by a metal spacer. Four different spacers were used with nominal lengths of 5, 10, 15 and 45 mm. An additional 2 mm spacer was also used, together with the others, to estimate the cuvette thickness error in different experiments. The metal spacer had grooves to fit the cylindrical gaskets that sealed the cuvette junctions. An outer metal frame kept the windows and spacers firmly locked, ensuring the straightness of the windows and a well defined and reproduceable size of the probe volume. A photograph of the setup with the cuvette, following the scheme from fig. 4.1 can be seen in fig. 5.2.

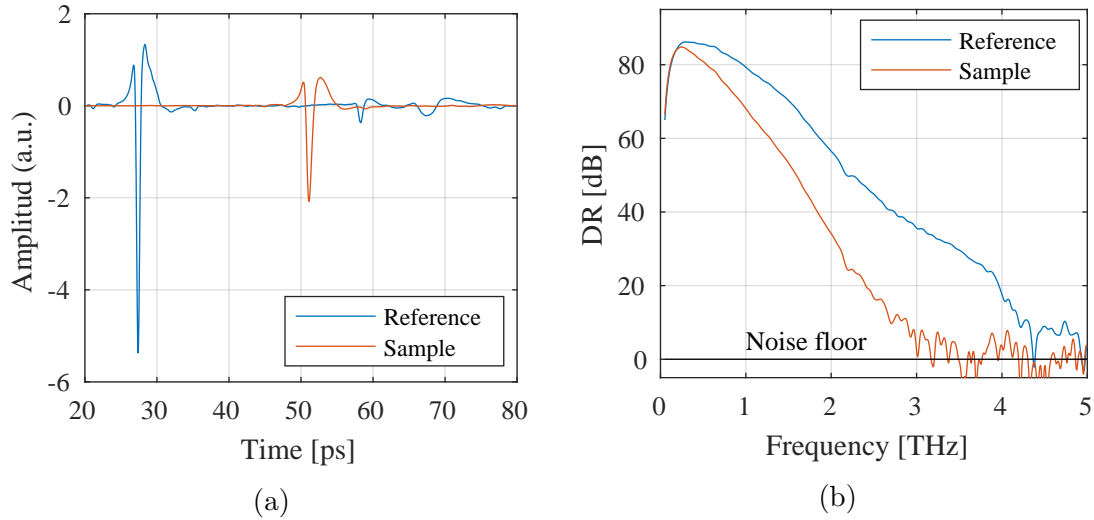


Figure 5.1.: Time and frequency domain recorded signals of the GA120 sample from round R4 (15 mm cuvette and integration time of 200 s).

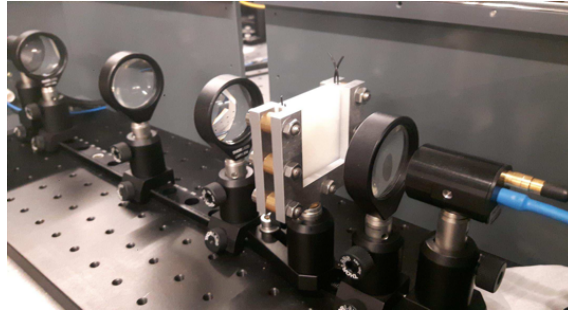


Figure 5.2.: Photo of the 2 mm cuvette in the THz-TDS setup.

5.3. Cuvette thickness error estimation

Several cuvette assemblies have been mounted and measured with sufficiently long-time spans in different iterations in order to check the echoes and precisely measure the thickness and the error between iterations. A total of 21 independent cuvette assemblies were measured and are summarized in table 5.3.

5.3.1. Estimation of the error for individual cuvettes

In order to estimate the error due to the resolution and the sample positioning occurring with a single cuvette, several consecutive thickness measurements were carried out for the cuvettes C1 - C8, corresponding to nominal spacer thicknesses of 10 and 15 mm. The cuvettes were taken out of the setup after every measurement, but without disassembling or altering anything else in the setup, minimizing the systematic errors. In this procedure, the error due to the resolution of the measuring

5. Distinctness of engine oil with THz-TDS

Cuvette number	Spacer	N_R	d_s
C1	10 mm	3	10.1600 mm
C2	10 mm	3	10.1700 mm
C3	10 mm	3	10.1567 mm
C4	15 mm	3	15.3400 mm
C5	15 mm	3	15.3350 mm
C6	15 mm	3	15.3333 mm
C7	2 mm	7	2.3707 mm
C8	2 mm	3	2.3817 mm
C9 - C15	5 mm	1	5.1857 mm (av.)
C16 - C21	45 mm	1	45.2800 mm (av.)

Table 5.3.: Summary of the 21 independent cuvette assemblies (C1 to C21) performed in order to characterize the uncertainty of the sample thickness. C1 to C8 correspond to different independent assemblies, each of them repeated N_R times by removing it from the beam path and replacing it, so that the error due to tilting of the cuvette by manual placing can be recorded. The cuvettes C9 to C21 are independent cuvette assemblies using the 15 and 45 mm labeled spacers.

method and the sample positioning (angle of the sample with respect to the beam) are, in practice, indistinguishable. There is however, a distinctive difference between the two. While the resolution error is independent of the size of the cuvette, the thickness error of the cuvette increases with the thickness, as shown by equation (4.36).

Thus, the standard deviation of the sample thickness for a single cuvettes must be calculated separately for different nominal spacers, but different cuvettes with the same nominal value are used in order to estimate the standard deviation by increasing the total number of observations. The standard deviation estimator is given by

$$\hat{\sigma}_d = \sqrt{\frac{\sum_{m=1}^{N_C} \sum_{n=1}^{N_m} (x_{m,n} - \bar{x}_m)^2}{N_T - N_C}}, \quad (5.1)$$

where the index value m represents the number of the cuvette, with N_C the total number of cuvettes for a nominal thickness (e.g. $N_C = 3$ for the 10 mm cuvette and $N_C = 2$ for 2 mm). The index n corresponds to each of the measurements taken in each assembly, with the number of these denoted as N_m and shown in table 5.3 as N_R for each assembly. The $N_T - N_C$ term, where N_T is the total number of measurements ($N_T = \sum_{m=1}^{N_C} N_m$), aims to correct the estimation of the standard deviation from the small set of samples ($N_T = 9$ for 10 mm and 15 mm and $N_T = 10$ for 2 mm), given that the N_C different mean values (one for each cuvette) are statistically dependent. The results are depicted in table 5.4. The data

shows that the error does not increase with the thickness, proving that the error is dominated by the measurement resolution.

All measurements are recorded using the same time resolution of 0.033356 ps, corresponding to a spatial resolution of $5 \mu\text{m}$. The standard deviation, assuming the model from eq. (4.47), is then $\sigma_l = 5/\sqrt{6} \mu\text{m} \approx 2.04 \mu\text{m}$.

Nominal thickness	Averaged thickness	$\hat{\sigma}_{d,single}$
10 mm	10.1622 mm	$1.6667 \mu\text{m}$
15 mm	15.3361 mm	$1.6667 \mu\text{m}$
2 mm	2.3740 mm	$4.1547 \mu\text{m}$

Table 5.4.: Standard deviation of the thickness measurement.

The larger standard deviation of the 2 mm cuvette is probably caused by the small number of samples. It can be assumed that the error is introduced by the resolution limit and is independent of the cuvette length. Therefore, the standard deviation from cuvette C1 to C8 can be pooled as $\hat{\sigma}_{(single)}^2 = [\sigma_{10}^2(9-3) + \sigma_{15}^2(9-3) + \sigma_2^2(10-2)]/[(9-3) + (9-3) + (10-2)]$ obtaining $\hat{\sigma}_{(single)} = 2.93 \mu\text{m}$, above but close to the $2 \mu\text{m}$ theoretical value when the error is established by the resolution limit.

5.3.2. Estimation of the sample thickness error between different assemblies

The second case of study is the error introduced by successive mountings and demountings of the cuvettes. For this purpose, all previous cuvette measurements are used, taken the median thickness among the N_m measurements for cuvette m . Two more sets of data are included, corresponding to cuvettes C9 to C15 from table 5.3, with a spacer with a nominal thickness of 5 mm, and C16 to C21, with a nominal thickness of 45 mm.

The procedure to mount and demount the cuvettes is similar throughout all measurements. There are, however, many factors that might affect the thickness of the cuvette at the micrometer or even tens of micrometer level: the tightening torque of the frame to the windows and the spacer, the stretching of the o-rings or the deformation of the PE windows, which have been observed to become slightly curved after several uses. There should be, however, no intrinsic differences in the error sources between different mounts. Therefore, it is possible to provide an estimation of the standard deviation of the cuvette thickness with a larger number of observations using a similar approach as in the previous section.

The uncertainty of the cuvette length using the 5 and 45 mm spacers, with seven samples each, is characterized using the standard deviation, obtaining a result of $11.70 \mu\text{m}$ for the 5 mm cuvette and $30.98 \mu\text{m}$ for the 45 mm one. The big difference between the two can be partially explained by individual observations of wrongly

5. Distinctness of engine oil with THz-TDS

mounted cuvettes. Eliminating an anomalous 45 mm cuvette mount, which can be seen in fig. 5.3, the standard deviation of the 45 mm cuvettes drops to 17.10 μm .

These results can be combined using the same approach as in eq. (5.1) or, equivalently, pooling the variances as:

$$\hat{\sigma}_{(5,45)}^2 = \frac{\sigma_{(5)}^2(N_5 - 1) + \sigma_{(45)}^2(N_{45} - 1)}{(N_5 - 1) + (N_{45} - 1)}, \quad (5.2)$$

where $\sigma_{(5)}$ and $\sigma_{(45)}$ is the standard deviation of the 5 mm cuvette spacer and N_5 and N_{45} the number of samples taken for each. The pooled standard deviation is then 14.11 μm .

The cuvettes used in the analysis of single error cuvettes (C1-C8), corresponding to 3 samples of 10 and 15 mm spacers and 2 of 2 mm, can also be added using the averaged value through all the repetitions, using a similar pooling as in eq. (5.2),

$$\hat{\sigma}_{(all)} = \sqrt{\frac{\sum_m \sigma_{(m)}^2(N_m - 1)}{\sum_m (N_m - 1)}}, \quad (5.3)$$

obtaining an estimated standard deviation of the cuvette thickness 12.06 μm . The big difference between the uncertainty on the cuvette thickness for a single assembly and multiple assemblies, around four times larger, makes the latter to introduce larger error bars on the optical constant measurements. Therefore, a previous measurement of the thickness of each assembly is required for precise measurements. In the following sections, it will be demonstrated that the assembly error predominates when the exact thickness is not measured.

Spacer	Cuvettes	\bar{x}_k	N_k	$\sigma_{d,k}$
2 mm	C7-C8	2.375 mm	2	7.07 μm
10 mm	C1-C3	10.162 mm	3	7.64 μm
15 mm	C4-C6	15.337 mm	3	3.47 μm
5 mm	C9-C15	5.186 mm	7	11.70 μm
45 mm	C16 - C21	45.280 mm	5	30.98 μm
45 mm	C16-C19, C21	45.269 mm	4	17.10 μm
45, 5	C9 - C19, C21	-	10	14.11 μm
All	C1-C19,C21	-	19	12.06 μm

Table 5.5.: Summary of the cuvette thickness uncertainty from different cuvette sets.

5.4. Uncertainty of the optical constants with a single-cuvette configuration

The first error analysis is performed using subsequent measurements of a given sample using a single cuvette. This error corresponds to a setup with precisely

5.4. Uncertainty of the optical constants with a single-cuvette configuration

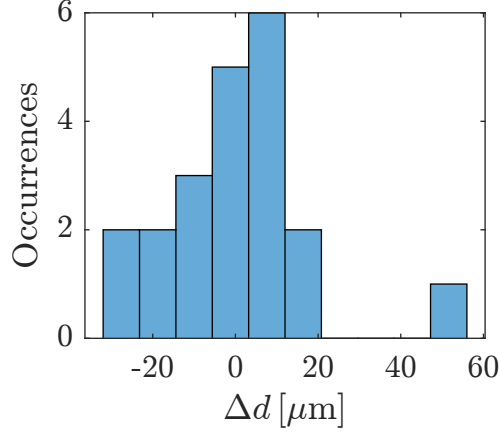


Figure 5.3.: Histogram with the deviation of the cuvette thicknesses from their average value. The single value above 4×10^{-5} m corresponds to C20, which has been excluded to obtain the final standard deviation of $12.06 \mu\text{m}$.

known cuvette lengths, or in which a single cuvette is used, however, displacements or rotations between successive measurements are allowed. The rest of the system is supposed to be in a steady state and does not change substantially during the repeated measurements.

For this purpose, the optical constants were measured multiple times in rounds R4 and R5 following the reference measurement for each sample, without emptying or cleaning the cuvette (which was done in between different samples). The standard deviation for each individual sample is estimated as:

$$\hat{\sigma}_{n, \text{single}}^{(s)}(\omega) = \sqrt{\frac{\sum_{r=0}^{N_R-1} \left(n_r^{(s)}(\omega) - \overline{n^{(s)}}(\omega) \right)^2}{N_R - 1}} \quad (5.4)$$

$$\hat{\sigma}_{\alpha, \text{single}}^{(s)}(\omega) = \sqrt{\frac{\sum_{r=0}^{N_R-1} \left(\alpha_r^{(s)}(\omega) - \overline{\alpha^{(s)}}(\omega) \right)^2}{N_R - 1}} \quad (5.5)$$

where s denotes the sample (NA000, OX048, ...), N_R is the number of measurement iterations (see table 5.2) and $\overline{n^{(s)}}(\omega)$ and $\overline{\alpha^{(s)}}(\omega)$ are the average values of the optical constants among the N_R repetitions (i.e. $\overline{n^{(s)}}(\omega) = (1/N_R) \sum_{r=0}^{N_R-1} n_r^{(s)}(\omega)$ and $\overline{\alpha^{(s)}}(\omega) = (1/N_R) \sum_{r=0}^{N_R-1} \alpha_r^{(s)}(\omega)$, respectively).

Despite the small number of measurements for each sample (a maximum of 4), the results of the estimated standard deviation are plotted together in figs. 5.4a and 5.4b. The error behaves differently for each optical constant and, therefore, it is analyzed individually.

5. Distinctness of engine oil with THz-TDS

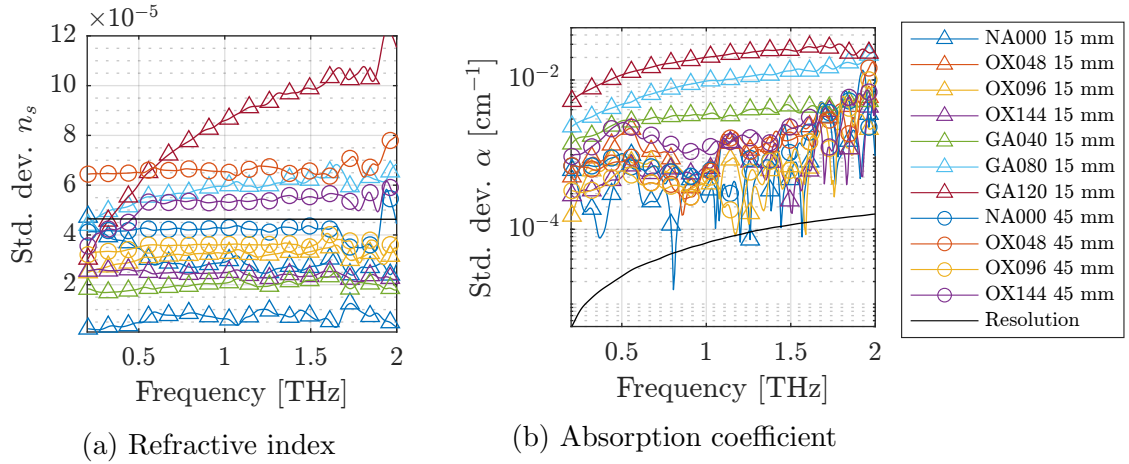


Figure 5.4.: Estimated standard deviation for the refractive index (a) and the absorption coefficient (b) of the individual samples using a single-cuvette configuration. The small number of measurements for each sample do not provide a reliable value of the standard deviation, but helps to identify anomalies and give the idea of the nature of the error. The theoretical standard deviation due to the resolution of the system with a 15 mm cuvette (eqs. (4.50) and (4.51)), is plotted as black solid line.

5.4.1. Single cuvette standard deviation of the refractive index

The calculated standard deviation of the refractive index shown in fig. 5.4a is a coarse estimation obtained from groups of up to 4 measurements: 3 for NA and OX samples and 4 for GA samples, with the exception of GA040, which combines the data from three different cuvettes with with 2, 3 and 4 samples recorded each. They all group around the theoretical resolution error, indicating that this might be the predominant error, only the GA120 sample seems to exhibit an anomalous behavior. It is important to notice that the variation is taking place on the fourth or fifth digit of the standard deviation, making it very susceptible to any external factor or change in the system.

The fact that samples measured with the 45 mm shows, in most cases, a larger error, indicates that this cuvette introduces additional errors with respect to the 15 mm one. Most of the samples that use the smaller cuvette are around the resolution limit. The error introduced by the resolution of the sample thickness measurement is proportional to $1/d_s$, as given by eq. (4.50). With the 45 mm cuvette being at or even above the 15 mm resolution limit, it can be concluded that the 45 mm cuvette assemblies introduce an intrinsically larger systematic error. It must be noticed, however, that this error is still small, changing no more than the fifth decimal of the refractive index.

In order to obtain more accurate estimations of the standard deviation, the total number of samples is increased by pooling the data from cuvettes of the same thickness, independently of the sample. Equations (4.37) and (4.50) show that the error

5.4. Uncertainty of the optical constants with a single-cuvette configuration

depends on the value of the optical constants when it is due to the resolution limit or to an angulation of the cuvette. Therefore, it might be necessary to introduce certain normalization to the error in order to provide an estimation using pooled data from different samples. This normalization for the error of both optical constants (n_s and α) to certain reference values (n_{ref} and α_{ref}), transforms eq. (5.4) into:

$$\hat{\sigma}_{n,norm}^{(s)} = \hat{\sigma}_{n,norm}^{(s)} f_{n=\bar{n}^{(s)}}(\omega), \quad (5.6)$$

where the normalization function, $f_{n=\bar{n}^{(s)}}(\omega)$, using the NA000 sample as a reference ($n_{ref} = n^{(NA000)}$) is:

$$f_{n=\bar{n}^{(s)}}(\omega) = \frac{n^{(NA000)}(\omega) - 1}{\bar{n}^{(s)}(\omega) - 1} \quad (5.7)$$

A detailed derivation of eq. (5.7) can be found in appendix C.

It is important to remark that this normalization is valid when the predominant error is based on a sample thickness error, including the resolution error, as shown in eq. (4.50). The reference values used in this thesis will always be, if applicable, those from the NA000 sample. The maximum and minimum values of the refractive index among all samples are 1.462 and 1.466 for NA000 and GA120, respectively, at 2 THz, where the biggest difference is found, producing a deviation on the error estimation of less than a 1%. This deviation is negligible and the normalization will be, therefore, omitted. This is not the case of the absorption coefficient, where the normalization implies a change of up to a factor of 3. The suitability of the normalization of the absorption coefficient error will be treated in the following section.

The pooled standard deviation for each sample s , $\hat{\sigma}_{n,s}$ given by eq. (5.4) is

$$\hat{\sigma}_{n,s}^{(single)}(\omega) = \sqrt{\frac{\sum_s \hat{\sigma}_s^2(\omega)(N_s - 1)}{\sum_s (N_s - 1)}} \quad (5.8)$$

The results are shown in fig. 5.5. The frequency-dependent behavior of the standard deviation for the 15 mm cuvette is given by the anomalies of the GA120 sample that can be seen in fig. 5.4a. It is important to remark, however, that this anomaly is affecting to no more than the fourth decimal of the refractive index, as the standard deviation shifts with frequency between 0.5×10^{-4} and 1×10^{-4} . Unlike the absorption coefficient, which will be treated in the following section, the frequency-dependent characteristic of the refractive index error does not repeat for all GA samples or, at least, this dependency is not sufficiently clear from the available data. Figure 5.5 shows the combined data for each cuvette thickness (15 and 45 mm), including the estimated standard deviation for 15 mm excluding the anomalous GA120 sample.

The standard deviation of the 45 mm cuvette is approximately coincident with the error introduced by a 1 degree angle. The 15 mm cuvette is also around this error

5. Distinctness of engine oil with THz-TDS

value. It is important to notice that the tilting error from eq. (4.37) is independent of the sample (i.e. cuvette) thickness. When excluding the GA120 measurement with a 15 mm cuvette, the pooled standard deviation lies even below the resolution. This is an indication of the still small number of samples available, as small changes on the data set induce relatively big changes on the error estimation. Nevertheless, it is also good indication of the resolution being the predominant source of error for this particular cuvette length.

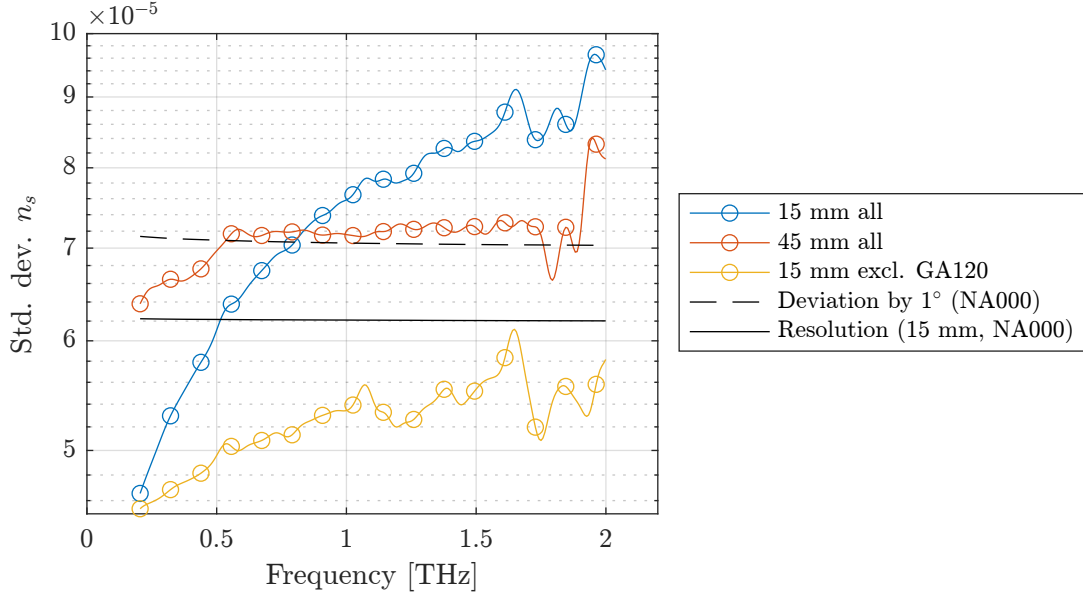


Figure 5.5.: Estimated standard deviation of the refractive index for the error using a single cuvette combining the results for different samples. The results from two rounds with different cuvette lengths are shown (15 and 45 mm). A third result, with the 15 mm cuvettes excluding the anomalous GA120 result, is also displayed. As a reference, the error for a 1 degree tilt and the resolution limit of a 15 mm cuvette (both referenced to the refractive index from NA000) are also shown.

5.4.2. Single-cuvette standard deviation of the absorption coefficient

The standard deviations of the absorption coefficient are shown in fig. 5.4b. Unlike the refractive index, where all samples (except for GA120) show similar error values and a similar frequency dependence, the measured standard deviation for the GA samples is comparatively different to the NA and OX samples. For that reason, the data is analyzed in two different set of samples: GA and NA-OX.

The pooled standard deviations of all samples are shown in fig. 5.6. Two different pooling methods are used, with and without normalizing the data, as in the previous section, now using a normalization function which is approximated by:

5.4. Uncertainty of the optical constants with a single-cuvette configuration

$$f_{\alpha=\bar{\alpha}^{(s)}}(\omega) = \frac{\alpha^{(NA000)}(\omega)}{\bar{\alpha}^{(s)}(\omega)} \quad (5.9)$$

This result is obtained by an approximation to the error from eq. (4.20). Again, the detailed derivation of eq. (5.9) is given in appendix C.

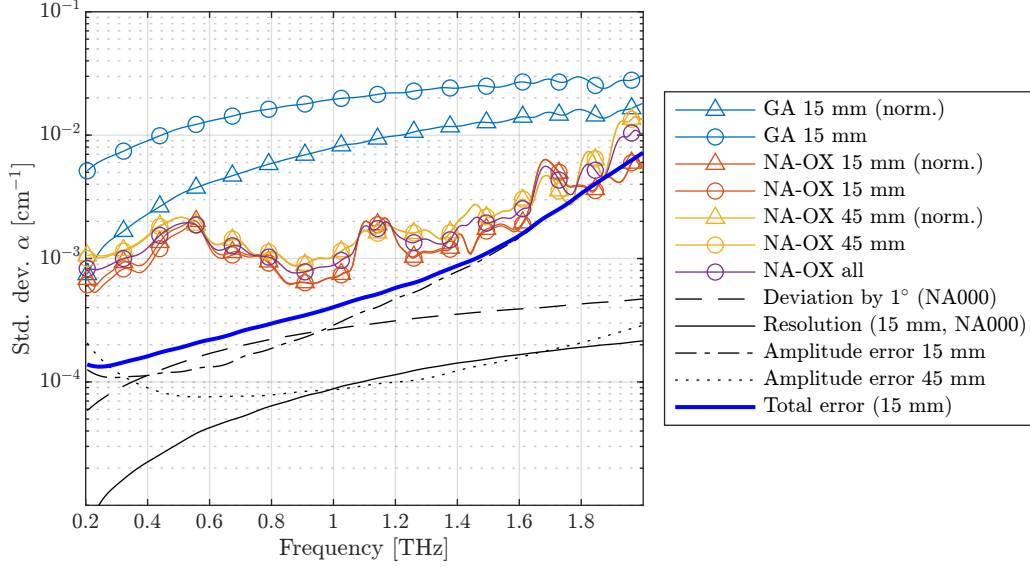


Figure 5.6.: Estimated standard deviation of the absorption coefficient for a single cuvette combining the results from different samples. The combination is performed separating the type of samples (GA and NA-OX), after observing a different behavior on the variability of the results for the individual samples (fig. 5.4b). Assuming the independence of the results for both cuvettes, the NA-OX data is pooled in a third curve (NA-OX all). GA samples were only characterize with 15 mm cuvettes. The theoretical values of the standard deviation due to resolution, eq. (4.51), 1° deviation, eq. (4.38), and noise, eq. (4.57) are also depicted, as well as the combined error for the 15 mm cuvette.

The results of the standard deviation in fig. 5.6 show several differences with respect to the refractive index:

- The observed standard deviation is much larger than the one corresponding to the resolution limit and the error originating by a 1 degree angulation with the beam axis.
- There exists a clear difference between the GA and the NA-OX samples. There are two different aspects that must be regarded: the first is that the error is up to 10 times larger for the GA samples at the central frequencies, but it must also be noticed that both standard deviations evolve very differently with frequency, showing a different nature of the error sources or the presence

5. Distinctness of engine oil with THz-TDS

of a predominant error on the GA samples that does not exist in the NA and OX samples.

- For the GA samples, which have very different absorption coefficients, the normalization implies a significant change as compared to the NA-OX samples, specially at the lowest frequencies. In this case, however, the lack of certainty about the origin of the error, which do neither fit to the resolution nor the angulation of the cuvette, makes normalization not applicable.
- The error of the NA-OX 15 mm samples seems to be dominated by noise, particularly above 1 THz.

From these results, it can be derived that not only the data obtained from the amplitude (α) is more affected by all sources of noise and error (in comparison to the n_s , which is obtained from the phase), but it will also be strongly dependent on the sample nature. In this particular case, inhomogeneity of the mixtures inside the cuvette or difference on the samples taken to fill the cuvette might introduce an additional systematic error that is made more evident through the absorption coefficient than using the refractive index.

5.5. Distinctness of the samples in a single-cuvette configuration

The error determination in the previous sections has shown a significant difference in the error of the two optical constants. While the samples are very close to each other in terms of refractive index, making it more challenging to discriminate, the phase proved more robust to certain sources of errors than the amplitude but with samples being more discernible through the absorption coefficient as they are significantly more separated. This implies two different approaches when studying the error source of the measurements.

The error of the refractive index can be directly related to the error of the manual positioning of the cuvette and the resolution limit, requiring the combination of many samples in order to discern an error different to the resolution limit. When only the individual measurements are used, consisting of no more than 4 samples, the error appears at (or even below) the resolution limit. Only after combining the results from various samples, it has been able to observe that the error source is different for each of the cuvette length mounts. In both 15 and 45 mm cuvettes, the standard deviation is close to the error corresponding to a cuvette misplaced by 1 degree in the beam path. By removing only the data from one of the samples (out of seven) of the 15 cuvette mount, it showed an error near the resolution limit of the setup.

For the absorption coefficient, however, other random and systematic errors arise and introduce a comparatively more significant error. This happens for all samples, but it is stronger in the case of the GA samples. The latter also seems to

have a less random behavior with frequency, increasing at higher frequencies. One plausible explanation for this error is the inhomogeneity of the GA samples, which consist of gasoline and motor-oil blends. As the frequency increases, a change of the beam waist and shape can be expected, changing the effective value of the optical constants of the samples. This effect is only evident on the absorption coefficient, where the error increment is also related to the gasoline quantity in the blend. The fact that this effect is not visible on the refractive index might be related to the similarities between the samples in terms of refractive index, while the difference on the absorption coefficient is much larger.

In order to quantify the error and the actual distinctness of the samples, we define an error from the previously calculated standard deviations, with the exact data that is used differing between the two optical constants:

- For the refractive index, n_s , the error bar is calculated from the pooled data from the two cuvettes, as described by eq. (5.8).
- For the absorption coefficient, α , with an error that does not correspond to neither the resolution factor nor the angulation of the cuvette, the standard deviation used for the error bar is calculated without the normalization factor. The difference between the two type of samples (GA and NA-OX) must be considered for the error bar of α , obtaining the values separately from the standard deviation of the combined samples for each family ($\hat{\sigma}_{\alpha,NAOX}$ and $\hat{\sigma}_{\alpha,GA}$).

Figure 5.7 shows the samples with the 95% confidence intervals, corresponding to $\pm 1.96\sigma_{n,s}$ and $\pm 1.96\sigma_{\alpha,s}$ (where s denotes the samples NA000, OX048, ...). The values of the optical constants were calculated using a 5 mm cuvette round where the echoes of the empty cuvette were recorded in order to provide the exact thickness of the cuvette (round R0).

Figures 5.8 and 5.9 show the evolution of the optical constants at 1.5 THz. The GA samples are much more discernible than the OX samples, as the gasoline introduces polar components into the blends that increases absorption. Despite being affected by fewer error sources, the refractive index is a worse predictor than the absorption coefficient in the case of the investigated oils. Due to Lambert-Beer law, changes in the absorption coefficient result in an exponential change of the transmission, making the transmitted THz power drop quickly, strongly increasing the uncertainty if the signal-to-noise ratio drops below a certain value, as described in eq. (4.60). Therefore, there exists a tradeoff on choosing the right length of the cuvette. While thicker samples will reduce many systematic errors and all those errors arising from the sample length uncertainty, a too thick sample will drop the SNR, introducing errors originating from noise.

Optimal cuvette thickness

Using the approach described in section 4.2.7 by eq. (4.62), the optimal thickness that minimizes the error of the absorption coefficient can be calculated. The results

5. Distinctness of engine oil with THz-TDS

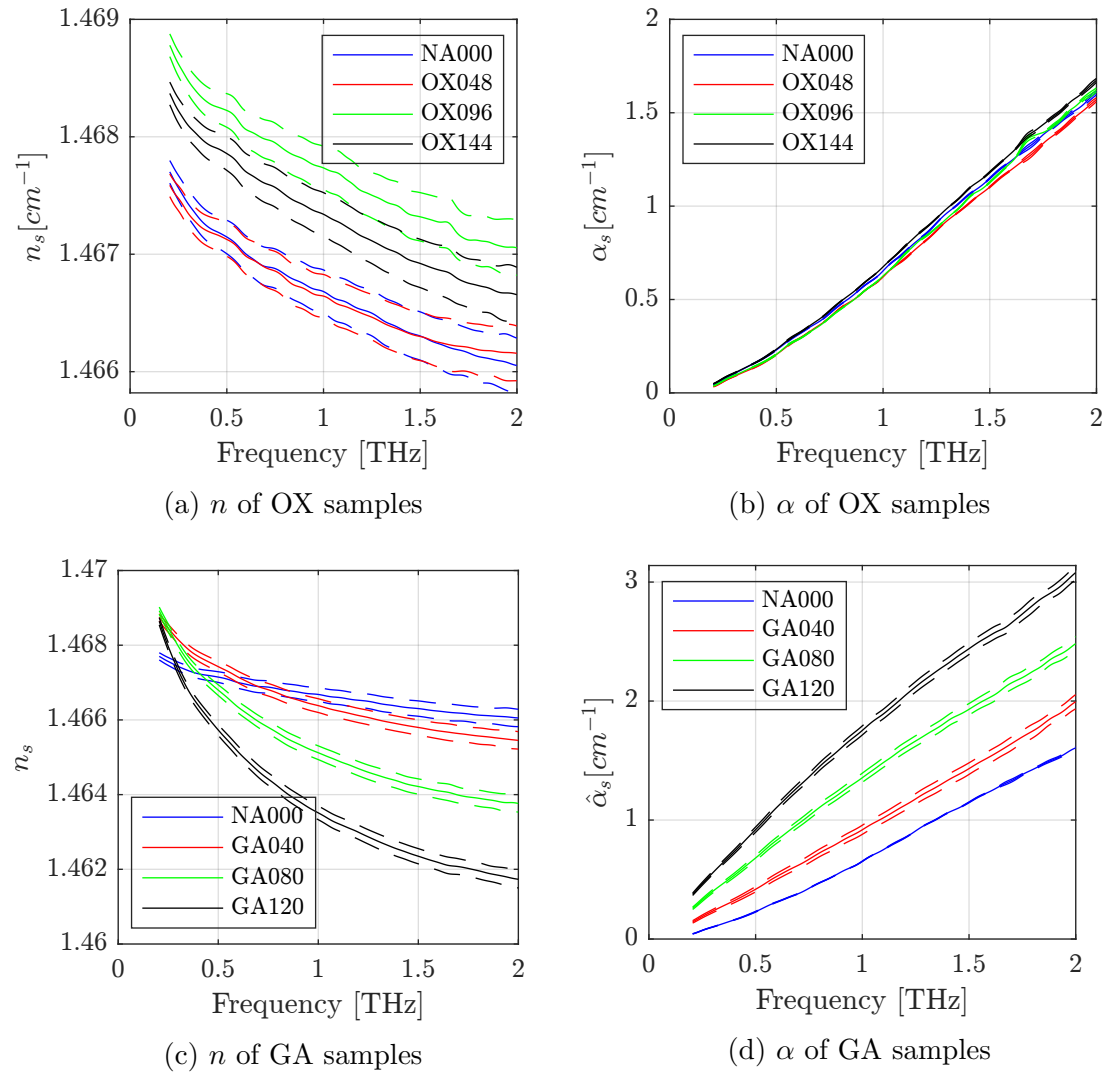


Figure 5.7.: Absorption coefficient and refractive index of all samples with the 95 % confidence interval (indicated with dashed lines) for a single, well known length of the cuvette.

5.6. Uncertainty of the optical constants using multiple cuvettes

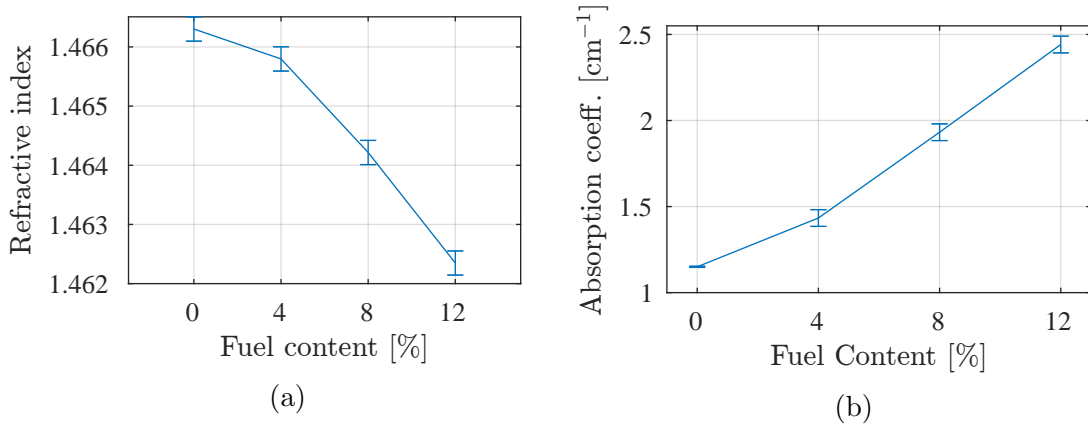


Figure 5.8.: Distinctness of the GA samples at 1.5 THz.

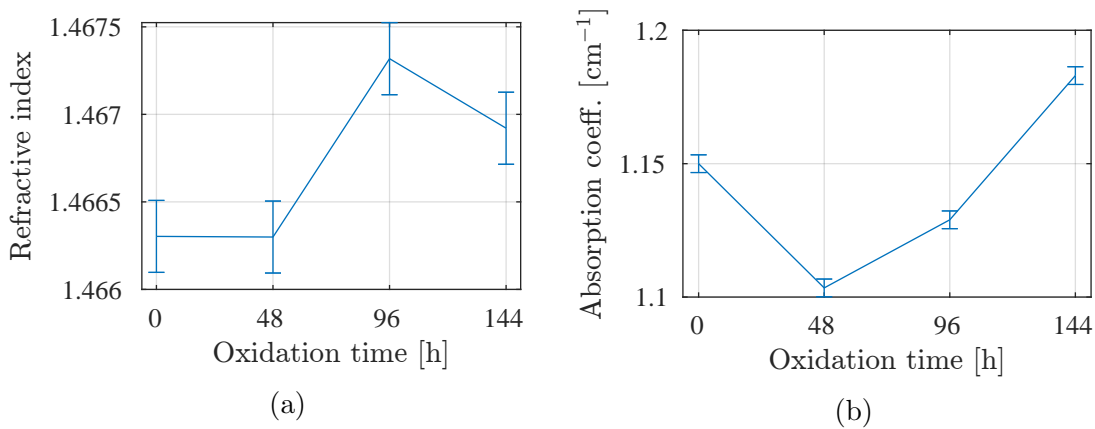


Figure 5.9.: Distinctness of the OX samples at 1.5 THz.

are shown in fig. 5.10. As it was expected from the theory in section 4.2.7, there is no single optimal cuvette length as the SNR and the absorption coefficient change with frequency. In this case, analysis has been extended beyond 2 THz in order to see how the optimal cuvette length converges below a certain SNR. Depending on the experiment needs, different cuvette thickness can be chosen to minimize the error. In general, higher frequencies (i.e. lower SNR) require thinner samples.

5.6. Uncertainty of the optical constants using multiple cuvettes

The next step on the error analysis consists of looking at the error originating from the variability of the sample thickness other than that originating from the cuvette measurement device or the tilted positioning of the cuvette. For this purpose, the thickness variation originating from different mounts of the cuvettes is used as the error source. The estimated uncertainty originating from this mounting and

5. Distinctness of engine oil with THz-TDS

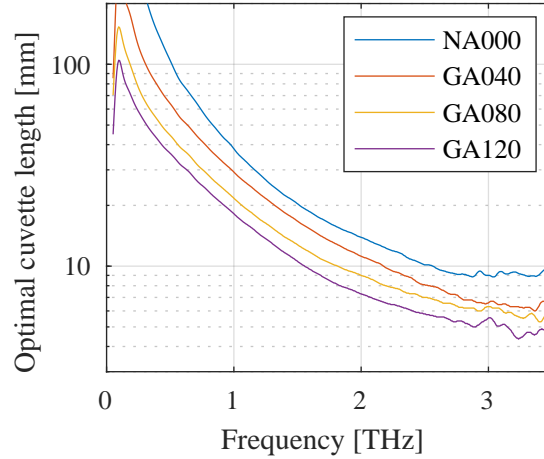


Figure 5.10.: Optimal cuvette length for the NA and the GA samples. The cuvette length standard deviation used is $\sigma_d = 3 \mu\text{m}$, corresponding to the one empirically obtained for a single cuvette in section 5.3.

unmounting process was shown in section 5.3.2, obtaining a standard deviation of the cuvette length of $12.06 \mu\text{m}$, significantly larger than the one produced by an angled positioning or the resolution, which were established around 2 to $3 \mu\text{m}$ (see section 5.3). Rounds R0 to R4 conform the data used in this analysis (see section 5.2.2). In R4, where several measurements are taken for each cuvette mount, the mean value is taken for each of the seven samples.

5.6.1. Intra-round error metrics

The error is estimated within each of the rounds. This is because different rounds might have different optical configurations (i.e. system alignments) which might introduce additional systematic errors. Therefore, the error is calculated for each round from the seven different samples, using the variability of the optical constants from the nominal value given by R0 as the error metric.

Figure 5.11 shows the necessity for this new metric: While the average variation of the refractive index for each sample is similar in both rounds, there exists an offset which, for this particular case, is almost symmetrical around the origin, indicating the presence of a systematic error that appears between rounds. Therefore, it is only possible to analyze the variations due to the cuvette thickness random error isolating each round from other systematic errors.

The error metric data is therefore obtained for a round R_k , as

$$\Delta n_s^{(k)}(\omega) = n_s^{(k)}(\omega) - n_s^{(0)}(\omega) \quad (5.10a)$$

$$\Delta \alpha_s^{(k)}(\omega) = \alpha_s^{(k)}(\omega) - \alpha_s^{(0)}(\omega), \quad (5.10b)$$

where $n_s^{(k)}$ and $\alpha_s^{(k)}$ are the refractive index (n_s) and absorption coefficient (α) of

5.6. Uncertainty of the optical constants using multiple cuvettes

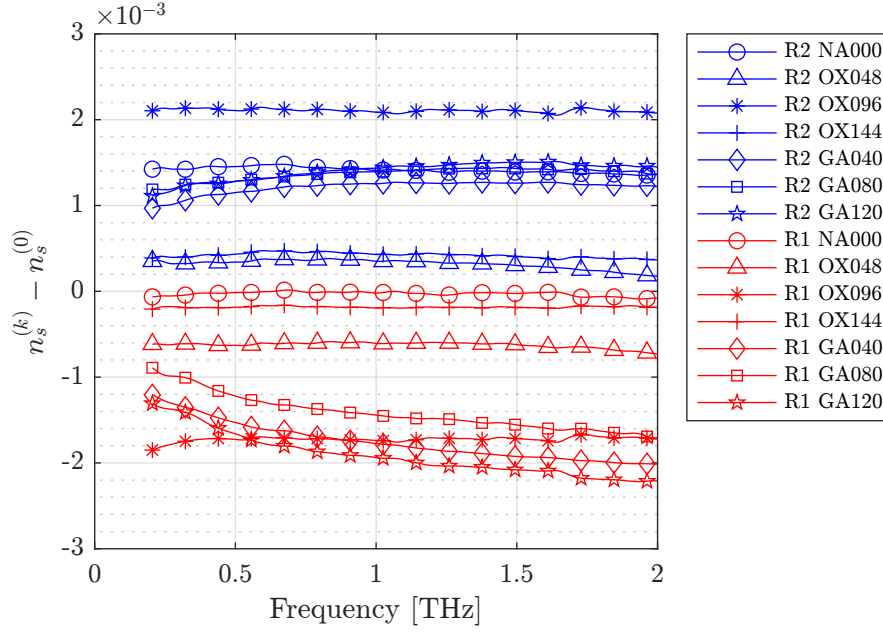


Figure 5.11.: Deviation of the refractive index of all samples from rounds R1 (red) and R2 (blue) (both using the nominal 10 mm spacer) with respect to the calibrated values given in R0.

sample s in round Rk, denoted as (k) . $n_s^{(0)}$ and $\alpha_s^{(0)}$ are the data, taken with calibrated cuvettes, in round R0.

The error is then calculated as the standard deviation of the variability of all samples within a round with respect to the reference sample R0 as

$$\hat{\sigma}_{n,multi}^{(k)}(\omega) = \sqrt{\frac{\sum_{s=0}^{N_s-1} \left(\Delta n_s^{(k)}(\omega) - \overline{\Delta n^{(k)}}(\omega) \right)^2}{N_s - 1}} \quad (5.11a)$$

$$\hat{\sigma}_{\alpha,multi}^{(k)}(\omega) = \sqrt{\frac{\sum_{s=0}^{N_s-1} \left(\Delta \alpha_s^{(k)}(\omega) - \overline{\Delta \alpha^{(k)}}(\omega) \right)^2}{N_s - 1}}, \quad (5.11b)$$

where N_s is the number of samples (typically seven, if there is none excluded, namely NA000, OX048, OX096, OX144, GA040, GA080 and GA120). The terms $\overline{\Delta n^{(k)}}(\omega)$ and $\overline{\Delta \alpha^{(k)}}(\omega)$ are the mean value of the variation throughout all samples s , i.e. $\Delta n_s^{(k)}(\omega)$ and $\Delta \alpha_s^{(k)}(\omega)$, in round Rk.

As the standard deviation is being calculated using data from different samples, a normalization might be necessary if the error is mainly due to the cuvette thickness uncertainty, eq. (4.46), or the resolution, eq. (4.51). The small differences in the refractive index makes the normalization unnecessary, in contrast to the absorption coefficient. The estimated standard deviation applying normalization is calculated

5. Distinctness of engine oil with THz-TDS

adding to eq. (5.11b) the normalization factor $f_\alpha(\omega)$. Unlike in eq. (5.5), the normalization factor is now different for each value used to calculate the standard deviation, as each of them corresponds to a different sample, resulting in

$$\hat{\sigma}_{\alpha,norm}^{(k)}(\omega) = \sqrt{\frac{\sum_{s=0}^{N_s-1} \left[\left(\Delta\alpha_s^{(k)}(\omega) - \overline{\Delta\alpha^{(k)}}(\omega) \right) f_{\alpha_s}(\omega) \right]^2}{N_s - 1}}, \quad (5.12)$$

where the normalization factor, $f_{\alpha_s}(\omega)$, is calculated as in eq. (5.9) as $f_{\alpha_s}(\omega) = \alpha^{(NA000)}/\alpha_s(\omega)$.

From the estimation given in eq. (5.12), the error of a specific sample s can be obtained denormalizing it as $\hat{\sigma}_{\alpha,multi}^{(s,k)}(\omega) = \hat{\sigma}_{\alpha,norm}^{(k)}(\omega)/f_{\alpha_s}(\omega)$.

5.6.2. Standard deviation of the measurements using multiple cuvettes

Figure 5.12 shows the results for all rounds, (R0', R1, ... R4). The estimated standard deviation of the refractive index, $\hat{\sigma}_{n,multi}(\omega)$ scales with d_s^{-1} (fig. 5.12a), as expected from eq. (4.45). The theoretical values are calculated for a standard deviation of $\sigma_d = 12.1 \mu\text{m}$, estimated in section 5.3. In the case of the R0' round, free from other systematic errors, the coincidence is almost perfect. For the other rounds, the standard deviation scales with the sample thickness, not far from the theoretical values, specially considering the relatively small number of samples. They all exhibit a colored (i.e. frequency dependent) characteristic, while the theory shows an almost constant error along the frequency span.

Regarding the absorption coefficient, the results are very different. While R0' shows again an almost perfect match with the theoretical values, confirming the adequacy to the error model from eq. (4.46), the error of the other rounds is more than one order of magnitude higher than that of R0'. This might indicate the presence of error sources that affect strongly to the absorption coefficient, α , but not to the refractive index, n_s .

The frequency dependent uncertainty of the refractive index can be analyzed by looking at the maximum variation of the standard deviation, $\sigma_n(\omega)$, within the bandwidth of interest (0.2 to 2 THz) ($\max\{\sigma_n\} - \min\{\sigma_n\}$). The results are shown in fig. 5.13a, showing a clear bias in most rounds for the GA samples (i.e., the error is, in general, more frequency dependent), which therefore features certain systematic errors which are not in the NA and OX samples.

While fig. 5.7c shows that the GA samples are, in general, more dispersive, the refractive index does not change by more than 0.5% and cannot affect to the error in the way that can be seen in fig. 5.12a. In fig. 5.13b the differential refractive index between two rounds is displayed. It shows how the colored systematic error between rounds appear only for the GA samples, while it is constant for the NA-OX samples. This reinforces the idea of the colored error originating at actual slightly different concentration of gasoline from the nominal value between the samples taken from

5.6. Uncertainty of the optical constants using multiple cuvettes

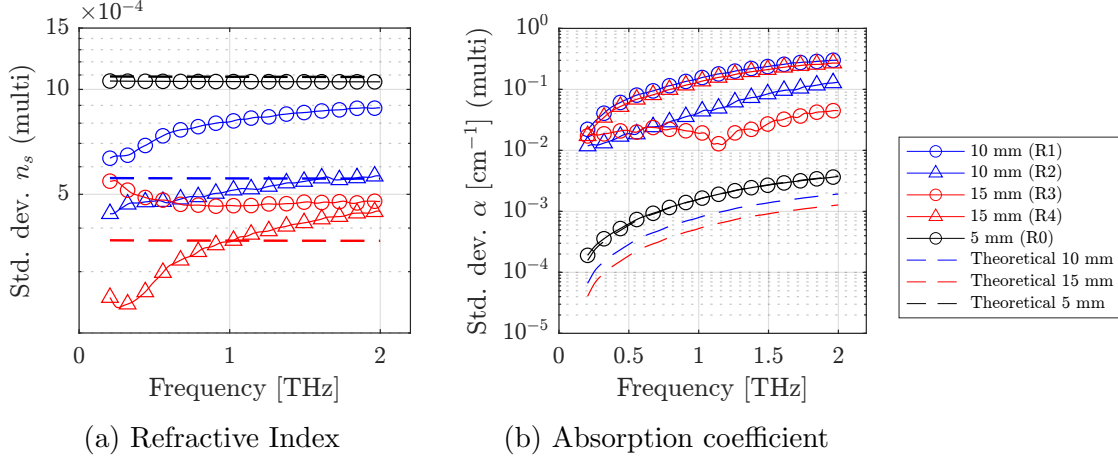


Figure 5.12.: Estimation of the standard deviation of the optical constants from the different rounds. The theoretical value corresponds to a uncertainty of the cuvette thickness of $\sigma_d = 12.1 \mu\text{m}$. The standard deviation of the absorption coefficient is calculated using the normalized error metric, as described in eq. (5.12).

the bottle for different measurement rounds or mixture inhomogeneities inside the cuvette.

It can be interesting to obtain an uncertainty for the NA and the OX samples only, excluding the samples that present additional systematic errors. This brings, however, one additional problem, as the number of samples that are taken from each round reduces from seven to only four, further reducing the reliability of the estimation. In order to avoid that, the standard deviations from the cuvettes with the same thickness can be combined in order to increase again the number of samples to eight in two independent sets. This is again done by pooling the standard deviations, which for the 10 mm cuvette results in

$$\hat{\sigma}_{n,multi}^{(10 \text{ mm})}(\omega) = \sqrt{\frac{\hat{\sigma}_{n,multi}^{(R1)}(\omega)(N_{R1} - 1) + \hat{\sigma}_{n,multi}^{(R2)}(\omega)(N_{R2} - 1)}{(N_{R1} - 1) + (N_{R2} - 1)}}, \quad (5.13)$$

where N_{R1} and N_{R2} are the number of samples being used from rounds R1 and R2, which is now 4 in both cases.

The same is also done for the 15 mm cuvette, with rounds R3 and R4 and with the data of the absorption coefficient, which is now taken from non-normalized data, as fig. 5.12b did not show a clear fit to the thickness uncertainty models that justify the normalization.

The result is shown in figure fig. 5.14. Now the theoretical uncertainty is adjusted matching the result from R0'. The resulting theoretical errors are calculated for $\Delta d = 14 \mu\text{m}$, which does not differ significantly from the value that resulted from

5. Distinctness of engine oil with THz-TDS

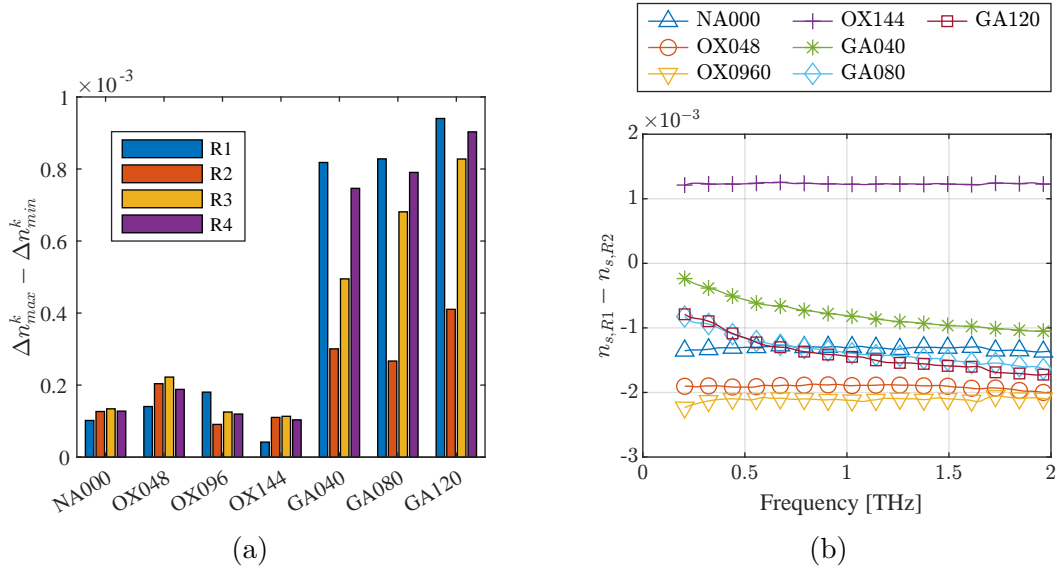


Figure 5.13.: Tests for the presence of systematic errors in the GA samples: (a) Maximum variation of the refractive index for each sample and round. (b) Difference between rounds R1 and R2.

the cuvette characterization¹.

Figure 5.14 shows that the estimated standard deviation of the refractive index is in very good agreement with the theoretical values. For the absorption coefficient, however, there are additional errors that make it to be more than one order of magnitude above the theoretical standard deviation caused by the cuvette length uncertainty.

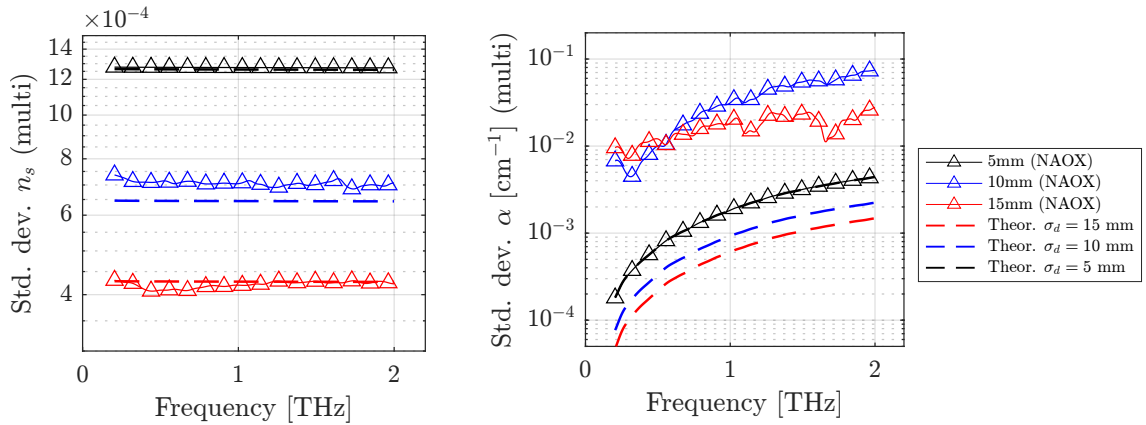


Figure 5.14.: Estimated standard deviation with multiple cuvettes grouped by sample thickness.

¹Due to the reduced number of samples used to estimate the $12.1 \mu\text{m}$ value in section 5.3, this difference is almost negligible.

5.7. Other sources of error and summary

In the previous section, we isolated the random error produced by the sample thickness uncertainty for the refractive index, independently of the setup configuration, and demonstrated the adequacy of the model from eqs. (4.19) and (4.20) to estimate the maximum error. The absorption coefficient was, however, dominated by amplitude error (noise) and other systematic errors. There are further systematic and random errors which were not identified and that will appear between rounds. For example, errors on the measurement sample preparation by extracting an imprecise mixture from the sample glass bottle.

To this point, the uncertainty of the optical constants n_s and α demonstrated a well differentiated origin of the error. Furthermore, GA samples showed a different error characteristic than NA and OX:

- The absorption coefficient (α), suffers more from variations of the setup, with the error more than one order of magnitude above the theoretical values for any data set other than the reference measurement, R0' (fig. 5.12).
- The gasoline blend samples (GA) exhibits a colored error that increases at higher frequencies. This is probably caused by the inhomogeneity of the sample and the change of the shape of the Gaussian terahertz beam through the sample with frequency.

In order to quantify further systematic errors of unknown origin, a new standard deviation is calculated without subtracting systematic errors arising between rounds. Denoting the refractive index and the absorption coefficient of sample s , corresponding to each of the seven samples (NA000, OX048, . . . , GA120), in round k as $n_s^{(k)}$ and $\alpha_s^{(k)}$, the complete standard deviation of sample s is calculated from

$$\hat{\sigma}_{n,(s,all)}(\omega) = \sqrt{\frac{\sum_{k=0}^{N_K-1} \left(n_s^{(k)}(\omega) - \overline{n_s}(\omega) \right)^2}{N_K - 1}} \quad (5.14a)$$

$$\hat{\sigma}_{\alpha,(s,all)}(\omega) = \sqrt{\frac{\sum_{k=0}^{N_K-1} \left(\alpha_s^{(k)}(\omega) - \overline{\alpha_s}(\omega) \right)^2}{N_K - 1}}, \quad (5.14b)$$

where $\overline{n_s}(\omega)$ and $\overline{\alpha_s}(\omega)$ and are the average values of sample s among every round Rk and $N_K = 5$ is the number of measurement rounds which are being considered (R0 to R4).

Figures 5.15 and 5.16 show the total standard deviation defined from eq. (5.14) in comparison with the standard deviation defined in previous sections for the single-cuvette (section 5.3) and multiple-cuvettes setups (section 5.6), respectively. The graphs compound the following data:

5. Distinctness of engine oil with THz-TDS

1. The **blue bars** represents the error from single-cuvette setups for each individual sample. The standard deviation for each sample was described in section 5.5 and is obtained differently for the GA and the NA and OX samples:
 - For the NA-OX, the standard deviation is calculated from the pooled standard deviation of the 15 mm described in eq. (5.8).
 - With an unclear origin of the GA samples error, the normalization is also not applied. Again the pooled standard deviation for 15 mm is used.
2. The **red bars** represent the error from multiple-cuvette setups. It uses the pooled standard deviation of the two 15 mm rounds, only using the data from NA and OX samples, which are free of systematic errors that appear on the GA samples, as described in section 5.6, where the standard deviation from rounds R3 and R4 have been pooled as described in eq. (5.13).
3. The **yellow bars** represent the overall standard deviation for each sample calculated from eq. (5.14).

When analyzing figs. 5.15 and 5.16, it must be considered that, while the single and multiple cuvette uncertainty results have been obtained from 15 mm cuvettes, the overall uncertainty described in this section is not attached to any sample thickness in particular. It is still a good indicator on the amplitude of systematic errors that appear between rounds, concluding that:

- The standard deviation of the **refractive index** (n_s) reaches the resolution limit using a single-cuvette with a well calibrated thickness ($\sigma_n \sim 1 \times 10^{-4}$). When using multiple cuvettes, the uncertainty is explained directly by the uncertainty of the cuvette length and is very robust against systematic errors, with a standard deviation of ($\sim 4 \times 10^{-4}$) for 15 mm cuvettes. The GA samples seem to have a small intrinsic systematic error, as compared to the NA and OX samples, which is more evident at the highest frequencies, exceeding the error due to the cuvette dimension uncertainty by a factor of two ($\sim 1.2 \times 10^{-3}$ at 2 THz).
- The standard deviation of the **absorption coefficient** (α) is above the resolution limit with a single-cuvette, with the additional error being likely explained by the error introduced by the amplitude uncertainty (i. e. the noise) of the THz signals, specially at higher frequencies, where the SNR drops. This standard deviation of the NA and OX samples was estimated around $0.7 \times 10^{-3} \text{ cm}^{-1}$ at 1 THz. At this point, systematic errors in the GA samples are already visible, exceeding 10^{-2} cm^{-1} at 1 THz. This difference with the NA-OX samples reduces at higher frequencies, where the signal to noise ratio (SNR) starts to be considerable. With multiple-cuvettes, the error is at least one order of magnitude larger than the uncertainty due to thickness variations. The NA and OX samples are not considerably affected by any other systematic

errors between rounds, but the GA samples are. Time and potential changes of the setup over days or weeks, or the changes on the samples themselves along time introduce an important source of systematic error in the GA samples, peaking at $3 \times 10^{-1} \text{ cm}^{-1}$ at 2 THz. The systematic error is clearly dependent on the GA content, increasing as the fuel proportion increases.

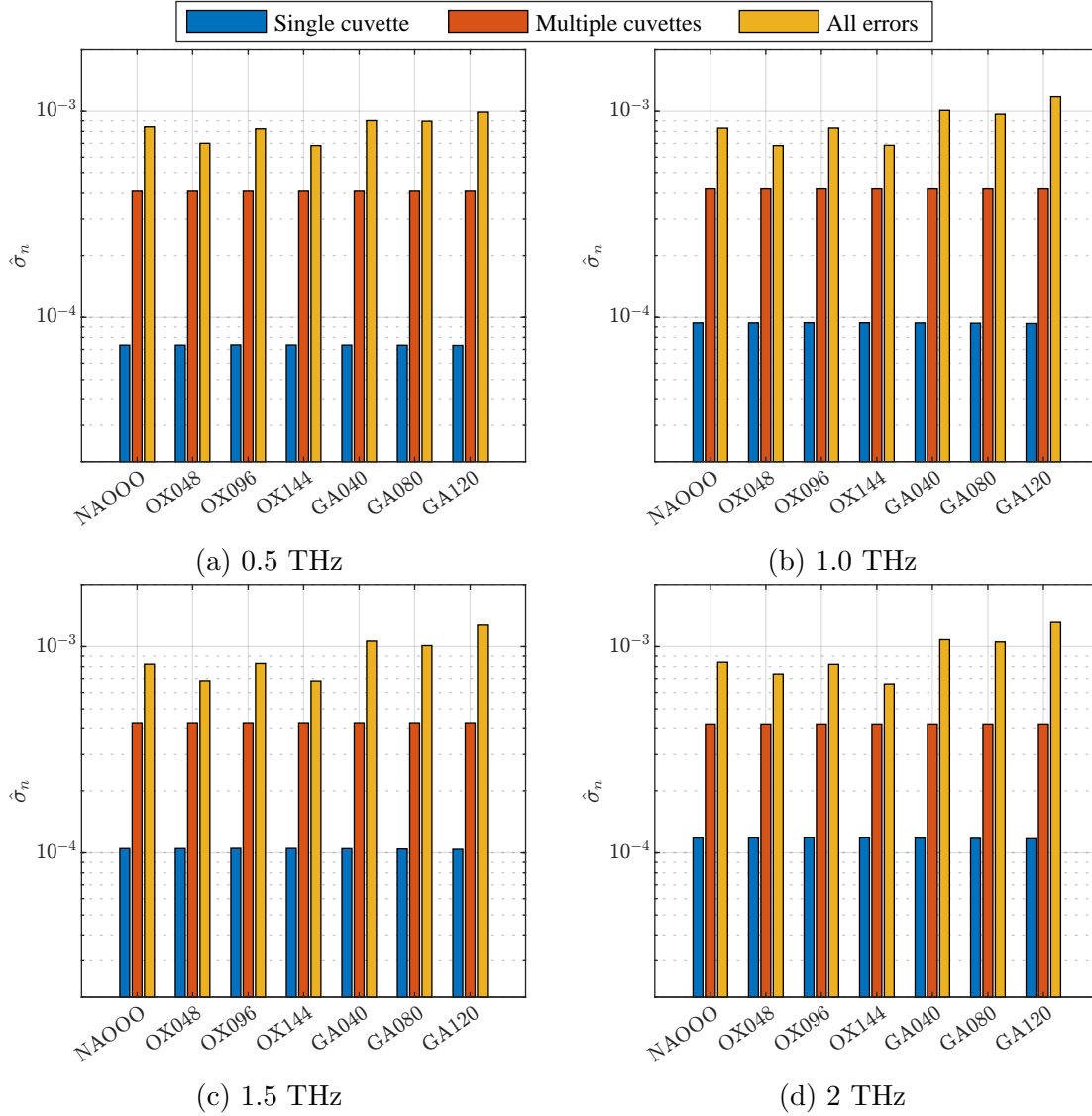


Figure 5.15.: Uncertainty summary of the refractive index.

5. Distinctness of engine oil with THz-TDS

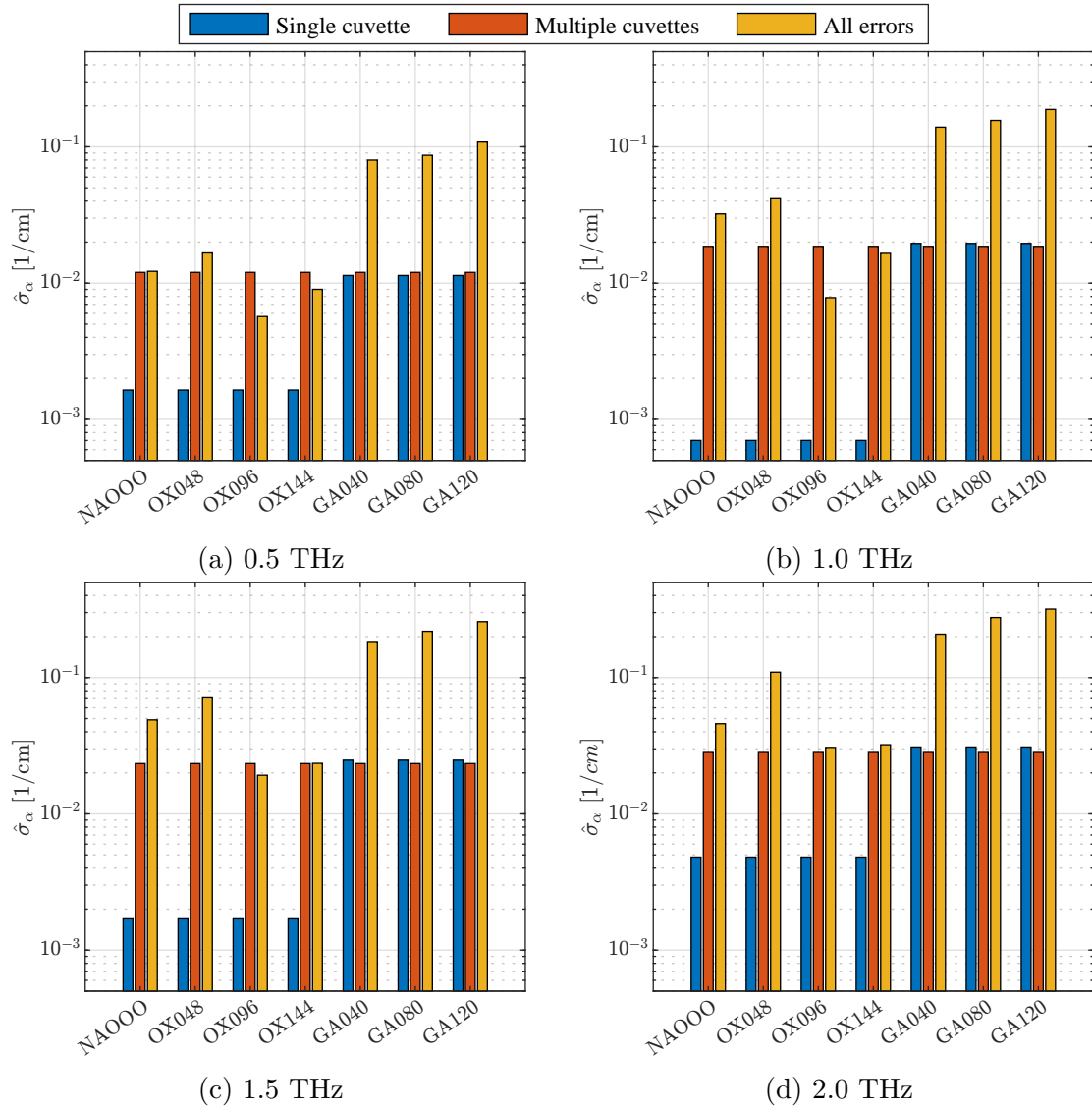


Figure 5.16.: Uncertainty summary of the absorption coefficient.

6. Broadband characterization of biodiesel blends

6.1. Introduction and motivation

With knowledge on the measurement accuracy of the spectroscopy system from the previous chapter, we now extend measurements to biodiesel blends.

Diesel engines combustion products are a health and environmental hazard [79–81]. Biodiesel is a fundamental component to reduce emissions, helping to keep carbon dioxide within a closed loop between the exhaust and the plant.

The most extended method so far to determine the biodiesel concentration in diesel oil blends is Fourier transform infrared spectroscopy (FTIR). One of the most important characteristics corresponds to the strong absorption peak at 1740 cm^{-1} (52.16 THz) introduced by the polar functional ester group which is present in the biodiesel molecule. This peak has been used as a biodiesel content indicator using the peak amplitude and the area under the curve of the absorption peak [82]. This method is defined as a European standard in EN 14078 [83]. Partial least squares (PLS) regression has also been used to obtain broadband spectral information [84], and is also defined by the international standard D7371-14 [85]. These FTIR methods and standards require of very well controlled experiments that must be carried out ex-situ.

THz-TDS has been already applied to characterize the biodiesel content in blends [86] and the optical properties of its base stock [87]. These previous works were limited to a bandwidth of 0.2 to 1.6 THz and correlated the characteristics of the different fuels and base stock compounds to the absorption coefficient at specific frequencies. In reference [87], cetane number (CN) and solidifying point (SP) are related to the absorption using different models obtained for individual frequencies and averaging the result. They therefore rely on independent calculations over several frequency points and systematic error and changes on the experimental conditions cannot be identified and compensated. As the absorption spectrum of pure biodiesel (B100) peaks at around 1.5 THz, there exists a well defined shape of the curve which might characterize the sample. With information available up to 3.5 THz and using non-polar liquid models, it will be demonstrated that it is possible to characterize the blends from the fit of the absorption coefficient to a model. This approach should offer an improved robustness against individual points characterization, as systematic errors usually do not change the shape of the absorption coefficient curve.

6. Broadband characterization of biodiesel blends

This chapter studies the biodiesel in petroleum diesel blends using a commercially available THz-TDS system by recording the absorption coefficient between 0.5 THz to 3.5 THz. The long hydrocarbon molecules that form the fuels are principally non-polar and they do not feature any distinctive absorption peak in the THz range, but they feature certain broadband characteristics of the absorption that can be used to identify the content of the different blends. This could be a solution for in-situ and real-time quality control, more robust to the variability of the measurement environment than the methods relying on individual frequency points. The results of this study were published in [88].

The chapter is structured as follows: first, models for the individual components, diesel (B0) and biodiesel (B100), are described starting from the assumption of a non-polar characteristic of the absorption. Using these models, a characterization method of the biodiesel content, based on the linear combination between the two components is presented. Similar results are later shown using the data provided by a real time THz-TDS (at 9 traces/s). Finally, a new characterization method based on the maximum recorded dispersion is presented.

6.2. THz-TDS setup and sample description

THz-TDS setup

The measurement of the optical constants, $n_s(\omega)$ and $\alpha(\omega)$, have been obtained with the same commercial THz-TDS system from Menlo Systems GmbH that was described and utilized in chapters 4 and 5 (see figs. 4.1 and 5.2). The same type of cuvette has been used, consisting of two 3 mm thick polyethylene (PE) windows, with an optical aperture of 35×35 mm, separated by a metallic spacer and clamped using two symmetric metal frames and two cylindrical sealing gaskets. The spacer used in this case had a nominal thickness of 2.3 mm.

The whole THz beam path is purged with dry nitrogen in order to eliminate water vapor absorption.

Sample set

Seven different blends of biodiesel (B100) and diesel (B0), with nominal biodiesel volumetric content of 0%, 5%, 10%, 20%, 50%, 80% and 100% (denoted B0, B5, B10, B20, B50, B80 and B100), were characterized. B100 consists of palm-based biodiesel meeting MS2008:2014 specifications [89] and B0 is 10 ppm sulfur diesel under the MS123-3:2016 specification [90].

Two sets of data were recorded: one for averages over 500 s (corresponding to 4500 spectra) and a second one with single shot measurements. Each data set was measured using a different cuvette mount.

The measurement procedure was identical for each data set. After the cuvette was mounted, a first reference measurement with the empty cuvette was performed, followed by the measurement of each of the blends in ascending order of biodiesel

concentration. The first measurement with the empty cuvette corresponded to the reference measurement.

The length of the cuvettes were measured from the first echo of the reference measurement of the empty cuvette at $2.350 \text{ mm} \pm 5 \text{ }\mu\text{m}$ for the 500 s integrates reference measurement and $2.370 \text{ mm} \pm 5 \text{ }\mu\text{m}$ for the single-shot reference. The uncertainty on the cuvette thickness arises from the temporal resolution of the measurement, set to 0.033 ps. The discrepancy of $20 \text{ }\mu\text{m}$ between the thickness of the two cuvettes is explained by the assembly process, which introduces an error which much larger than the resolution error of around $5 \text{ }\mu\text{m}$ which is applied to each of the cuvette.

The recorded pulses of samples B0 and B100 and their spectra (Fourier Transforms) are shown in fig. 6.1. The spectra are normalized to the noise level, obtained from the highest frequencies, yielding the signal to noise ratio (SNR). The window size and thickness have been chosen in order to avoid any overlap of the main pulses with the echoes. This allows the removal of the etalon effects using a *hann* window around the main peak. The Hann windows are illustrated as black solid lines in figs. 6.1a and 6.1c for the single-shot and the 500 s integrated time-signals. The optical constants $n_s(\omega)$ and α are calculated using eq. (4.10), assuming again that the imaginary refractive index is negligible for (i.e. $\kappa_s \ll n_s$).

6.3. Absorption models for diesel and biodiesel

From the recorded data for the individual constituents, B0 and B100, two models, based on non-polar liquids are fitted.

Both biodiesel and diesel are mixtures of multiple hydrocarbon compounds. Petroleum-diesel is mostly composed of non-polar alkanes and only some slightly polar aromatic hydrocarbons. The main molecule of biodiesel, fatty acid methyl ester (FAME), is polar at its ester functional group (R-COO-R), but the largest part of the hydrocarbon chain is essentially non-polar [91].

6.3.1. Non-polar liquid model for diesel

Unlike in polar liquids, where the electromagnetic field causes the oscillations of the permanent dipole moments with subsequent Debye relaxation that causes a high absorption at the far-infrared and THz regions, non-polar liquids show a much smaller absorption. It originates from transient dipole moments induced, among other reasons, by the collision between molecules.

The absorption of liquids is related to the dipole correlation function, which is defined as [92]

$$C(t) = \sum_u \sum_v \langle \vec{\mu}_u(0) \cdot \vec{\mu}_v(t) \rangle , \quad (6.1)$$

where $\vec{\mu}_v(t)$ is the dipole moment of the molecule v at time t . The variation of the

6. Broadband characterization of biodiesel blends

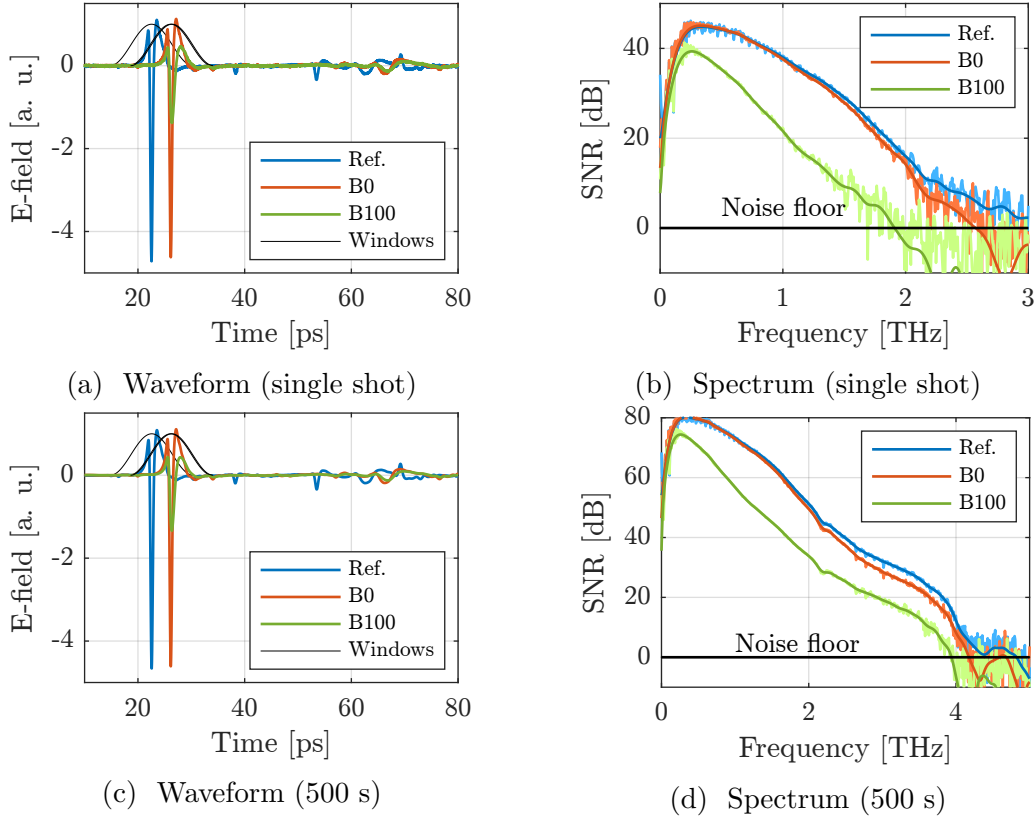


Figure 6.1.: Recorded time traces and spectra of the pure diesel and biodiesel samples (B0 and B100). The background spectra depicted in pale colors correspond to the spectra calculated from the raw time signals, before applying the Hann windows (© 2021 IEEE).

correlation function can be expressed using a memory function $K(t)$ as

$$\frac{dC(t)}{dt} = - \int_0^t K(t - \tau)C(\tau)d\tau \quad (6.2)$$

Equation (6.2) can be expressed using a series of kernel functions $K_0(t)$, $K_1(t)$, \dots , $K_n(t)$ that fulfill [93]:

$$\frac{dK_{n-1}(t)}{dt} = - \int_0^t K_n(t - \tau)K_{n-1}(\tau)d\tau \quad (6.3)$$

Laplace transform of eq. (6.2) using eq. (6.3) yields a fraction expansion of the form [94]

$$C(p) = \frac{C(0)}{p + K_0(p)} = \frac{C(0)}{p + \frac{K_0(0)}{p + K_1(p)}} = \dots \quad (6.4)$$

Truncations of eq. (6.4) can describe many fluctuations in liquids. A first-order memory function of the form $K_0(t) = 1/\tau_D \delta(t)$ corresponds to the Debye-relaxation

for a relaxation time τ_D [95]. The absorption of non-polar liquids is proportional to the real part of the spectral function $C(j\omega)$ using the second order memory function $K_1(t) = K_0(0) \cdot \exp(-\gamma t)$ [92, 96]:

$$\alpha(\omega) = \frac{D_t \omega^2}{n_s(\omega) c_0} \Re[C(j\omega)] , \quad (6.5)$$

where $D_t = \epsilon_0 - \epsilon_\infty$ is the dispersion, c_0 is the speed of light in vacuum and $n_s(\omega)$ is the refractive index of the sample.

Therefore, the model for non-polar liquids absorption and the model used in this work for the absorption of petroleum diesel, is

$$\alpha_D(\omega) = \frac{D_t}{n_s(\omega) c_0} \cdot \frac{\gamma K_0 K_1 \omega^2}{\gamma^2 (K_0 - \omega^2)^2 + \omega^2 (\omega^2 - K_1 - K_0)^2} , \quad (6.6)$$

The parameters for the absorption model of non-polar liquids (and here the petroleum diesel) are: $K_0 = K_0(0)$ in ps^{-2} , $K_1 = K_1(0)$ in ps^{-2} , γ in ps^{-1} and D_t .

6.3.2. Modified model for biodiesel

Previous measurements of biodiesel featured strong difference between different refinements due to undesirable by-products, such as glycerol and ethanol, which are polar substances [87, 97] that increase the overall absorption.

A linearly increasing term in the absorption that accommodates an additional polar behavior, either from residual by-products or by the polar part of the FAME molecule, must be included in order to accommodate the model from eq. (6.6) to biodiesel. A new parameter g in $\text{cm}^{-1}/\text{ps}^{-1}$ is therefore added to eq. (6.6), obtaining a model for biodiesel given by

$$\alpha_{BD}(\omega) = \frac{D_t}{n_s(\omega) c_0} \cdot \frac{\gamma K_0 K_1 \omega^2}{\gamma^2 (K_0 - \omega^2)^2 + \omega^2 (\omega^2 - K_1 - K_0)^2} + g \cdot \omega \quad (6.7)$$

6.3.3. Data fit to models

The models for B0 and B100 are obtained for the data between 0.5 and 3.5 THz, integrated over 500 s (4500 waveforms). While data can be accessed well below 50 GHz, the errors increase at low frequencies. Therefore, a lower bound of 0.5 THz is chosen. The upper bound of 3.5 THz ensures a SNR of at least 20 dB for integration time of 500 s.

Figure 6.2 shows the measured absorption coefficients of pure diesel (B0) and biodiesel (B100), with excellent agreement to the models from eqs. (6.6) and (6.7), respectively. The absorption of pure diesel peaks at around 3.2 THz with $\alpha \approx 4 \text{ cm}^{-1}$, while biodiesel (B100) features a more pronounced peak around 1.5 THz with $\alpha \approx 19 \text{ cm}^{-1}$.

The fit values to the models from eqs. (6.6) and (6.7) are summarized in table 6.1. They are in agreement with physical boundary conditions:

6. Broadband characterization of biodiesel blends

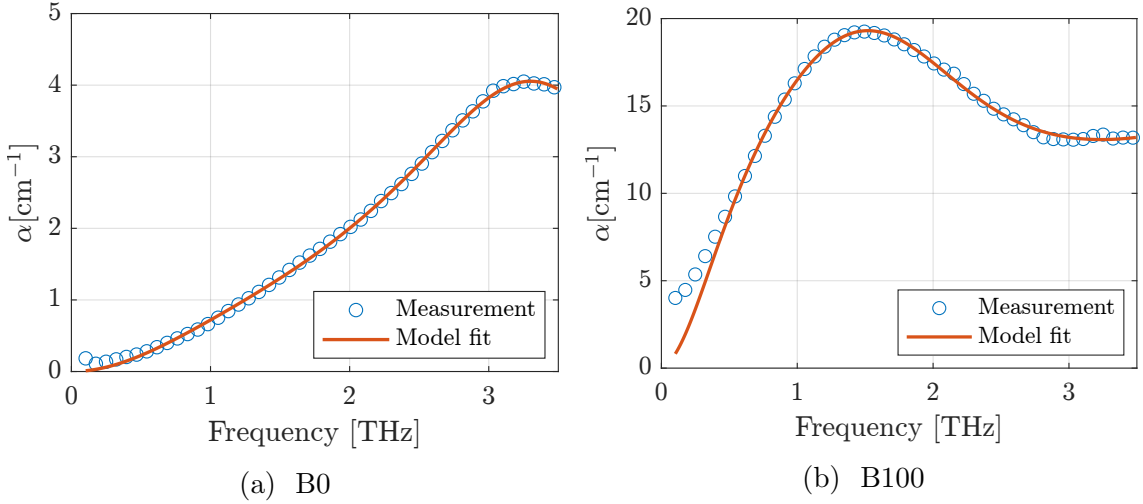


Figure 6.2.: Absorption coefficient of petroleum diesel (B0) and (B100) and the fit to the model from eqs. (6.6) and (6.7)

- The parameter D_t approximates the difference between the maximum and the minimum values of the permittivity ($\epsilon = n_s^2$) recorded within the measurable range (0.2 and 3.5 THz), i.e. $D_t^{ap} = n_{s,max}^2 - n_{s,min}^2$, as shown in table 6.1.
- The model parameters K_1 and K_0 fulfill that $|K_1| > |K_0|$, as demonstrated in [92].
- The real part of the refractive index obtained from the absorption must fulfill the Kramer-Kronig relation as

$$n_s(\omega) = n_s(\infty) + \frac{c_0}{\pi} \int_0^\infty \frac{\alpha}{\Omega^2 - \omega^2} d\Omega \quad (6.8)$$

	Diesel (B0)	Biodiesel (B100)
K_0 [ps ⁻²]	188.97 ± 1.44	31.28 ± 0.40
K_1 [ps ⁻²]	457.50 ± 3.51	191.40 ± 2.73
γ [ps ⁻¹]	23.17 ± 0.22	19.17 ± 0.29
D_t	0.01056 ± 0.00024	0.17443 ± 0.00607
g [cm ⁻¹ /ps ⁻¹]	n. a.	0.5073 ± 0.038
D_t^{ap} [0.2-3.5 THz]	0.0052	0.1873

Table 6.1.: Fit model parameters of B0 and B100 from 4500 waveforms. The error bars correspond to the 95% confidence interval.

The adequacy of the models to predict the refractive index based on applying the Kramer-Konig relation is shown in fig. 6.3. It shows the measured refractive index

of B0 and B100 according to eq. (4.10) in comparison to the refractive index arising from the Kramer-Konig relation applied to the theoretical models given in eqs. (6.6) and (6.7) for the parameters listed in table 6.1. With the offset being the only parameter, determined by correcting the offset at 2 THz as $n_s(\infty) = 1.452$ and $n_s(\infty) = 1.460$, there exists an excellent agreement between the models and the measured refractive index.

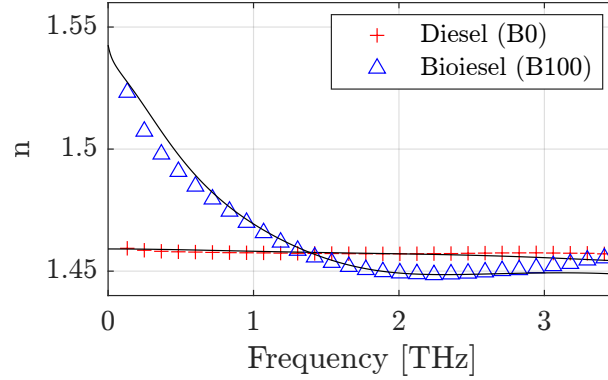


Figure 6.3.: Refractive index of the B0 and B100 samples. The solid lines corresponds to the refractive index calculated from the fit models of the absorption coefficient given in table 4.1 after applying the Kramers-Konig relation from eq. (6.8), where the $n_s(\infty)$ has been used to adjust the offset at 2 THz (© 2021 IEEE).

6.4. Broadband blend characterization

After having determined the models for the two basic constituents of the blends (B0 and B100), three different approaches are used to determine the biodiesel content of the blends. The first two methods are based on a linear combination of the models for B0 and B100 described by eqs. (6.6) and (6.7), with the second one using simplified models that accommodate single-shot data with lower SNR and, therefore, real time characterization ability at cost of lower bandwidth (1.75 THz). The third method consists of a simplified model based on characterizing the blend based on the maximum observed dispersion, i.e., on the difference between the maximum and the minimum value of the refractive index.

6.4.1. Linear combination model of blends

The model for absorption coefficients of blends is defined as a linear combinations between the absorption coefficient models of pure petroleum diesel from eq. (6.6), $\alpha_D(\omega)$, and pure biodiesel from eq. (6.7), $\alpha_{BD}(\omega)$:

$$\alpha_{Bk}(\omega) = k \cdot \alpha_{BD}(\omega) + (1 - k) \cdot \alpha_D(\omega), \quad (6.9)$$

6. Broadband characterization of biodiesel blends

where $\alpha_{Bk}(\omega)$ is the model absorption coefficient of the blend Bk between B0 (100% diesel, $k = 0$) and B100 (100% biodiesel, $k = 1$). The mixing ratio k is obtained by minimizing the error between the model and the measured absorption coefficient $\tilde{\alpha}_{Bx}$. Using the root-mean-squares over the discretized spectrum with N_ω points (ω_i), the ratio is calculated as:

$$k = \arg \min_{k \in [0,1]} \left[\sqrt{\frac{1}{N_\omega} \sum_{i=0}^{N_\omega} (\alpha_{Bk}(\omega_i) - \tilde{\alpha}_{Bx}(\omega_i))^2} \right] \quad (6.10)$$

The results can be found in fig. 6.4. The absorption of all samples are well modeled using this approach and the k -value is very close to the nominal value representing the mixing ratio, as it can be seen in fig. 6.5, that also shows that the committed error is below 3% ($\Delta k = k_{fit} - k_{nom} \leq 3\%$). The small error could even be assigned to errors occurring during sample preparation, performed by hand with graduated pipettes.

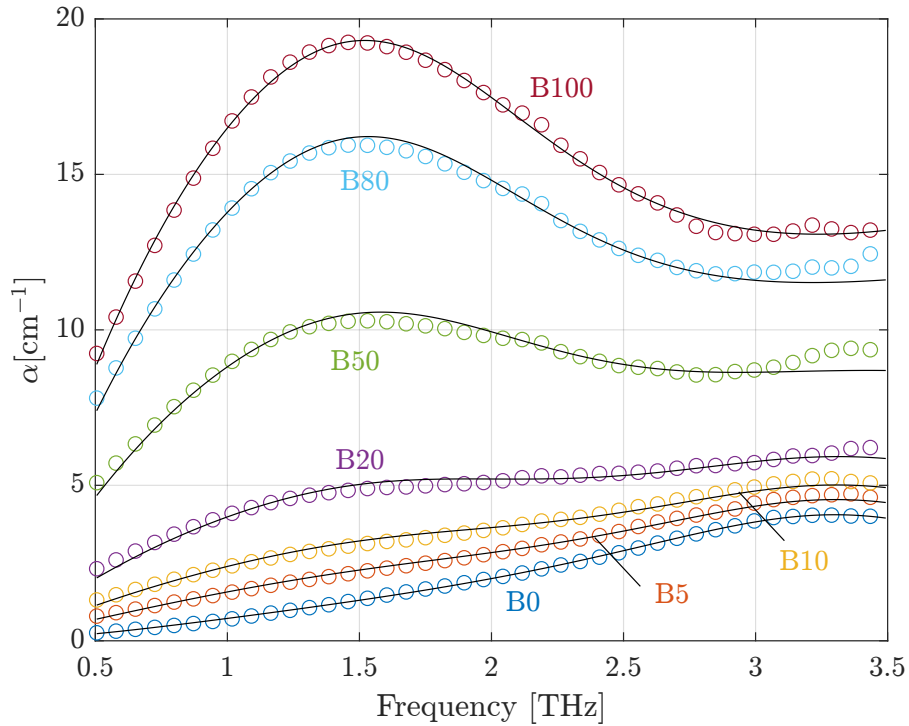


Figure 6.4.: Measured absorption coefficient of all samples (circles) and fit (solid lines) from the model given by eqs. (6.9) and (6.10) (© 2021 IEEE).

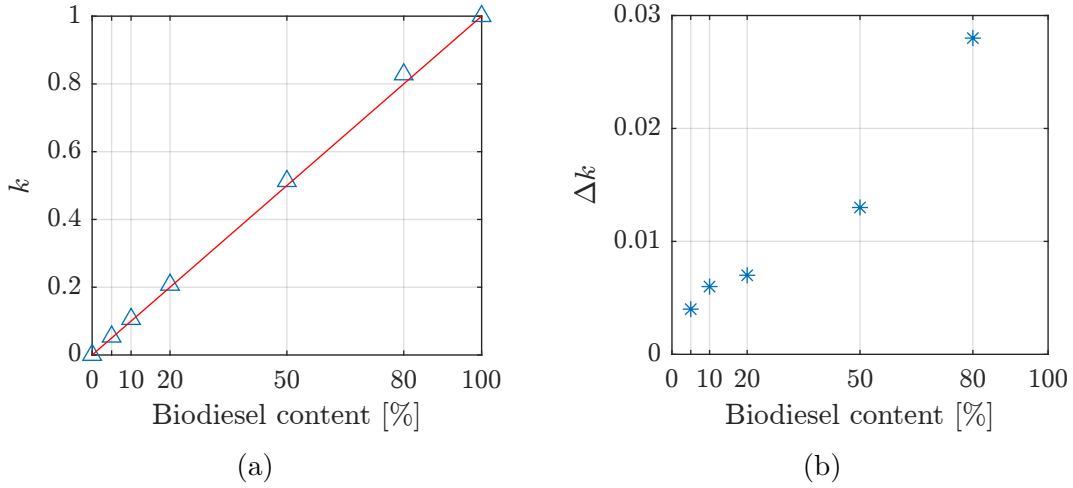


Figure 6.5.: (a) Blend characterization from the linear combination model given by eqs. (6.9) and (6.10). (b) Deviation of the fit from the nominal value (© 2021 IEEE).

6.4.2. Real-time characterization

Single shot data, recorded with the THz- TDS system at a speed of 9 traces/s is shown in fig. 6.1a and fig. 6.1b. With this configuration, in which the data is not averaged over multiple waveforms, the SNR decreases and the bandwidth is limited to 2 THz.

With a range of 2 THz, the model for the diesel loses some of the features that makes the non-polar model to quickly converge (e.g. the 3.2 THz peak is out of range). For sufficiently low frequencies eq. (6.6) can be approximated to a quadratic absorption model as

$$\alpha_D(\omega) \approx \frac{D_t}{n_s(\omega)c_0} \frac{K_1}{\gamma K_0} \omega^2 = \frac{K_D}{n_s(\omega)c_0} \omega^2, \quad (6.11)$$

where $K_D = (D_t K_1)/(\gamma K_0)$, expressed in ps, is now the only parameter of the model.

Within the 2 THz range, the absorption still features a peak and the model from (6.7) converges. The measured absorption coefficients and fit curves, obtained for the interval 0.5-1.75 THz, are shown in fig. 6.6 for both samples.

With a similar approach to that applied previously for 4500 waveforms, described in eqs. (6.9) and (6.10), it is also possible to obtain the biodiesel content of the blends by fitting the data to a linear combination of the constitues. The value of the mixing ratio k and the deviation from the nominal value Δk are shown in fig. 6.7. There still exists an excellent agreement between the nominal and the fitted mixing ratio, with a deviation below 2%.

6. Broadband characterization of biodiesel blends

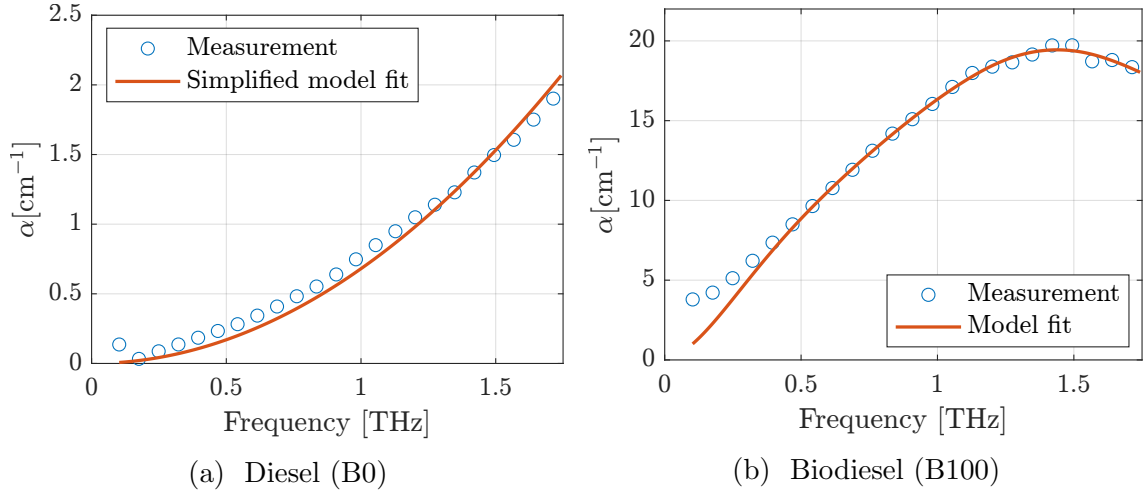


Figure 6.6.: Absorption coefficient of petroleum diesel (B0) and (B100) and the fit to the model from eqs. (6.7) and (6.11) using single-shot data (© 2021 IEEE).

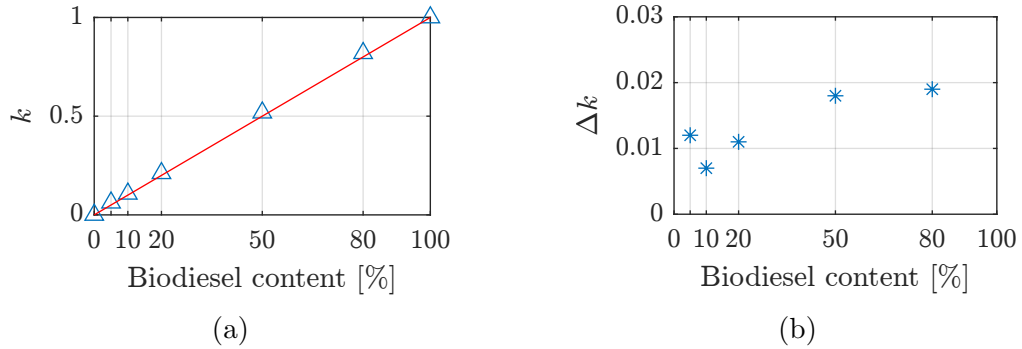


Figure 6.7.: (a) Blend characterization from the linear combination model given by eqs. (6.9) and (6.10) using the single-shot data. (b) Deviation of the fit from the nominal value (© 2021 IEEE).

6.4.3. Biodiesel content determination by maximum dispersion

Figure 6.3 showed a clear distinction in terms of dispersion between B0 and B100, with the latter being strongly more dispersive. Dispersion can therefore be an alternative parameter for the determination and characterization of biodiesel content. Figure 6.8a depicts the refractive index of all blends, showing that the refractive index of pure diesel is almost constant. It becomes more frequency-dependent as the biodiesel content increases within the measurement interval of 0.2-3 THz.

Dispersion, while usually defined by the slope of the refractive index vs. wavelength, is here approximated by the difference between the maximum and minimum measured permittivity ($\epsilon_{max} - \epsilon_{min}$). This permittivity difference is also directly related to the fit model parameter D_t , as shown in table 6.1, providing the approximation denoted as D_t^{ap} .

Figure 6.8b shows the maximum variation of the permittivity for each sample in two different frequency ranges that represent two different system capabilities (i.e. with different frequency spans). It shows that dispersion is an excellent characteristic to identify the biodiesel content, as it increases with the biodiesel (FAME) content almost linearly, except for the highest concentrations.

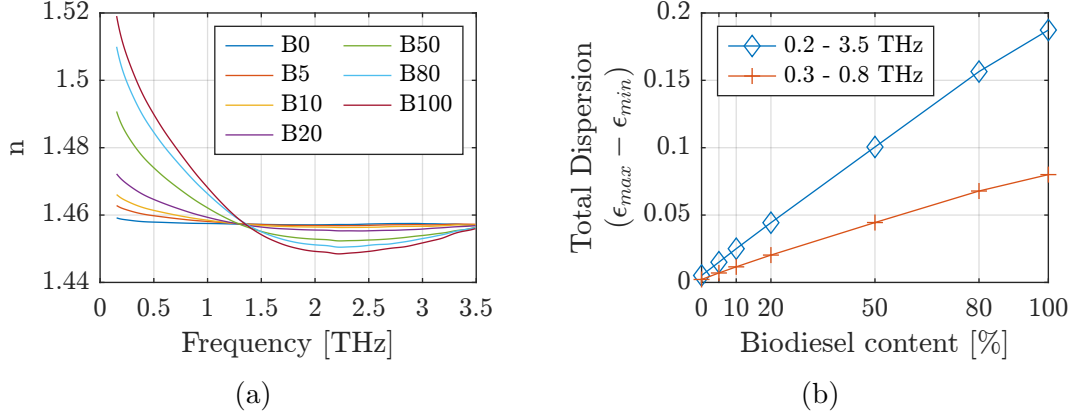


Figure 6.8.: (a) Refractive index of all samples. (b) Blend characterization using the maximum dispersion at two predefined frequency spans (© 2021 IEEE).

6.5. Conclusions and Further Work

This chapter has demonstrated that it is possible to characterize the biodiesel content in diesel blends based on the linear combination of absorption models of the two components. The model fit to the biodiesel corresponds to a non-polar liquid, while for biodiesel a linearly increasing absorption component had to be added to the model, corresponding to either the polarity of FAME molecule ester-group or some polar by-products such as methanol or glycol. The linear combination model has shown an excellent discernability among all 5 intermediate blends. This approach is capable of real-time data acquisition (with 9 traces/s), modifying only the model for the diesel (BO) in order to fit the data below 1.75 THz. It has also been demonstrated that biodiesel introduces a distinctive change of the dispersion, which can also be used as a simplified broadband characteristic to determine biodiesel concentration.

A further evaluation of the methods can be carried out using training and evaluation data sets that will provide a quantification of the correlation. The identification and quantification of individual by-products (e.g. methanol, glycol, water, etc.) that are potentially present in biodiesel might be a useful quality and process control technology based on the methods described, precisely discerning among the different components and contaminants and its quantity. Relying on broadband characteristics that, in absence of narrow features, provides a unique fingerprint for each of them which is discernible with THz-TDS.

7. Conclusions and summary

The first part of this thesis (chapters 2 and 3) was focused on the development, fabrication and characterization of FB-p-i-n diode as a THz source. The source was designed towards the implementation of a continuous-wave photonic VNA (CW-PVNA), with an increased optical to THz conversion efficiency required in table-top, two-port systems that features some tens of mW of optical power levels.

It has been shown that the passive optical waveguide (POW)-coupled photomixer outperforms a similar top-illuminated sample by a factor of 7 in terms of optical coupling efficiency. The FB-p-i-n diode has shown a comparatively better characteristics at high frequency than a n-i-pn-i-p superlattice photomixer as a comparison to the state-of-the-art. This feature, combined with an improved thermal conductivity, is a promising result that may lead towards overcoming some limitations found with n-i-pn-i-p superlattice photomixers that limited their maximum THz power. Furthermore, the implementation of the POW coupling is much easier with one-period diodes, as opposed to the two- or three-period n-i-pn-in-p superlattice photomixers.

In future work, the emitted THz power needs to be improved by a redesign of the p-i-n structure in order to surpass the state-of-the-art in terms of absolute power, which currently is about 15-20 dB better. Several improvements have been identified that might result in an overall better outcome of the THz power. They include redesigns of the diode heterostructure (e. g. changing p-type dopant from Zn to C), changes on the growing process (e. g. MBE in stead of CVD will provide a better control over the material characteristics), improvements on the fabrication process for better reproducibility of the overall fabrication and improvements of the experimental set-up. A more detailed description of these points was presented in section 3.3.

The second part of the thesis focused on Terahertz (THz)-time-domain spectroscopy (THz-TDS) of liquids. In Chapter 4, the THz-TDS technique and the different sources of error have been described and analyzed. Special attention has been paid to typical assumptions and approximations, providing a detailed theoretical description and analysis of the systematic errors that they produce. Using data from own published work (references [74, 78]), a detailed analysis of the error was performed in chapter 5. Grouping different sets of measurements allowed to conclude that the phase measurement (i.e the refractive index) is much more robust against errors and perturbations than the absorption coefficient, reaching the resolution limit of the system when the dimensions of the cuvettes are known. Furthermore, the small absorption or refractive index contrast of mixtures has demonstrated the need for cautious preparation of these kind of samples. Using cuvettes with imprecisely known thickness (but with a estimated standard deviation), it has been also

7. Conclusions and summary

possible to prove the adequacy of the theoretical models of the error sources, as the measured standard deviation of the refractive index matched the theoretical standard deviation given the experimentally measured error of the cuvette thickness. A detailed analysis of the different errors experimentally determined and conclusions from this chapter were shown in section 5.7.

In chapter 6, biodiesel and petroleum-diesel blends were characterized using a new approach based on broadband information of the absorption coefficient with THz-TDS. Using a non-polar liquid absorption model for diesel and a slightly modified model for biodiesel that also accommodates the existence of some polar components, it has been possible to identify the biodiesel content in mixtures by the fit to the best linear combination of the two models. The deviation from the nominal mixing ratio was below 3% i.e. of the order of the error due to sample preparation. The approach also works under real-time data acquisition conditions (9 traces/s), with just a modification of the biodiesel model to better fit data below 1.75 THz. A final approach that identifies the mixtures by investigating the dispersion has been also proven to give a precise and almost linear determination of the biodiesel content. The use of broadband information, even in the absence of narrow features allows for an improved robustness with respect to methods that rely on individual frequencies only, as it identifies the components by the frequency-dependent characteristics of their absorption coefficient, so that systematic and random errors with different frequency characteristics are easier to identify and to correct for. In the future, the identification and quantification of by-products and potential contaminants of biodiesel blends (e.g. water, methanol, glycol, etc.) might be useful for quality and process control technology. As the method presented in this thesis relies on broadband characteristics that provides a unique fingerprint with THz-TDS for each of them, detailed content characterization should be possible.

A. Dry etching process description and calibration

A.1. III-V semiconductor etching process

For the etching of the InP, InGaAs and InGaAsP compounds, a chlorine-based plasma-assisted reactive ion etching (RIE) process was used. It was performed using a Sentech SI 500 inductive coupled plasma - RIE (ICP-RIE) system in Duisburg. The exact parameters of the process are depicted in table A.1.

Gases	Flow	Pressure	P _{ICP}	P _{RF}	Temperature
Cl ₂ :N ₂	4 : 26 sccm	0.6 Pa	300 W	25 W	300 °C

Table A.1.: III-V semiconductor etching recipe.

Due to the low volatility of the indium chloride products of the reaction, it is necessary to increase the temperature of the sample during the etching process in order to obtain a good anisotropy (i.e. verticality of the etching process) as well as a low surface roughness. In this work, a temperature of 170 °C was used. The sample is mounted on top of a Si wafer, placed on top of a loading plate that heats it from the back. The etching rate of InP and InGaAs saturates at around 200 °C for Cl₂:N₂ and reduces beyond this temperature. This is due to the desorption of the active radicals, which are no longer able to reach the surface [98].

The etch rate increases with the Cl₂ ratio. The exact flow rate of the gases is not relevant as long as it is enough to keep the target pressure. The dependence of etching speed on the chlorine ratio is shown in fig. A.1.

The process from table A.1 was calibrated using a s.i.-Fe:InP wafer with different test runs separated by several months. Two models were considered and fitted into the data. The first fit is a linear model that provides good estimations of the etched InP with long processing times, but fails for shorter times (below 1 minute). When smaller depths (i.e. lower times) are required, a rational model is used. This is specially useful for the waveguide etch process in which the goal depth on n-InP is 100 nm. The results of a calibration using two sets of data are shown in fig. A.2.

The heterostructure composition, with In(Al)GaAs and quaternary InGaAsP layers and the different doping levels of the InP, makes the s.i.-InP calibration insufficient. It is important to calibrate the speed at which the SiN mask is etched in order to precisely monitor the etch depth during the process. As the mask has always the same composition, the estimation of the etch depth is independent from

A. Dry etching process description and calibration

the heterostructure. The slow etching speed, around 5 times lower than s.i. InP, makes it more difficult to calibrate with higher variations observed, specially for low time processes. The results are shown in fig. A.3.

A.2. SiN etching process

A dry-etching plasma-assisted process based on $\text{CF}_4:\text{O}_2$ is used to pattern the SiN mask and remove it after the etching was completed. It is also used to create the passivation SiN layer and the anti-reflection coating. This process was carried out at 24°C , which was the minimum stable temperature that the system was able to sustain. The sample was glued using pump-oil to a p-type Si wafer in order to improve the thermal contact and get a more constant etch rate. The etch rate, extracted from the linear fit, was between 326 and 372 nm/min, with delay times of 18 and 3s, respectively. The data from different test runs and points (corresponding to individual measurements during actual sample processing runs), are depicted in fig. A.4. The variability of the delay at the start of the process is the main source of error, which is likely produced by impedance matching of the RF generator and the pressure stabilization.

Gases	Flow	Pressure	P_{ICP}	P_{RF}	Temperature
$\text{CF}_4:\text{O}_2$	36 : 6 sccm	10 Pa	Off	120 W	24°C

Table A.2.: $\text{CF}_4:\text{O}_2$ process for SiN etching. Used for SiN mask shaping, and isolation layer formation.

A.3. Other recipes and summary

A.3.1. Photoresist removal

After every SiN mask patterning using $\text{CF}_4:\text{O}_2$, a thin layer of cross-linked photoresist, insoluble in acetone, was still present at the end of the process after the acetone and isopropanol dip. It is usually easy to identify it under a microscope as a thin veil with cracks. The thickness is usually on the limit of what can be measured with common profilers, in the range of 50 to 100 nm, although it might bend and fold forming thicker layers. During this thesis, it occurred with all the positive photoresist, including those more suitable for dry-etching. The best solution to remove this cross-linked photoresist was an O_2 plasma etch process. The details of this process is shown in table A.3.

The processing time to remove the cross-linked photoresist was found at 100 s. It is important to keep the time as short as possible to avoid physical damage on the sample surface.

Gases	Flow	Pressure	P_{ICP}	P_{RF}	Temperature
O ₂	25 sccm	1 Pa	300 W	25 W	24 °C

Table A.3.: O₂ plasma process for photoresist ashing.

A.3.2. Cleaning process

The cleaning recipe consists of an Ar and O₂ plasma process given by the manufacturer. It was run before every new process that required of any different gas.

A.3.3. Summary

Table A.4 summarizes all etch recipes used. Some processes, like the SiN etching with CF₄:O₂ were performed with two separate systems in Duisburg and Darmstadt.

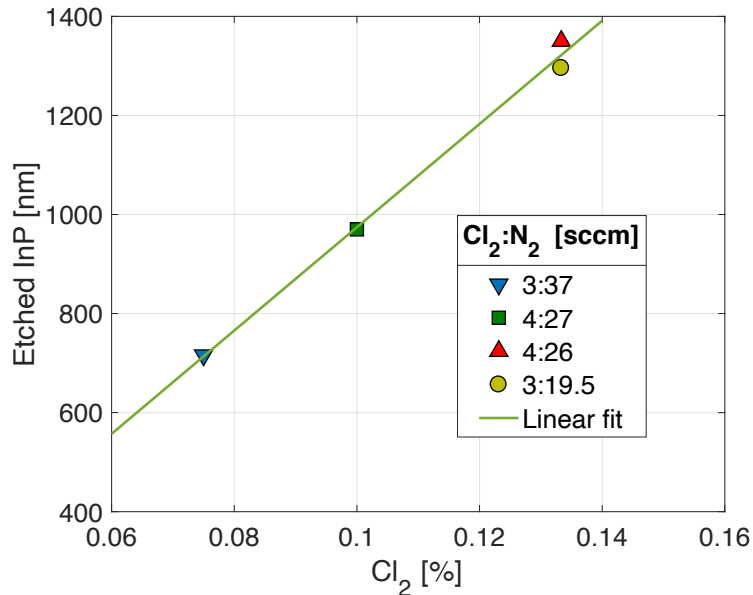


Figure A.1.: Etch rate of s.i. InP for different Cl₂ ratios. All processes were run for 5 min and performed with all other parameters unaltered using a coil power of 300 W, a RF power of 25 W, a pressure of 0.6 Pa and a temperature of 170 °C. The points with 3:26 and 3:19.5 sccm correspond to the same Cl₂ ratio.

A. Dry etching process description and calibration

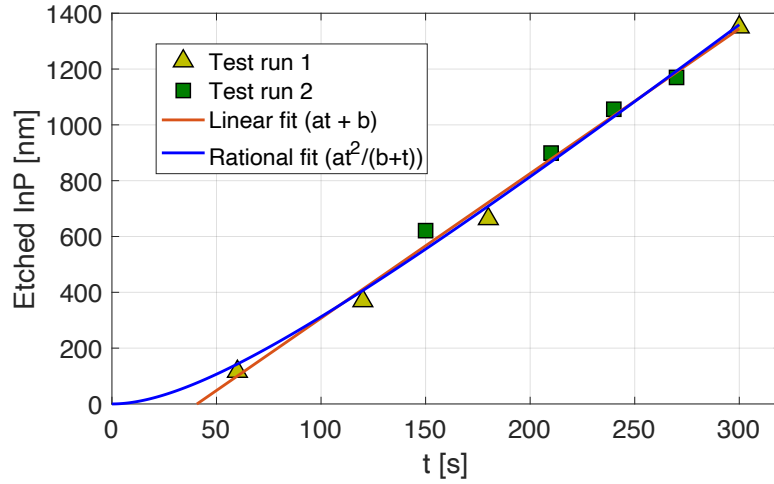


Figure A.2.: Etch calibration of s.i. InP. The two test runs were spaced around four months. A linear model and a rational model are fitted. The process is described in table A.1

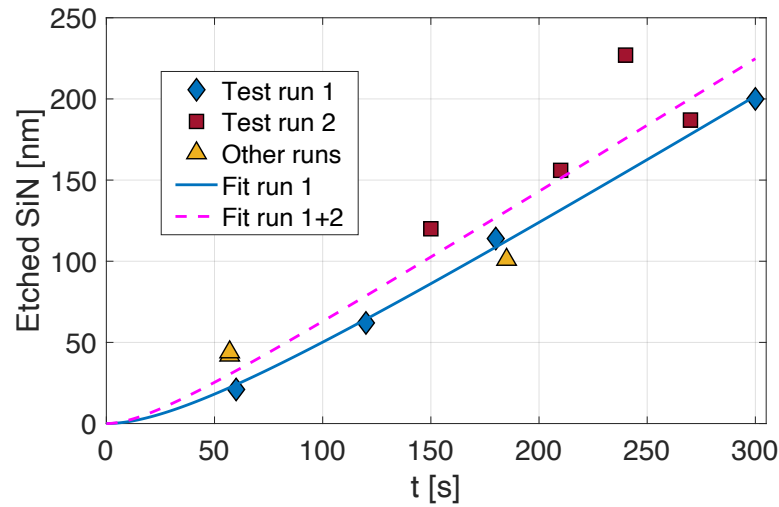


Figure A.3.: Etch calibration of SiN. Two independent test runs, spaced four months in time are depicted. The yellow triangle show other independent process runs during actual sample processing. The fit curve is a rational function of the form $at^2/(b+t)$. The process is described in table A.1

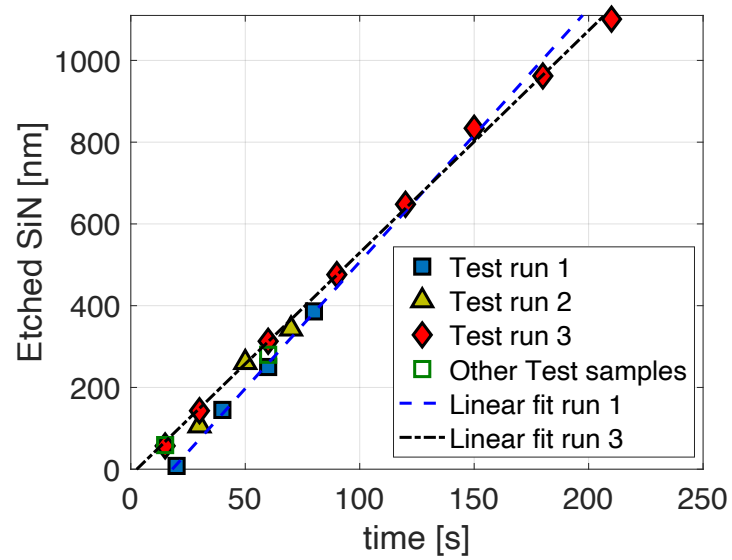


Figure A.4.: Etch calibration of SiN with $\text{CF}_4:\text{O}_2$ plasma. Linear fits to two of the runs are shown.

Description	Gases	Flow	Pressure	P _{ICP}	P _{RF}	Temperature
III-V semiconductor etching (DU)	Cl ₂ :N ₂	4:26 sccm	0.6 Pa	300 W	25 W	300 °C
SiN etching (DU)	CF ₄ :O ₂	36:6 sccm	10 Pa	Off	120 W	24 °C
SiN etching (DA)	CF ₄ :O ₂	45:5 sccm	75 mTorr	N. A.	120 W	20 °C
PR etching (DU)	O ₂	25 sccm	1 Pa	300 W	25 W	24 °C
PR etching (DA)	O ₂	100 sccm	150 mTorr	N. A.	200 W	20 °C

Table A.4.: Summary of all the plasma assisted dry etching processes used in this work. It includes the clean rooms where they were performed, denoted as DA for Darmstadt and DU for Duisburg. N. A denotes not applicable, as the system used in Darmstadt was a capacitive RIE and, thus, it has only a RF generator.

B. Optical constants of the S.I.-Fe:InP substrate

The following data were obtained using a commercial THz-TDS system from Menlo Systems GmbH. The measured thickness, using also with the THz-TDS data, was 0.50593 mm.

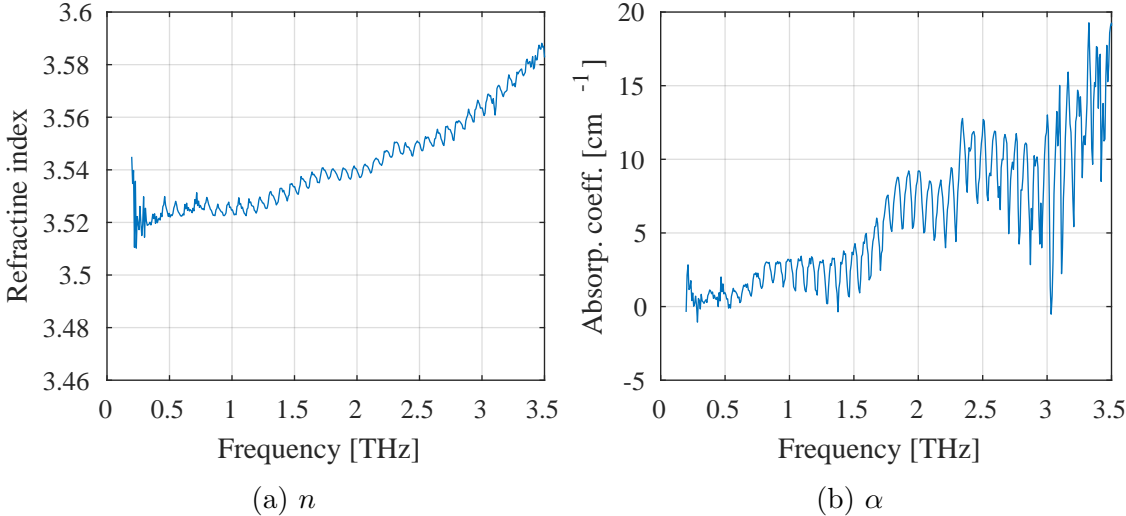


Figure B.1.: Optical constants of semi-insulating (s.i.) Fe:InP

C. Error normalization

Assuming that predominant error is due to thickness variation (including resolution and rotation of the cuvette), the error will then depend on the value of the optical constant. Therefore, the data from different samples are pooled in order to improve the error estimation, as in section 5.6, to estimate the statistics of a measurement round that comprises different sample, a normalization must be performed over the error for each sample.

Error normalization of the refractive index

The error of the refractive index for a thickness error Δd is shown to be proportional to $(n_s(\omega) - 1)$ in eq. (4.19). Defining the normalized error Δn_{norm} as:

$$\Delta n_{norm}(\omega) = (n_{ref}(\omega) - 1) \frac{\Delta d}{d_s} = f_n(\omega) \Delta n(\omega), \quad (\text{C.1})$$

where d_s is the sample thickness and $f_n(\omega)$ is the normalization factor, which is calculated from eq. (C.1) as:

$$f_n(\omega) = \frac{\Delta n_{norm}(\omega)}{\Delta n(\omega)} = \frac{n_{ref}(\omega) - 1}{n_s(\omega) - 1} \quad (\text{C.2})$$

Equation (C.1) is, therefore:

$$\Delta n_{norm}(\omega) = \Delta n(\omega) \frac{n_{ref} - 1}{n_s(\omega) - 1} \quad (\text{C.3})$$

In this thesis, particularly in chapter 5, where the error analysis is performed, the small difference in refractive index between all samples makes this approximation negligible. In particular, the maximum difference identified is between 1.466 and 1.462 for NA000 and GA120 samples, respectively (see fig. 5.7c). That implies a change of less than 1% of the estimated error.

Error normalization of the absorption coefficient

Symmetrically, the normalized error for the absorption coefficient can be obtained from eq. (4.20) as:

$$\Delta \alpha_{norm}(\omega) = \Delta \alpha f_\alpha(\omega) = \Delta \alpha \frac{\alpha_{ref}(\omega) \Delta d - 2 \ln R(\omega, n_{ref}(\omega))}{\alpha(\omega) \Delta d - 2 \ln R(\omega, n_s(\omega))}, \quad (\text{C.4})$$

C. Error normalization

where

$$R(\omega, n) = \frac{(n(\omega) + n_w)^2 (n(\omega) + \Delta n(\omega))}{(n(\omega) + \Delta n(\omega) + n_w)^2 n(\omega)}, \quad (\text{C.5})$$

with $\Delta n(\omega) = -(n(\omega) - 1)\Delta d/(d_s + \Delta d)$.

For most cases, the term $\ln R(\omega)$ is much smaller than $\alpha \cdot \Delta d$ and eq. (C.4) simplifies to

$$\Delta\alpha_{norm} = \Delta\alpha(\omega) \frac{\alpha_{ref}(\omega)}{\alpha(\omega)} \quad (\text{C.6})$$

Bibliography

- [1] Virginia diodes. <https://vadiodes.com/en/products/vector-network-analyzer-extension-modules>. Accessed: 12-01-2021.
- [2] Thorsten Göbel, Dennis Stanze, Björn Globisch, Roman J. B. Dietz, Helmut Roehle, and Martin Schell. Telecom technology based continuous wave terahertz photomixing system with 105 decibel signal-to-noise ratio and 3.5 terahertz bandwidth. *Opt. Lett.*, 38(20):4197–4199, Oct 2013.
- [3] Sascha Preu. Components towards a photonics aided thz vector network analyzer. In *Optical Fiber Communication Conference*, page W4K.4. Optical Society of America, 2016.
- [4] Anselm J. Deninger, A. Roggenbuck, S. Schindler, and S. Preu. 2.75 THz tuning with a triple-DFB laser system at 1550 nm and InGaAs photomixers. *Journal of Infrared, Millimeter, and Terahertz Waves*, 36(3):269–277, March 2015.
- [5] Angel Ruben Criado, Cristina De Dios, Gottfried Dohler, Sascha Preu, Stefan Malzer, Sebastian Bauerschmidt, H. Lu, A.C. Gossard, and P. Acedo. Ultra-narrow linewidth CW sub-THz generation using GS based OFCG and n-i-pn-i-p superlattice photomixers. *Electronics Letters*, 48:1425, 10 2012.
- [6] Mohammad Tanvir Haidar, Sascha Preu, Sujoy Paul, Christian Gierl, Julijan Cesar, Ali Emsia, and Franko Küppers. Widely tunable telecom MEMS-VCSEL for terahertz photomixing. *Optics Letters*, 40(19):4428, October 2015.
- [7] Hiroshi Ito, Fumito Nakajima, Tomofumi Furuta, and Tadao Ishibashi. Continuous THz-wave generation using antenna-integrated uni-travelling-carrier photodiodes. *Semiconductor Science and Technology*, 20(7):S191–S198, jun 2005.
- [8] S. Preu, F. H. Renner, S. Malzer, G. H. Döhler, L. J. Wang, M. Hanson, A. C. Gossard, T. L. J. Wilkinson, and E. R. Brown. Efficient terahertz emission from ballistic transport enhanced n-i-p-n-i-p superlattice photomixers. *Applied Physics Letters*, 90(21):212115, 2007.
- [9] Guillermo Carpintero, Luis Enrique Garcia-Muñoz, Hans L. Hartnagel, Sascha Preu, and Antti V. Räissänen. *Semiconductor Terahertz Technology. Devices and Systems at Room Temperature Operation*. Wiley, 2015.

Bibliography

- [10] Dennis Stanze, Anselm Deninger, Axel Roggenbuck, Stephanie Schindler, Michael Schlak, and Bernd Sartorius. Compact CW Terahertz Spectrometer Pumped at 1.5 μm Wavelength. *Journal of Infrared, Millimeter, and Terahertz Waves*, 32(2):225–232, February 2011.
- [11] Vitaly Rymanov, Andreas Stöhr, Sebastian Dülme, and Tolga Tekin. Triple transit region photodiodes (TTR-PDs) providing high millimeter wave output power. *Opt. Express*, 22(7):7550–7558, Apr 2014.
- [12] Anuar de Jesus Fernandez Olvera, Axel Roggenbuck, Katja Dutzi, Nico Vieweg, Hong Lu, Arthur C. Gossard, and Sascha Preu. International System of Units (SI) traceable noise-equivalent power and responsivity characterization of continuous wave ErAs:InGaAs photoconductive terahertz detectors. *Photonics*, 6(1), January 2020.
- [13] A.D.J. Fernandez Olvera, H. Lu, A. C. Gossard, and S. Preu. Continuous-wave 1550 nm operated terahertz system using ErAs:In(Al)GaAs photo-conductors with 52 dB dynamic range at 1 THz. *Opt. Express*, 25(23):29492–29500, Nov 2017.
- [14] Alejandro Rivera-Lavado, Sascha Preu, Luis Enrique García-Munoz, Andrey Generalov, Javier Montero-de Paz, Gottfried Döhler, Dmitri Lioubtchenko, Mario Méndez-Aller, Florian Sedlmeir, Martin Schneidreit, Harald G. L. Schwefel, Stefan Malzer, Daniel Segovia-Vargas, and Antti V. Raisanen. Dielectric Rod Waveguide Antenna as THz Emitter for Photomixing Devices. *IEEE Transactions on Antennas and Propagation*, 63(3):882–890, March 2015.
- [15] S. M. Sze. *Physics of Semiconductor Devices*. Wiley, 3 edition, 2005.
- [16] M. S. Alam, M. S. Rahman, M. R. Islam, A. G. Bhuiyan, and M. Yamada. Refractive index, absorption coefficient, and photoelastic constant: Key parameters of InGaAs material relevant to InGaAs-Based device performance. In *2007 IEEE 19th International Conference on Indium Phosphide Related Materials*, pages 343–346, May 2007.
- [17] Constantine A Balanis. *Antenna theory: analysis and design*. Wiley-Interscience, 2005.
- [18] Uttam Nandi, J. Norman, A. Gossard, H. Lu, and Sascha Preu. 1550-nm driven ErAs:In(Al)GaAs photoconductor-based terahertz time domain system with 6.5 THz bandwidth. *Journal of Infrared, Millimeter, and Terahertz Waves*, 39:340–348, 02 2018.
- [19] U. Nandi, M. Mohammadi, H. Lu, J. Norman, A. C. Gossard, L. Alff, and S. Preu. Material properties and performance of ErAs:In(Al)GaAs photoconductors for 1550 nm laser operation. *Journal of Vacuum Science & Technology A*, 39(2):023407, 2021.

- [20] J. L. Hudgins, G. S. Simin, E. Santi, and M. A. Khan. An assessment of wide bandgap semiconductors for power devices. *IEEE Transactions on Power Electronics*, 18(3):907–914, May 2003.
- [21] H. Erlig, S. Wang, T. Azfar, A. Udupa, H. R. Fetterman, and D. C. Streit. LT-GaAs detector with 451 fs response at 1.55 μm via two-photon absorption. *Electronics Letters*, 35(2):173–174, Jan 1999.
- [22] Yi-Jen Chiu, S. Z. Zhang, S. B. Fleischer, J. E. Bowers, and U. K. Mishra. GaAs-based, 1.55 μm high speed, high saturation power, low-temperature grown GaAs p-i-n photodetector. *Electronics Letters*, 34(12):1253–1255, June 1998.
- [23] J. R. Middendorf and E. R. Brown. THz generation using extrinsic photoconductivity at 1550 nm. *Opt. Express*, 20(15):16504–16509, Jul 2012.
- [24] J. Mangeney, N. Chimot, L. Meignien, N. Zerounian, P. Crozat, K. Blary, J.F. Lampin, and P. Mounaix. Emission characteristics of ion-irradiated In_{0.53}Ga_{0.47}As based photoconductive antennas excited at 1.55 μm . *Opt. Express*, 15(14):8943–8950, Jul 2007.
- [25] H. Roehle, R. J. B. Dietz, H. J. Hensel, J. Böttcher, H. Künzel, D. Stanze, M. Schell, and B. Sartorius. Next generation 1.5 μm terahertz antennas: mesa-structuring of InGaAs/InAlAs photoconductive layers. *Opt. Express*, 18(3):2296–2301, Feb 2010.
- [26] Roman J. B. Dietz, Björn Globisch, Marina Gerhard, Ajanthkrishna Velauthapillai, Dennis Stanze, Helmut Roehle, Martin Koch, Thorsten Göbel, and Martin Schell. 64 μw pulsed terahertz emission from growth InGaAs/InAlAs heterostructures with separated photoconductive and trapping regions. *Applied Physics Letters*, 103(6):061103, 2013.
- [27] B. Globisch, R. J. B. Dietz, R. B. Kohlhaas, T. Göbel, M. Schell, D. Alcer, M. Semtsiv, and W. T. Masselink. Iron doped InGaAs: Competitive THz emitters and detectors fabricated from the same photoconductor. *Journal of Applied Physics*, 121(5):053102, 2017.
- [28] Sascha Preu, Martin Mittendorff, H. Lu, Heiko Weber, Stephan Winnerl, and A. Gossard. 1550 nm ErAs:In(Al)GaAs large area photoconductive emitters. *Applied Physics Letters*, 101, 09 2012.
- [29] S. Preu, G. H. Döhler, S. Malzer, L. J. Wang, and A. C. Gossard. Tunable, continuous-wave terahertz photomixer sources and applications. *Journal of Applied Physics*, 109(6):061301, 2011.
- [30] C Müller-Landau, S Malzer, H B Weber, G H Döhler, S Winnerl, P Burke, A C Gossard, and S Preu. Terahertz generation with ballistic photodiodes

- under pulsed operation. *Semiconductor Science and Technology*, 33(11):114015, November 2018.
- [31] H. Ito, S. Kodama, Y. Muramoto, T. Furuta, T. Nagatsuma, and T. Ishibashi. High-speed and high-output InP-InGaAs unitraveling-carrier photodiodes. *IEEE Journal of Selected Topics in Quantum Electronics*, 10(4):709–727, July 2004.
- [32] G Döhler, F Renner, O Klar, M Eckardt, A Schwanhäußer, Stefan Malzer, D Driscoll, Maxwell Hanson, AC Gossard, G Loata, T Löffler, and H Roskos. THz-photomixer based on quasi-ballistic transport. *Semiconductor Science and Technology*, 20:178–190, 06 2005.
- [33] Peng Lu. Hybride und monolithische Integration von passiven optischen Wellenleitern zur optischen Kopplung mit Terahertz-Photodioden. Master’s thesis, Universität Duisburg-Essen, Germany, 2016.
- [34] R. E. Nahory, M. A. Pollack, W. D. Johnston, and R. L. Barns. Band gap versus composition and demonstration of Vegard’s law for InGaAsP lattice matched to InP. *Applied Physics Letters*, 33(7):659–661, 1978.
- [35] Eric W. Van Stryland, M. A. Woodall, H. Vanherzeele, and M. J. Soileau. Energy band-gap dependence of two-photon absorption. *Opt. Lett.*, 10(10):490–492, Oct 1985.
- [36] Robert G Hunsperger. *Integrated Optics : Theory and Technology*. 6th edition, 2009.
- [37] K. Tappura. Electrical and optical properties of GaInAsP grown by gas-source molecular beam epitaxy. *Journal of Applied Physics*, 74(7):4565–4570, October 1993.
- [38] T. P. Pearsall, editor. *GaInAsP alloy semiconductors*. Wiley, Chichester [West Sussex] ; New York, 1982.
- [39] Stefan Krämer. *Geordnetes InGaAsP. Grundsätzliche Untersuchungen und elektro-optische Anwendungen*. PhD thesis, Friedrich-Alexander-Universität Erlangen Nürnberg, 2005.
- [40] Sasson R. Somekh. *Theory, fabrication and performance of some integrated optical devices*. PhD thesis, California Institute of Technology, 1973.
- [41] C. Yeh and F. Shimabukuro. *The Essence of Dielectric Waveguides*. Springer US, 2008.
- [42] Longfei Shen, René van Veldhoven, Yuqing Jiao, Victor Dolores Calzadilla, Jos van der Tol, Gunther Roelkens, and Meint Smit. Ohmic contacts with ultra-low optical loss on heavily doped n-type ingaas and ingaasp for inp-based photonic membranes. *IEEE Photonics Journal*, 8, 2016.

- [43] Andrei V Ivanov, V D Kurnosov, K V Kurnosov, Aleksandr A Marmalyuk, V I Romantsevich, Yu L Ryaboshtan, and Roman V Chernov. Refractive indices of solid AlGaInAs solutions. *Quantum Electronics*, 37(6):545–548, jun 2007.
- [44] D. Olego, T. Y. Chang, E. Silberg, E. A. Caridi, and A. Pinczuk. Compositional dependence of band-gap energy and conduction-band effective mass of inAlGaAs lattice matched to InP. *Applied Physics Letters*, 41(5):476–478, 1982.
- [45] L. Chusseau, P. Martin, C. Brasseur, C. Alibert, and P.J.L. Herve. Carrier-induced change due to doping in refractive index of InP: measurements at 1.3 and 1.5 μm . *Applied Physics Letters*, 69(20):3054–3056, 1996.
- [46] <https://ent-epitaxy.com/> (last visited 20-04-2020).
- [47] S. M. Sze and Ming-Kwei Lee. *Semiconductor Devices. Physics and Technology*. Wiley, 3 edition, 2006.
- [48] T-J. Kim and P. H. Holloway. Ohmic contacts to GaAs epitaxial layers. *Critical Reviews in Solid State and Materials Sciences*, 22(3):239–273, 1997.
- [49] D. H. van Dorp, D. Cuypers, S. Arnauts, A. Moussa, L. Rodriguez, and S. De Gendt. Wet chemical etching of InP for cleaning applications. *ECS Journal of Solid State Science and Technology*, 2(4):P190–P194, 2013.
- [50] A.G Baca, F. Ren, J. C. Zolper, R. D. Briggs, and S.J. Pearton. A survey of ohmic contacts to III-V compound semiconductors. *Thin Solid Films*, 308-309:599 – 606, 1997.
- [51] Sheng S. Li, editor. *Semiconductor Physical Electronics*. Springer New York, New York, NY, 2006.
- [52] J. Van Rudd and Daniel M. Mittleman. Influence of substrate-lens design in terahertz time-domain spectroscopy. *J. Opt. Soc. Am. B*, 19(2):319–329, Feb 2002.
- [53] Mario Méndez Aller, Hong Lu, Arthur C. Gossard, and Sascha Preu. Continuous-wave terahertz system with 50 dB dynamic range at 1 THz using a n-i-pn-i-p superlattice photomixer and an ErAs:InGaAs photoconductor operated at 1550 nm. In *2018 43rd International Conference on Infrared, Millimeter, and Terahertz Waves (IRMMW-THz)*, pages 1–2, 2018.
- [54] Hai-Bo Liu, Yunqing Chen, Glenn J. Bastiaans, and X.-C. Zhang. Detection and identification of explosive RDX by THz diffuse reflection spectroscopy. *Optics Express*, 14(1):415, 2006.
- [55] Tae-In Jeon and D. Grischkowsky. Characterization of optically dense, doped semiconductors by reflection THz time domain spectroscopy. *Appl. Phys. Lett.*, 72(23):3032–3034, June 1998.

Bibliography

- [56] Stefan Regensburger, Mahdad Mohammadi, Arslan A. Khawaja, Aldin Radetinac, Philipp Komissinskiy, Lambert Alff, and Sascha Preu. Optical Properties of Highly Conductive SrMoO₃ Oxide Thin Films in the THz Band and Beyond. *J. Infrared, Milli., THz Waves*, 41:1170 – 1180, June 2020.
- [57] R. Piesiewicz, C. Jansen, S. Wietzke, D. Mittleman, M. Koch, and T. Kürner. Properties of Building and Plastic Materials in the THz Range. *Int. J. Infrared, Milli. Waves*, 28(5):363–371, April 2007.
- [58] Ali Abdul-Munaim, M. Reuter, Oday Abdulmunem, Jan Balzer, Martin Koch, and Dennis Watson. Using Terahertz Time-Domain Spectroscopy to Discriminate among Water Contamination Levels in Diesel Engine Oil. *Trans. ASABE*, 59(3):795–801, June 2016.
- [59] Oday M. Abdulmunem, Ali Mazin Abdul-Munaim, Mario Méndez Aller, Sascha Preu, and Dennis G. Watson. THz-TDS for Detecting Glycol Contamination in Engine Oil. *Appl. Sci.*, 10(11):3738, May 2020.
- [60] Hui Zhao, Kun Zhao, and Rima Bao. Fuel property determination of biodiesel-diesel blends by terahertz spectrum. *Journal of Infrared, Millimeter, and Terahertz Waves*, 33(5):522–528, May 2012.
- [61] Hui Zhao, Kun Zhao, Lu Tian, Qing Miao, and Hao Ni. Optical property of biodiesel and its base stock in terahertz region. *Frontiers of Optoelectronics*, 5(2):214–217, Jun 2012.
- [62] José Vázquez-Cabo, Pedro Chamorro-Posada, Francisco Javier Fraile-Peláez, Óscar Rubiños López, José María López-Santos, and Pedro Martín-Ramos. Windowing of THz time-domain spectroscopy signals: A study based on lactose. *Optics Communications*, 366:386 – 396, 2016.
- [63] Ignacio H Lira and Wolfgang Wöger. The evaluation of standard uncertainty in the presence of limited resolution of indicating devices. *Measurement Science and Technology*, 8(4):441–443, 1997.
- [64] W. Withayachumnankul, H. Lin, S. P. Mickan, B. M. Fischer, and D. Abbott. Analysis of measurement uncertainty in THz-TDS. In Ali Serpengüzel, Gonçal Badenes, and Giancarlo C. Righini, editors, *Photonic Materials, Devices, and Applications II*, volume 6593, pages 604 – 621. International Society for Optics and Photonics, SPIE, 2007.
- [65] Withawat Withayachumnankul, Bernd M. Fischer, Hungyen Lin, and Derek Abbott. Uncertainty in terahertz time-domain spectroscopy measurement. *J. Opt. Soc. Am. B*, 25(6):1059–1072, 2008.
- [66] Withawat Withayachumnankul and M. Naftaly. Fundamentals of measurement in terahertz time-domain spectroscopy. *Journal of Infrared, Millimeter, and Terahertz Waves*, 35, 08 2013.

- [67] L. Duvillaret, F. Garet, and J. . Coutaz. A reliable method for extraction of material parameters in terahertz time-domain spectroscopy. *IEEE Journal of Selected Topics in Quantum Electronics*, 2(3):739–746, 1996.
- [68] Tingjun Hu, Ho Teng, Xuwei Luo, and Bin Chen. Impact of fuel injection on dilution of engine crankcase oil for turbocharged gasoline direct-injection engines. *SAE Int. J. Engines*, 8(3):1107–1116, apr 2015.
- [69] Matthew D. Brouwer, Lokesh A. Gupta, Farshid Sadeghi, Dimitrios Peroulis, and Douglas Adams. High temperature dynamic viscosity sensor for engine oil applications. *Sensors and Actuators A: Physical*, 173(1):102 – 107, 2012.
- [70] Bernhard Jakoby, Monika Scherer, Matthias Buskies, and Heinz Eisenschmid. An automotive engine oil viscosity sensor. *Sensors Journal, IEEE*, 3:562 – 568, 11 2003.
- [71] Y.-C Lin, Yu-Hsien Cho, Chin-Te Chiu, Ryan Clark, and Claudia Fajardo. Assessment of the properties of internal combustion engine lubricants using an onboard sensor. *Tribology and Lubrication Technology*, 68:40–49, 07 2012.
- [72] Alessandra Borin and Ronei J. Poppi. Application of mid infrared spectroscopy and iPLS for the quantification of contaminants in lubricating oil. *Vibrational Spectroscopy*, 37(1):27 – 32, 2005.
- [73] Ali Mazin Abdul-Munaim, Marco Reuter, Martin Koch, and Dennis G. Watson. Distinguishing gasoline engine oils of different viscosities using terahertz time-domain spectroscopy. 36.
- [74] Ali Mazin Abdul-Munaim, Mario Méndez Aller, Sascha Preu, and Dennis G. Watson. Discriminating gasoline fuel contamination in engine oil by terahertz time-domain spectroscopy. *Tribology International*, 119:123 – 130, 2018.
- [75] M. Naftaly and R. E. Miles. Terahertz time-domain spectroscopy for material characterization. *Proceedings of the IEEE*, 95(8):1658–1665, 2007.
- [76] Lu Tian, QingLi Zhou, Bin Jin, Kun Zhao, SongQing Zhao, YuLei Shi, and CunLin Zhang. Optical property and spectroscopy studies on the selected lubricating oil in the terahertz range. *Science in China Series G: Physics, Mechanics and Astronomy*, 52(12):1938–1943, December 2009.
- [77] Lu Tian, Kun Zhao, Qing-Li Zhou, Yu-Lei Shi, and Cun-Lin Zhang. Quantitative analysis for monitoring formulation of lubricating oil using terahertz time-domain transmission spectroscopy. *Chinese Physics Letters*, 29(4):043901, apr 2012.
- [78] Mario Méndez Aller, Ali Abdul-Munaim, Dennis Watson, and Sascha Preu. Error sources and distinctness of materials parameters obtained by THz-time

- domain spectroscopy using an example of oxidized engine oil. *Sensors*, 18(7), 2018.
- [79] A. Sydbom, A. Blomberg, S. Parnia, N. Stenfors, T. Sandström, and S-E. Dahlén. Health effects of diesel exhaust emissions. *Eur. Respir. J.*, 17(4):733–746, April 2001.
- [80] Zoran D. Ristovski, Branka Miljevic, Nicholas C. Surawski, Lidia Morawska, Kwun M. Fong, Felicia Goh, and Ian A. Yang. Respiratory health effects of diesel particulate matter: Diesel particulate matter and health. *Respirology*, 17(2):201–212, February 2012.
- [81] Matthias Möhner and Andrea Wendt. A critical review of the relationship between occupational exposure to diesel emissions and lung cancer risk. *Crit. Rev. Toxicol.*, 47(3):185–224, March 2017.
- [82] Marcelo Adriano Aliske, Giuliano Fernandes Zagonel, Bill Jorge Costa, Wanderley Veiga, and Cyro Ketzer Saul. Measurement of biodiesel concentration in a diesel oil mixture. *Fuel*, 86(10-11):1461–1464, July 2007.
- [83] Flüssige Mineralölerzeugnisse - Bestimmung des Gehaltes an Fettsäuremethylester (FAME) in Mitteldestillaten- Infrarotspektrometrisches verfahren; deutsche Fassung, September 2014. DIN EN 14078:2014.
- [84] A. Guerrero, F. Anguebes, M. Castelán, V. Morales, R. García, A. V. Córdova, and J. C. Zavala. FTIR-ATR and multivariate calibration for the prediction of biodiesel concentration in petrodiesel blends. *Am. J. Chem.*, 04(07):343–347, 2013.
- [85] Test Method for Determination of Biodiesel (Fatty Acid Methyl Esters) Content in Diesel Fuel Oil Using Mid Infrared Spectroscopy (FTIR-ATR-PLS Method), 2014. ASTM D7371-14.
- [86] Hui Zhao, Kun Zhao, and Rima Bao. Fuel property determination of biodiesel-diesel blends by terahertz spectrum. *J. Infrared, Milli., THz Waves*, 33(5):522–528, May 2012.
- [87] Hui Zhao, Kun , Lu Tian, Qing Miao, and Hao Ni. Optical property of biodiesel and its base stock in terahertz region. *Front. Optoelectron.*, 5(2):214–217, June 2012.
- [88] M. Méndez Aller, D. S. Ong, H. L. N. Lau, and S. Preu. Broadband determination of biodiesel content in petroleum diesel blends by terahertz time domain spectroscopy. *IEEE Transactions on Terahertz Science and Technology*, 2021. doi:10.1109/TTHZ.2021.3049646.
- [89] Automotive fuels - Palm Methyl Esters (PME) for diesel engines - requirements and test methods (first revision), 2014.

- [90] Diesel fuel - specification - part 3: Euro5, 2016.
- [91] Magán Lapuerta, José Rodríguez-Fernández, David Fernández-Rodríguez, and Rayda Patiño-Camino. Modeling viscosity of butanol and ethanol blends with diesel and biodiesel fuels. *Fuel*, 199:332–338, July 2017.
- [92] Graham J. Davies and Myron Evans. Use of generalized Langevin theory to describe far infrared absorptions in non-dipolar liquids. *J. Chem. Soc., Faraday Trans. 2*, 72:1194, 1976.
- [93] M. Davies and C. Brot. Correlation function in dipolar absorption-dispersion. In *Dielectric and related molecular processes*, volume 2, pages 1–47. Royal Society of Chemistry, Cambridge, 1975.
- [94] Graham J. Davies and Myron Evans. Use of generalized langevin theory to describe far infrared absorptions in non-dipolar liquids. *J. Chem. Soc., Faraday Trans. 2*, 72:1194–1205, 1976.
- [95] Junko Habasaki, Carlos León, and K. L. Ngai. *Dynamics of glassy, crystalline and liquid ionic conductors: experiments, theories, simulations*, volume 132 of *Topics in applied physics*. Springer, Switzerland, 2017.
- [96] J.E. Pedersen and S.R. Keiding. THz time-domain spectroscopy of nonpolar liquids. *IEEE J. Quantum Electron.*, 28(10):2518–2522, October 1992.
- [97] Khairul Zahan and Manabu Kano. Biodiesel Production from Palm Oil, Its By-Products, and Mill Effluent: A Review. *Energies*, 11(8):2132, August 2018.
- [98] J. Bae, C. Jeong, J. Lim, H. Lee, G. Yeom, and I. Adesida. Anisotropic etching of InP and InGaAs by using an inductively coupled plasma in Cl₂/N₂ and Cl₂/Ar mixtures at low bias power. *Journal of The Korean Physical Society*, 50, 04 2007.

Erklärungen laut Promotionsordnung

§ 8 Abs. lit. c PromO

Ich versichere hiermit, dass die elektronische Version meiner Dissertation mit der schriftlichen Version übereinstimmt.

§ 8 Abs. 1 lit. d PromO

Ich versichere hiermit, dass zu einem vorherigen Zeitpunkt noch keine Promotion versucht wurde. In diesem Fall sind nähere Angaben über Zeitpunkt, Hochschule, Dissertationsthema und Ergebnis dieses Versuchs mitzuteilen.

§ 9 Abs. 1 PromO

Ich versichere hiermit, dass die vorliegende Dissertation selbstständig und nur unter Verwendung der angegebenen Quellen verfasst wurde.

§ 9 Abs. 2 PromO

Die Arbeit hat bisher noch nicht zu Prüfungszwecken gedient.

A handwritten signature in blue ink, appearing to read 'M. Meinde', is shown on a light blue background.

12.3.2021

Datum und Unterschrift

Selected Publications

1. Méndez Aller, M.; Ong, D.S.; Lau, H. L. N.; Preu, S. (2021):
Broadband determination of biodiesel content in petroleum diesel blends by terahertz time domain spectroscopy.
In: IEEE Transactions on Terahertz Science and Technology.
DOI:10.1109/TTHZ.2021.3049646.
2. Méndez Aller, M.; Abdul-Munaim, A.; Watson, D.; Preu, S. (2018):
Error Sources and Distinctness of Materials Parameters Obtained by THzTime Domain Spectroscopy Using an Example of Oxidized Engine Oil.
In: Sensors, 18 (7)
DOI: 10.3390/s18072087
3. Abdul-Munaim, A.; Méndez Aller, M.; Preu, S.; Watson, D. (2017):
Discriminating gasoline fuel contamination in engine oil by terahertz time-domain spectroscopy.
In: Tribology International.
DOI:10.1016/j.triboint.2017.10.026
4. Méndez Aller, M.; Preu, S. (2019):
Quasi-Analytical Description of a Double Slit Planar Dielectric Waveguide as Broadband Dispersion Compensating Element.
In: 2019 44th International Conference on Infrared, Millimeter, and Terahertz Waves (IRMMW-THz), Paris, France.
DOI: 10.25534/tuprints-00011361
5. Méndez Aller, M.; Lu, H; Gossard, A.C.; Nandi, U.; Norman, J.C.; Preu, S. (2018):
ErAs Enhanced Active Photonic THz Components.
In: 2018 First International Workshop on Mobile Terahertz Systems (IWMTS), Velen, 2.-4.7.2018
DOI: 10.1109/IWMTS.2018.8454690
6. Méndez Aller, M.; Lu, H.; Gossard, Arthur C.; Preu, S. (2018):
Continuous-Wave Terahertz System with 50 dB Dynamic Range at 1 THz Using a ni-pn-ip Superlattice Photomixer and an ErAs: InGaAs Photoconductor Operated at 1550 nm.
In: 2018 43rd International Conference on Infrared, Millimeter, and Terahertz

Bibliography

Waves (IRMMW-THz)

DOI: 10.1109/IRMMW-THz.2018.8510172

7. Méndez Aller, M.; Fernandez Olvera, A.de J.; Lu, H.; Gossard, A. C.; Preu, S. (2016):

Pulsed THz time domain system with ErAs:In(Al)GaAs photoconductors.

In: 2016 41st International Conference on Infrared, Millimeter, and Terahertz waves (IRMMW-THz), Copenhagen.

This thesis contains material that has been previously published in scientific journals and conferences. Table D.1 summarizes the relationship between these publications and the content of this thesis. No text in this document is directly copied out of the publications. However, figures and tables have been replicated in this thesis. This is done in order to make correct use of the gathered data and previous results. A list of selected scientific publications of the author of this thesis is available at the end of the thesis. Scientific work usually is the result of a joint effort in a team. Hence, all publications described below are the result of the collaborative work.

Chapter 3	M. Méndez Aller et al., "Side-illuminated fully ballistic p-i-n diode-based photomixer at 1550 nm," 2020 45th International Conference on Infrared, Millimeter, and Terahertz Waves (IRMMW-THz), 2020, pp. 1-2.
Chapter 5	[74, 78]
Chapter 6	[88]

Table D.1.: Chapters related with publications from the author